Prediction of static failure in titanium based fibre metal laminates

G Corderley

22930728

Thesis submitted for the degree *Philosophiae Doctor* in Mechanical Engineering at the Potchefstroom Campus of the North-West University

Promoter: Dr JJ Kruger

October 2017

Abstract

Fibre Metal Laminates (FMLs) made of titanium and carbon-fibre reinforced epoxy have the potential to reduce the mass of structures that would otherwise be made of conventional materials. This material also exhibits good fatigue performance and resistance to localised and impact damage. These properties make the material a good candidate for airframes. The properties of the material also make it suitable for military vehicles that require light weight armour.

The design of components that include FMLs requires a model to predict the failure under static loads. The static failure modelling of titanium / carbon based FMLs has seen relatively little research. A failure model for FMLs will include different failure criteria for each of the composite and metallic constituents. The evaluation of the best constituent criteria for inclusion into a titanium / carbon FML failure model has also seen little research. A model is therefore presented which predicts the failure progression of a titanium / carbon FML. The predictions cover the range from the initial failure in the material up to the point of final collapse. The individual failure criteria for the material constituents are selected on the basis of their applicability to the modelling such an FML.

The accuracy of the proposed progressive failure model is investigated by two methods. The model is first verified by laboratory level tests and thereafter validation is carried out by means of field trials that are representative of actual service conditions.

The laboratory level verification includes the design of various types of test samples that will exhibit different failure modes. These samples are tested under load where both the initial and final failure modes are recorded. The initial failure modes are detected through the simultaneous examination of the data from the strain output, acoustic monitoring, micrographic examination and micro-focus X-Ray examination. The results from the tests are compared with the progressive failure modes predicted by the model, where there is good correlation.

The validation of the failure model under realistic field conditions is achieved through the development and testing of armour panels that meet the need for light weight protection against improvised explosive devices. The static progressive failure model is used as an input to the design the armour panels. Additional predictive ballistic models are required for the balance of the design calculations. These ballistic models do not exist for FMLs and

therefore they are developed for this work. The armour panels are then tested against a representative threat. Additional ballistic theory is also developed for the analysis of the test data in order to determine the performance of the armour. The correlation between the predictions and test results is good.

Keywords

Fibre Metal Laminate, FML, titanium, carbon-fibre, composite, static failure, progressive failure, terminal ballistics, armour.

Acknowledgements

The people listed below are acknowledged as having made a contribution to the work contained in this thesis. The nature of the contribution and the section which includes the contribution are also given.

Name	Contribution	Section
Dr UA Curle	Operation of micro-focus X-Ray equipment.	3.3.3
M Grobler	Assistance with the manufacture of armour panels (1).	4.7.3, 4.8
E Guldenpfennig	Assistance with the mechanical testing of samples (1).	3.3
M Johannes	Thermographic inspection of samples.	4.8.2
Dr JJ Krüger	Thesis Promotor.	All
Prof L Liebenberg	Academic guidance.	All
Prof EH Mathews	Academic guidance.	All
C McDuling	Assistance with the mechanical testing of samples (1).	3.3
Dr FJ Mostert	Mentorship in the fields of external and terminal ballistics. Management of a ballistic test range. Analysis of terminal ballistic data.	Chapter 4
Dr K Mutombo	Thermo-mechanical processing of titanium sheet. SEM examination of titanium samples.	4.7.4, 4.8.2
H Nolte	Proofreading of the thesis.	All
D Ntuli	Assistance with the manufacture of armour panels (1).	4.7.3, 4.8
P Rossouw	Procurement of titanium sheet. Manufacture of an anodisation facility and the subsequent treatment of the titanium sheets.	4.7.2
J Steyn	Laser ablation of titanium specimens.	4.7.2
Dr JD van Rensburg	Academic guidance.	All
JD Wilkins	Manufacture of mechanical test samples. Assistance with the manufacture of armour panels (1).	3.2.5, 4.7.3, 4.8
MB Williams	Design and manufacture of a dipping frame for titanium anodisation.	4.7.2

Note (1): Assistance was given as required by laboratory procedures that are derived from safety legislation and ISO 17025 requirements.

Table of Contents

List of Figures

List of Tables

Chapter 1. Introduction

In this chapter an introduction to Fibre Metal Laminates (FMLs) is presented, together with a review of the published research. Also discussed is the research hypothesis and how this work will contribute to the field. The ensuing structure of the thesis is given in outline form, and the unique aspects of the study are identified.

1.1 Introduction to Fibre Metal Laminates

The concept of an FML can be seen in Figure 1, where the material is made from alternating layers of continuous fibre reinforced composites and metal alloys. The most common types of this material are referred to as GLARE (Glass Laminate Aluminium Reinforced Epoxy) and TiGr (Titanium-Graphite), which are characterized by their material constituents:

- GLARE: Aluminium and glass fibre reinforced polymer
- TiGr: Titanium and graphite or carbon fibre reinforced polymer

This material is therefore a hybrid of the two dominant airframe materials, namely light metal alloys and continuous fibre reinforced composites.

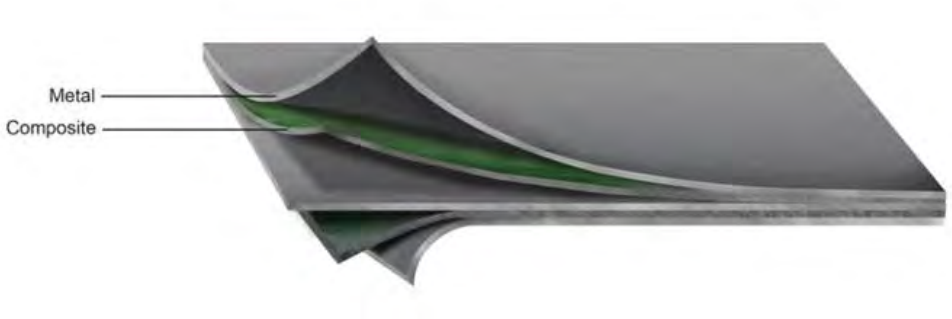

Figure 1: Typical Fibre Metal Laminate

The hybridisation of the different material types results in the advantages of each constituent material type being retained, while the disadvantages of the constituents are minimised. This will result in a material that has some advantages over traditional aerospace materials. In comparison to aluminium structures, FMLs exhibit higher specific strength and stiffness and also better fatigue and fracture properties. When compared to continuous fibre composite

structures FMLs have a higher bearing strength, better impact resistance and an improved resistance to environmental effects.

The various grades of GLARE all use the same composite materials. The composite core is made from S-glass fibres in conjunction with the FM 94 adhesive [1]. The resulting composite has a lamina thickness of 0.127 mm with a fibre volume fraction of 59%. These fibres are 10μm thick, with a strength of 4 000 MPa, a stiffness of 88 GPa and a strain to failure of 4.45%. The adhesive has a strength of 50 MPa, a stiffness of 1.7 GPa and a strain to failure of 5 to 10%, depending on the strain rate.

There are six standard grades of GLARE [1], as summarised in Table 1. The different types can be classified according the orientation of the uni-directional composite layers and the type of aluminium alloy used. GLARE grades 1, 2, 4 and 5 have a symmetrical stacking of the composite laminae. GLARE 3 uses a cross-ply configuration, with the lamina closest to the outside of the airframe having a direction corresponding to the rolling direction of the aluminium. An analogous situation exists for GLARE 6, where the 6A grade has the first lamina at an angle of 45 degrees to the rolling direction. Grade 6B has this lamina at an angle of -45 degrees.

Table 1: Standard GLARE grades (adapted from [1])

GLARE Grade	sub	Metal Sheet Thickness (mm) & Alloy	Pre-Preg Orientation in each Fibre Layer	Main Beneficial Characteristics
GLARE 1	-	0.3-0.4 7475-T761	0/0	Fatigue, strength, yield stress
GLARE 2	GLARE 2A	0.2-0.5 2024-T3	0/0	Fatigue, strength
	GLARE 2B	0.2-0.5 2024-T3	90/90	Fatigue, strength
GLARE 3		0.2-0.5 2024-T3	0/90	Fatigue, impact
GLARE 4	GLARE 4A	0.2-0.5 2024-T3	0/90/0	Fatigue, strength in the 0º direction
	GLARE 4B	0.2-0.5 2024-T3	90/0/90	Fatigue, strength in the 90º direction
GLARE 5		0.2-0.5 2024-T3	0/90/90/0	Impact
GLARE 6	GLARE 6A	0.2-0.5 2024-T3	+45/-45	Shear, off-axis properties
	GLARE 6 B	0.2-0.5 2024-T3	-45/+45	Shear, off-axis properties

Another class of FMLs is generally known as TiGr, which combines titanium with graphite or carbon fibre reinforced composites. TiGr was initially studied as part of the NASA funded High Speed Research Program that focused on civil transport category aircraft [2]. A schematic view of the material is shown in Figure 2, where it can be seen to be conceptually similar to GLARE, while using different material constituents. The polymer used for the core is typically thermoplastic, where the processing times for the material manufacture is less

than for epoxy based systems. Thermoplastics can also offer better interlaminar fracture toughness and better resistance to environmental attack than epoxy resins [3].

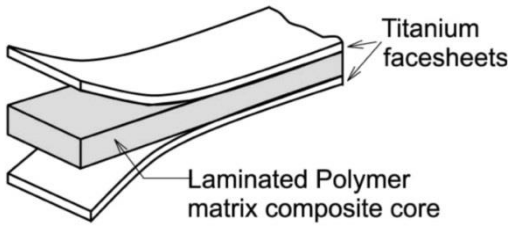

Figure 2: Schematic view of a TiGr laminate [4]

Typical TiGr laminates use a metastable beta titanium alloy 15V-3Cr-3Al-3Sn (Ti 15-3) metal foils of 0.127 mm thickness [5]. The polymer matrix laminae are 0.142 mm thick with IM-7 fibres and a PIXA-M thermoplastic matrix where the fibre volume fraction is approximately 0.6 [4]. The stacking sequences for the various grades of TiGr [6] are given in Table 2.

Table 2: TiGr designation (adapted from [6])

Designation	Stacking Sequence
TiGr 2-6-2	$[Ti/0/90/0_2]_S$
TiGr 2-2-6	$[Ti/90/0/90_2]_S$
TiGr	$[Ti/0/90/\pm30_2]_S$

The elastic properties for the TiGr laminate are determined from the constituent properties by means of classical laminated plate theory. The laminate properties are listed in Table 3.

Table 3: TiGr elastic properties (adapted from [6])

Material Property	Ti 15-3	IM-7/PIXA-M	TiGr 2-6-2	TiGr 2-2-6	TiGr
E_1 (GPa)	107	155	118	58.5	86.9
E_2 (GPa)	112	6.9	58.5	118	59.6
G_{12} (GPa)	41.4	5.1	11.7	11.7	22.3
v_{12}	0.33	0.35	0.16	0.081	0.32

Manufacturing studies were carried out by NASA which established induction bonding [7] and automatic tape placement [8] methods for the TiGr material.

1.2 Properties of Fibre Metal Laminates

Vogelesang and Vlot [9] investigated the frequency of repairs to the Boeing 747 fuselage primary structure. Their study included seventy one aircraft with an average of 29 500 flying hours. The findings concerning the primary damage types requiring repair were as follows:

- Fatigue: 396 repairs (57.6% of total)
- Corrosion: 202 repairs (29.4% of total)
- Impact: 90 repairs (13.0% of total)

The resistance of a material to these three damage types is therefore of interest, as is the resistance to burn-through due to regulatory requirements.

1.2.1 Fatigue Behaviour

The damage tolerance of airframes was traditionally dealt with as a structural design problem. The failure of part of the structure on a Boeing 737 operated by Aloha Airlines [10] showed that a more rigorous approach was required. In the case of this particular failure a number of small cracks emanating from the rivet holes in a single lap joint grew together to form a single long crack after 90 000 flight hours. This single crack resulted in the loss of part of the upper fuselage section. It became evident that safe operation should also include consideration of the material selection, maintenance and a deeper understanding of the complex and interacting failure modes in an aircraft structure. Since the introduction of the jet transport aircraft, the increase in the fuselage pressures and diameters has resulted in the loading on the fuselage skins more than doubling. Current generation aircraft also face higher loads than the Boeing 737 did [10]. This increase in loads has made the fatigue of fuselage skins an increasingly critical matter.

A comparison was done of the fatigue of pre-cracked aluminium 2024-T3, GLARE 2, GLARE 3 and ARALL 2 [9]. As can be seen in Figure 3, there is a strong increase in the crack growth rate for the aluminium 2024 as the crack length increases, while the laminated materials show slow crack growth. The laminates have crack growth rates that are between ten and a hundred times slower than those for monolithic aluminium.

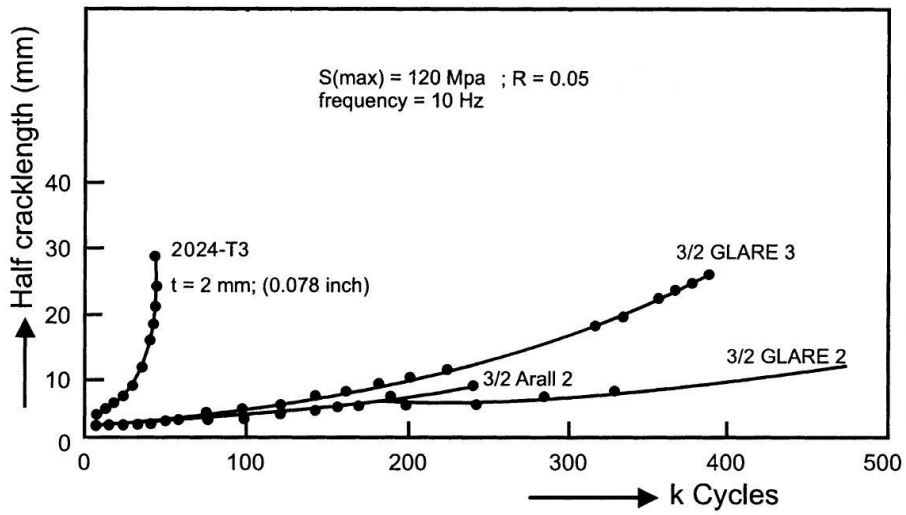

Figure 3: Fatigue of Al 2024-T3 and GLARE (adapted from [9], [10])

Figure 4 shows the residual strength of riveted lap joints in aluminium and GLARE resulting from fatigue loading. In comparison to aluminium the GLARE based joints show a slower reduction in strength. The aluminium joint notably shows a rapid reduction in strength once fatigue cracks form, mandating frequent inspection intervals on an airframe [10].

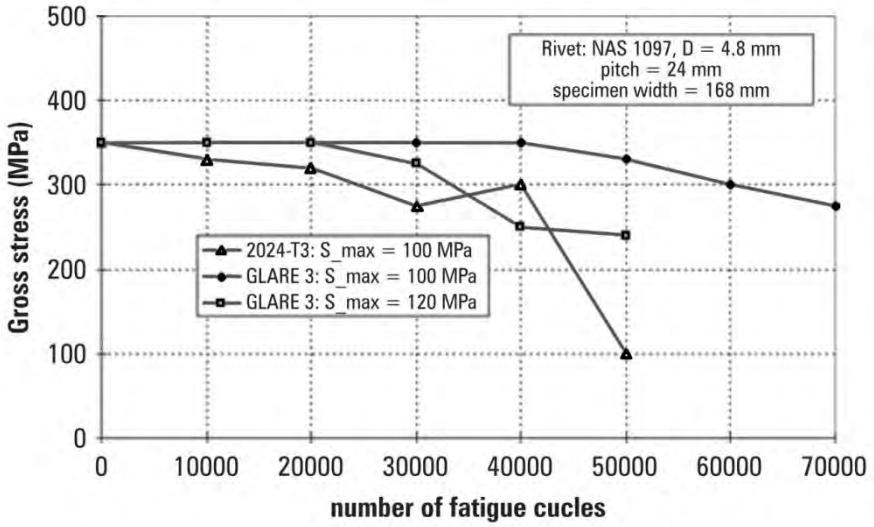

Figure 4: Residual strength of riveted lap joints after fatigue (adapted from [9], [10])

The results of material tests from the literature provide insight into the behaviour of the TiGr class of material. The published test data includes the following aspects of fatigue:

- Face sheet cracking and associated delamination
- Edge delamination of face sheet
- Open hole damage growth

Burianek and Spearing investigated the cracking and delamination of the face sheets of TiGr under fatigue loading. Their work incorporated both experimental investigations [5] and analytical predictions [6]. They used the 3D Virtual Crack Closure Technique (VCCT) and tunnelling models in their analysis. Both methods gave good predictions of the test results, with the VCCT proving to be the most robust. Another notable aspect of this work is the effect of temperature on the crack growth rate as a result of the thermal stresses altering the effective R-ratio in the material.

Alderliesten [11] concluded that the driving mechanism of fatigue behavior in TiGr FMLs is the initiation and growth of cracks within the metal face sheets. The cracks in the metal laminae in turn cause the growth in the delamination of the adhesive that forms the interface to the fibre layers. The relationship between the delamination growth rate and the strain energy release rate may be described by a Paris type equation [12]. The conclusion is that the adhesive type is the main factor contributing to the delamination resistance [11].

Burianek, Giannakopoulos and Spearing [6] developed numerical models to predict the propagation of both the facesheet crack and the underlying delamination in TiGr laminates. They developed a 2D bridged-crack (BC) model and a three dimensional VCCT model. The damage modes considered in the models are shown in Figure 5 and consist of cracks and delamination. The cracks extend the full thickness of the titanium face sheets. Both face sheets are affected, with the geometry of the damage being symmetric around the centre plane of the laminate. The delamination occurs between the titanium face sheets and the composite core. This follows the same symmetry as the damage to the face sheets.

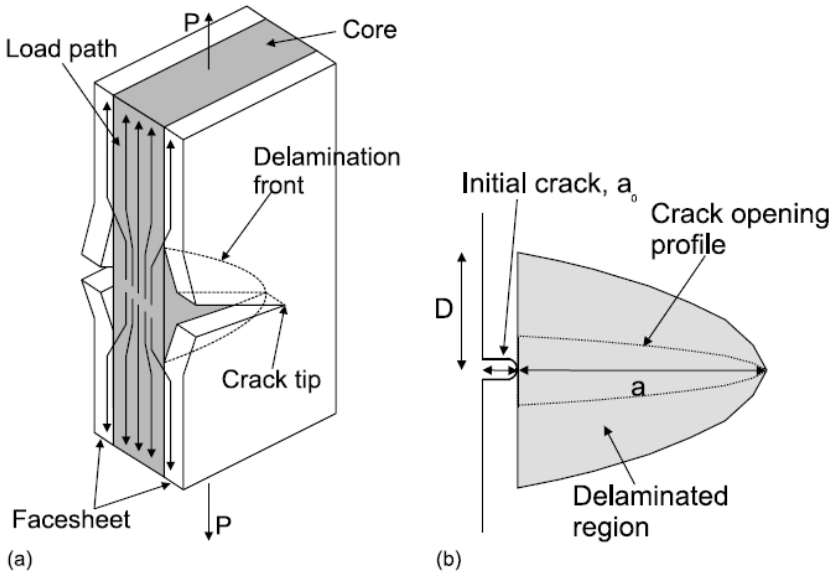

Figure 5: Bridged crack damage modes (a) 3D view (b) plan view [6]

When the two damage modes are allowed to grow the titanium face sheet crack extends, while the underlying composite plies remain intact. These composite plies carry some of the applied load, reducing the load on the crack tip in the titanium. Both the BC and 3D VCCT methods show good correlation with the test data [6].

The face sheet edge delamination is of relevance when large FML panels are manufactured by using butted seams to join the sections of face sheet. Burianek and Spearing [13] carried out a study into the delamination arising from these seams in TiGr at a range of temperatures. Their conclusion was that the propensity for delamination at the interface is driven by the intensity of the strain energy release rate, which is in part dependent on the lamination angles of the composite core.

Fibre metal laminates will typically be applied in conjunction with mechanical fasteners. The stress concentrations around the fastener holes make them vulnerable to damage growth. Burianek and Spearing [4] carried out tests to determine the high temperature fatigue performance on TiGr laminates containing open holes.

The TiGr laminate exhibited several different damage modes which interacted to cause the final failure [4]. These modes included cracking in the titanium face sheets, matrix cracks in outer 0^O plies parallel to the load direction and transverse cracks in the 90^0 plies perpendicular to the load direction.

1.2.2 Impact Resistance

Composite materials have relatively poor impact resistance, which increases the cost of inspection and repair. Fibre metal laminates on the other hand are inherently more resistant to impact damage and any resulting damage can be repaired with riveted metal patches in the same way as conventional structures [10].

The minimum energies at impact required to cause initial failure in various materials are summarised in Figure 6 for both standard drop weight and gas gun tests [10]. GLARE shows a greater resistance to impact damage than aluminium 2024-T3 across the range of impact dynamics. The higher impact resistance of GLARE is attributed to strengthening of the glass fibres which occurs at high strain rates, which is in addition to their relatively high static strain to failure.

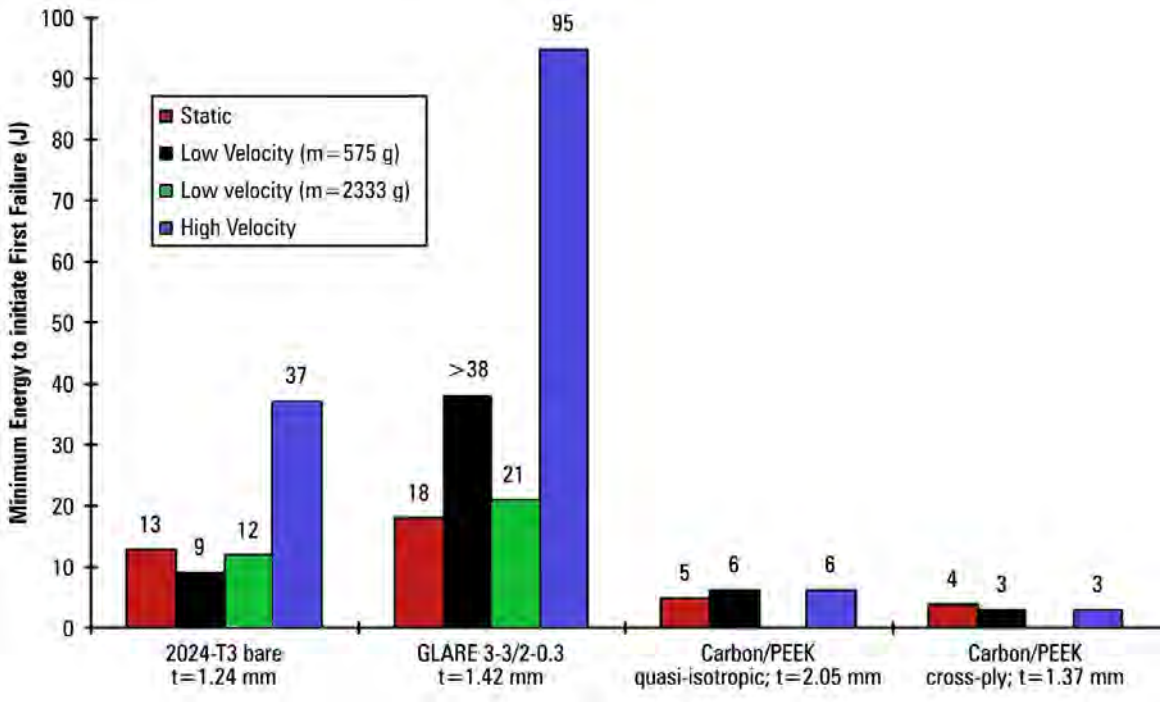

Figure 6: Impact resistance of aluminium and fibre metal laminates (adapted from [10])

The low velocity puncture energy for GLARE 3 and 4 and aluminium 2024-T3 is shown in Figure 7 [9], where both grades of GLARE show superior performance to the aluminium at all comparable panel thicknesses.

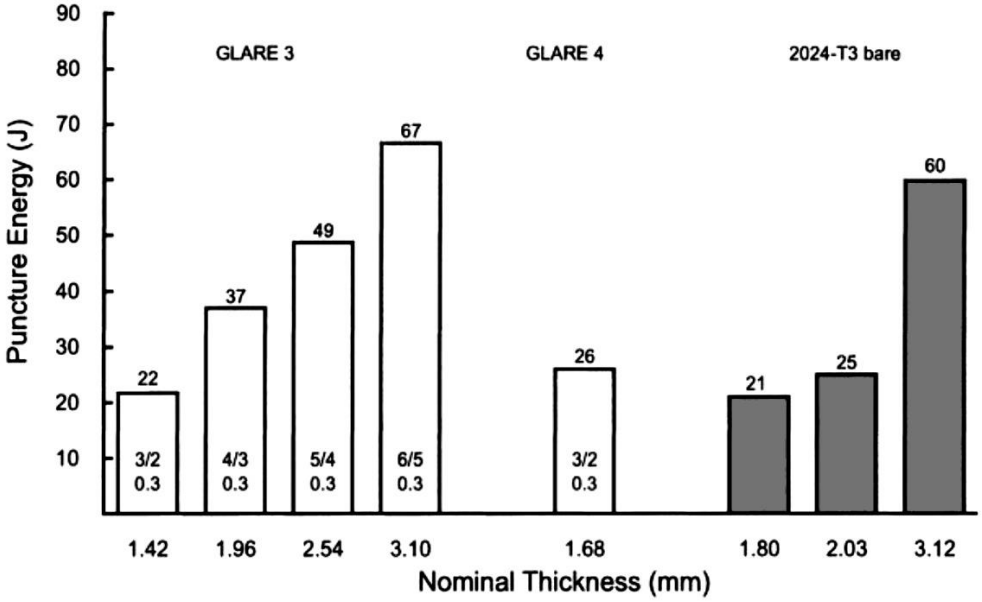

Figure 7: Low velocity puncture energy for GLARE and Al 2024-T3 [9]

Up to the point of the initial failure of the fibres and the face sheets on impact, there is only minor matrix damage in the GLARE. The damage area to the composite is less than the area of the visible dent, with failure in the outer aluminium layer occurring before the fibre failure. The first crack in an impacted panel may occur within the interior of the panel due to the bending on the laminate. The crack growth under fatigue loading, however, will only occur on the outside surface which was impacted, making the damage easier to inspect [10].

1.2.3 Corrosion

In the case of FMLs that include aluminium sheets, these sheets are first anodised and then treated with a corrosion inhibiting primer [10]. The resistance of the aluminium can be further enhanced by using a thin clad layer instead. The fibre – epoxy layers provide a barrier to through-the-thickness corrosion.

An example of the exploitation of the corrosion properties of FMLs is the repair of an Indonesian F28 aircraft [10]. The original stiffeners were heavily corroded within a year of service, and were replaced with FML equivalents as shown in Figure 8.

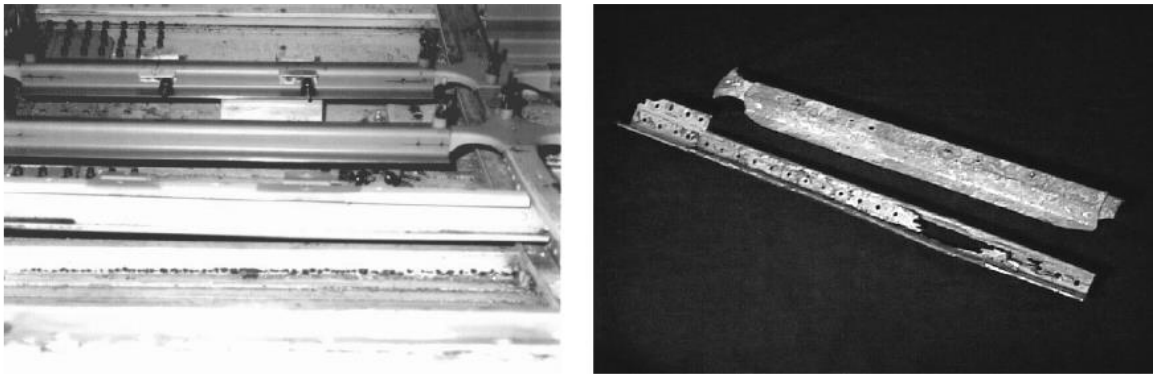

(a) (b)

Figure 8: F28 Corrosion repair: (a) GLARE stiffeners installed, (b) original corroded aluminium stiffeners [10]

1.2.4 Flame Resistance

An advantage of FMLs in relation to metals is the increased resistance to burn-through. Tests representative of a typical kerosene fire impinging on an aircraft structure have been carried out where a total heat flux of 204 W/m^2 was applied to material samples at a temperature of 1 150ºC [10]. The two materials tested are GLARE 4-3/2-0.5, a biaxial FML intended as a fuselage material with a 2.1mm thickness, and also the aluminium 2024-T3 alloy with a 2mm thickness. A summary of the results can be seen in Figure 9. The exposed aluminium face sheet of the GLARE melted quickly. The glass fibres subsequently remained intact while the resin burned, forming a carbon layer. This material state acted as an effective fire barrier against further burn-through, with delamination providing further insulation. No flame penetration of the GLARE occurred by the end of ten minutes of testing, while the 2024-T3 samples showed burn-through within 100 seconds.

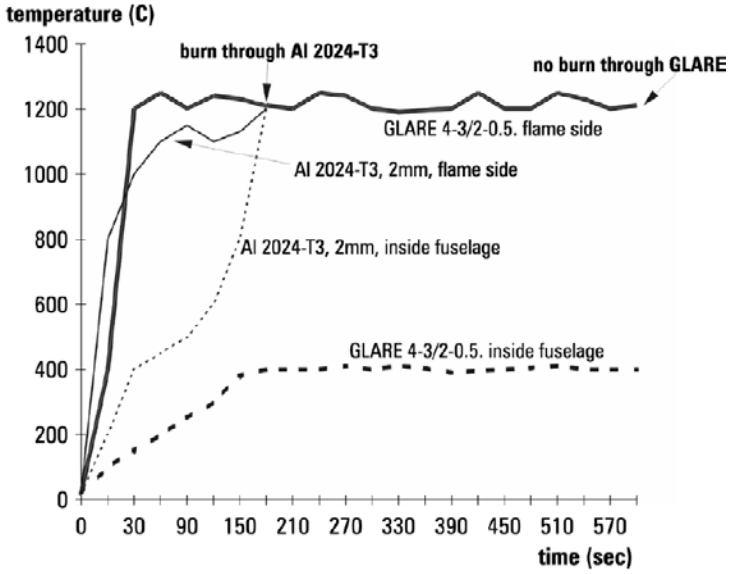

Figure 9: Flame penetration of GLARE and Al 2024-T3 [10]

1.3 Application of Fibre Metal Laminates to Airframes

The application of composite materials to airframes has been growing with time, with aircraft entering service having 50% of the airframe attributable to composite materials. The reason for the adoption of composites is that the airframe cost and weight is lower when using composite materials as opposed to metals [14].

An aircraft of particular interest is the airbus A380. The overall composite material usage is shown in Figure 10, with the specific application areas of the fibre metal laminates highlighted in Figure 11.

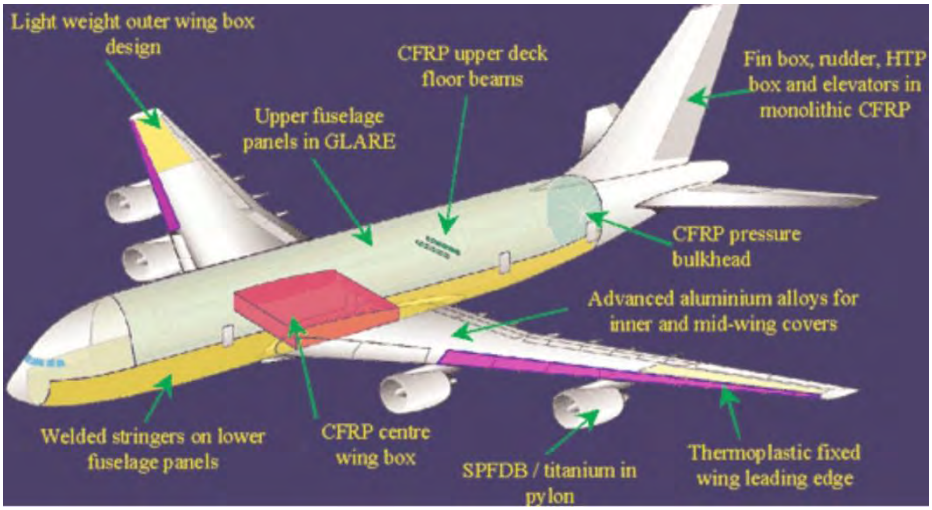

Figure 10: Airbus A380 material usage [15]

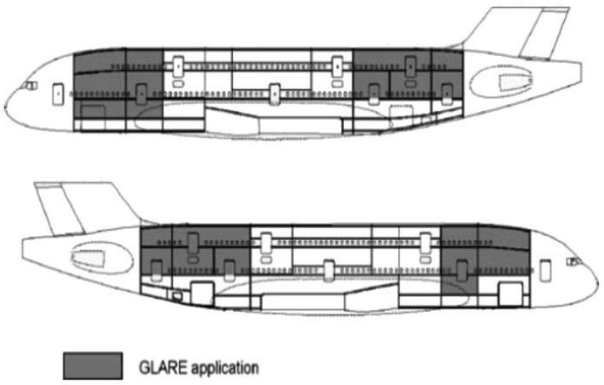

Figure 11: Application of GLARE to the A380 fuselage (adapted from [16])

The dimensions to which a GLARE panel can be manufactured are constrained by the available width of the aluminium sheets. These sheets typically have a maximum width of 1.65 metres, while fuselage skins may require widths of over 2 metres. This limitation prompted the development of concepts to manufacture large panels with the metal sheets spliced to the required dimension [1]. In the case where the splices are in the direction of loading they can act as crack stoppers, improving the integrity of the structure [17].

A splicing technique was devised that only requires a single autoclave cycle, where the autoclave pressure is used to form the aluminium and still flexible composite core into a configuration that inherently contains doublers at the joints [1]. This is termed the Self Forming Technique (SFT), where typical cross-sectional layouts can be seen in Figure 12. The metal on metal contact and extra internal spaces within the laminate means that extra adhesive needs to be added for the forming of the panels. This adhesive is of the same type used for the composite core. This technique also allows for local tailoring through the addition of layers within a specific area [1].

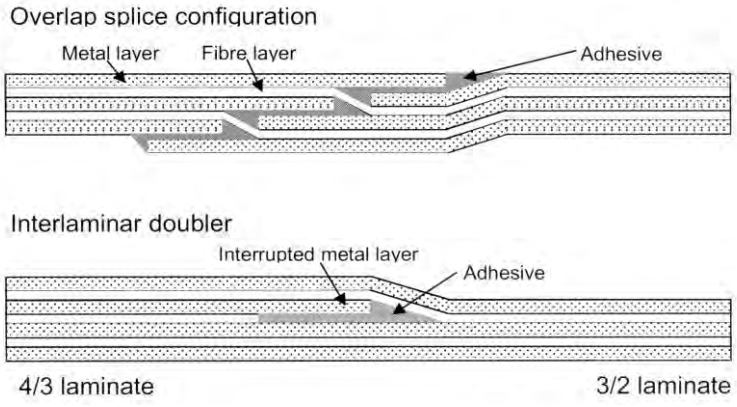

Figure 12: Typical self-forming layouts [1]

The in-service repair of airframes is also a matter of relevance. A damage tolerant repair of aluminium skins may be made with GLARE 3 and 4, which have biaxial fibre directions [9]. The fatigue resistance and the high blunt notch strength of these GLARE laminates make them suited for application as riveted patches, as shown in Figure 13.

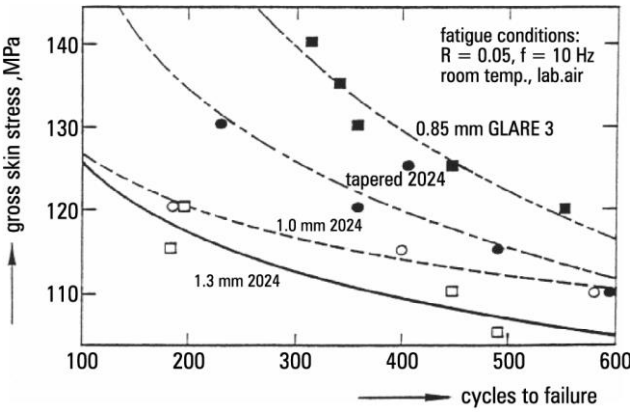

Figure 13: Fatigue life of aluminium skins repaired with riveted patches [9], [10]

The uni-directionally reinforced GLARE 1 and 2 materials may be applied as an adhesively bonded patch repair to intact cracks. This type of damage is typical for ageing transport category aircraft which may suffer from multiple site fatigue damage. GLARE has proven to be superior to boron / epoxy patches at high altitudes due to the lower thermal expansion mismatch between the patch and skin [10].

1.4 Summary of Published Research

This study examined a variety of journal articles and dissertations which dealt primarily with fibre metal laminates made from titanium face sheets with carbon fibre reinforced polymer cores. The primary topics covered in these papers are summarised in Table 4. The table includes the primary loading factors, the material constituents that are considered in the failure analysis, whether the methodology is based around analysis or testing, if the paper is a review and finally if it is primarily supporting an investigation into manufacturing.

It can be seen that most of the research that has been reviewed has focused on the fatigue aspects of the material, with relatively little work around static failure, impact effects and the effect of holes. The material constituent that has been most thoroughly investigated is the face sheets, with the delamination in the adhesive receiving almost the same amount of

attention. Laminate failure has received relatively little attention. When it comes to methodology there has been more testing carried out than analytical simulations.

Table 4: Summary of publications

Reference	Loading				Failure			Methodology		Review Paper	Manufacturing
	Static	Fatigue	Impact	Hole	Laminate	Face Sheets	Adhesive Delamination	Analysis	Testing		
[18]		x				x	x	x	x		
[19]		x				x	x	x	x		
[20]		x				x	x	x		x	
[2]										x	
[13]		x					x		x		
[4]		x		x	x	x	x		x		
[5]		x				x	x		x		
[6]		x				x	x	x			
[21]		x				x	x	x			
[16]										x	
[22]		x				x	x		x		
[3]	x				x	x	x	x	x		
[23]			x		x	x	x		x		
[24]	x			x	x	x			x		
[15]										x	
[7]											x
[25]		x		x		x			x		
[26]		x				x	x	x		x	
[27]	x		x		x	x			x		
[28]											x
[29]											x
[30]								x	x		x
[31]	x				x	x			x		x
[32]	x	x				x	x		x		x
[33]		x				x	x		x		x
[9]										x	
[34]		x				x	x	x			
[11]		x					x	x		x	
[35]	x			x	x	x		x	x		
[36]	x						x		x		
[37]	x			x	x	x		x	x		
[38]									x		x
[39]									x		x
[40]									x		x
[41]	x	x	x	x	x				x		
[42]		x				x	x	x	x		
[43]			x		x	x			x		
[44]	x				x	x	x		x		
[45]		x		x		x	x	x	x		
[46]	x			x	x	x	x	x	x		
[47]									x		x
[48]			x				x		x		

The relevant articles from Table 4 will be discussed in more detail during the course of this thesis.

1.5 Need for the Work Presented in this Thesis

The advantages of the titanium / carbon FMLs make them an attractive alternative for the aerospace structural components where neither metals nor composites are well suited to the requirements. In order to realise this potential, design methods are needed for the material. The modelling of the progressive failure of titanium / carbon FMLs under static load is not an area that has seen a significant amount of research. There is even less research available where properly verified failure models for the constituent materials are included. This type of modelling is however required in order to arrive at a viable design.

In addition to the aerospace field, there is a need for the development of lighter weight armour for military vehicles. There is a lack of predictive methods that will allow for the design of titanium / carbon FMLs for resistance to specific threats. With such design methods in place it will be possible to develop armour that will resist the required threat levels at a low weight.

1.6 Thesis Hypothesis

It is proposed that a static load failure model can be developed for titanium / carbon FMLs that meets the usability requirements of the design process and that embodies a good degree of confidence in the predictions.

The FML is consists of multiple constituent materials. There is already a significant body of work regarding the failure models for these individual constituent materials. This allows for the selection of constituent models that are applicable to FMLs and which have been demonstrated to have good predictive capabilities. An additional requirement for the selection is that the constituent failure models should be able to predict all failure modes up to the point of final failure. The prediction of all modes is of particular importance in the aerospace industry, where the regulations typically define two different loads that the airframe must withstand. The structure must be able to withstand the lower load with no damage. The higher load must be taken without structural collapse, although some structural degradation may be incurred.

These constituent failure models may be combined into an overall failure model that predicts the progressive degradation of the FML under the application of load. This model may then be compared directly to laboratory level tests of titanium / carbon FMLs to determine the accuracy of the predictions.

The failure model may then be extended further to include relationships for the resistance to penetration by ballistic impact. These predictions may be compared to ballistic field tests to determine the accuracy of the model.

1.7 Overview of the Work in this Thesis

This section gives a broad overview of the general scope of the study. This is followed by a more detailed overview of each individual step pertaining to this study.

A broad overview of the scope is presented in Figure 14. The investigation was initiated by a literature survey. This survey then led into the development of software for the prediction of the static failure modes for FMLs. The software was then validated by two means. The first was laboratory tests of samples. The second was ballistic field tests and correlation of the results to the predicted failure modes.

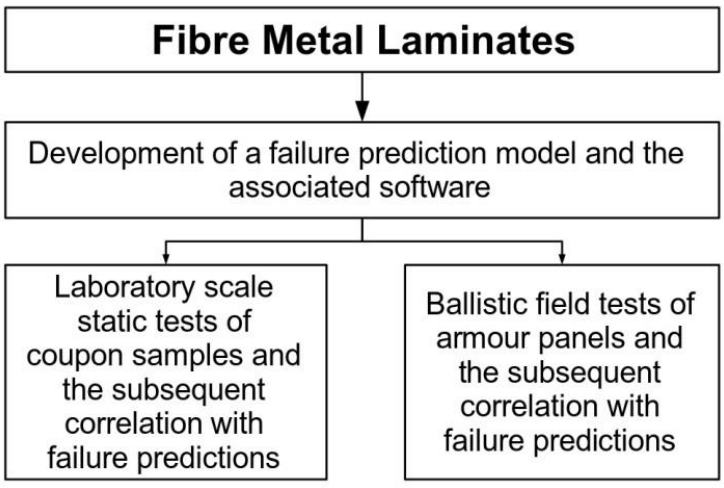

Figure 14: General scope of this investigation

The specific tasks that were carried out are given in Figure 15.

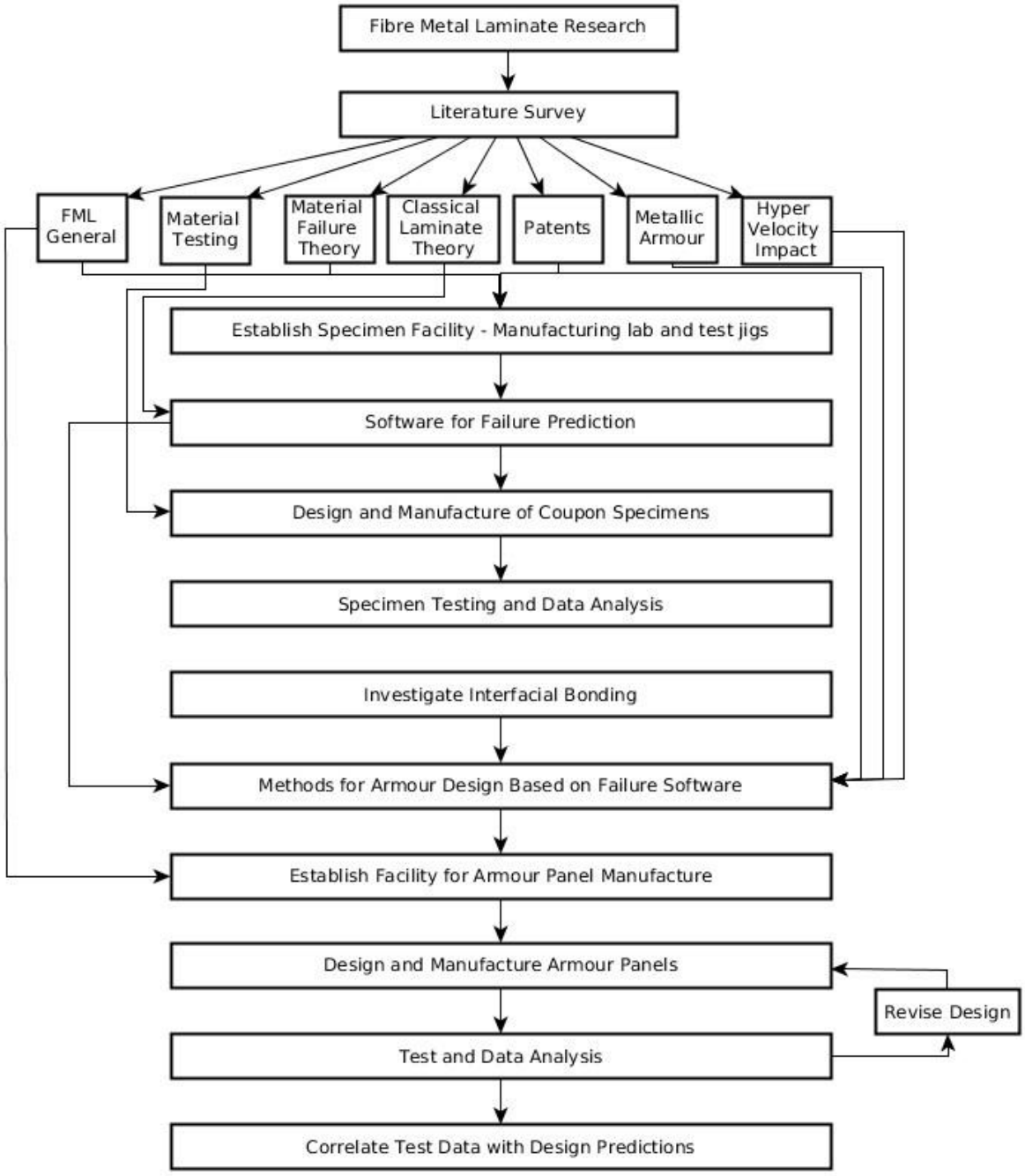

Figure 15: Steps followed in this investigation

1.8 Unique Aspects of the Work in this Thesis

The novelty of the research can be ascribed to the successive refinement of the topic, starting at the overall level of FMLs as a general topic and proceeding to the specific content of the research. The refinement of the technical scope includes the consideration of the overall material type, the loading type, nature of the material failures, the modelling of the failures, the static testing and finally the ballistic testing.

Overall Material Type: The majority of the research reported on in the literature pertains to the aluminium / glass fibre based FMLs. The titanium / carbon fibre based FMLs, as covered in this thesis, have received a lower volume of publication. All of the following comments pertain specifically to the titanium / carbon fibre type.

Loading Type: The majority of the reported research on the FMLs has focused on the fatigue behaviour. The static failure modes have received less attention, despite being of equal importance in the design process. The research presented is specific to the static failure behaviour.

Nature of the Material Failures: The majority of the existing research has addressed the failure of the metal face sheets. These studies also address the adhesive delamination between the face sheets and the composite core. Less effort has been spent on the investigation of the composite laminate failure. This thesis addresses the overall failure of the material, including the composite laminate.

Modelling of the Laminate Failure: The two most applicable models for predicting the failure of the composite laminates that are incorporated in the FMLs are identified for purpose of this thesis. None of the literature investigated these failure models with respect to FMLs. A method was developed for the purpose of the thesis to predict all of the progressive damage modes in the FML leading up to the final failure. Only one paper reported an attempt to model the progressive degradation, although this was done using a simple assumptive model.

Static Testing: Three different methods for monitoring the samples were combined into a single procedure for determining the failure modes, allowing for the differentiation between matrix and fibre failure. The different methods allow for the failure measurements to be correlated against each other, thereby increasing the confidence in the results. This particular combination of methods is not reported on in other research related to FMLs. The first method was the use of a stethoscope to monitor the specimens while load was being applied. This was done to identify the progressive degradation modes that occur before final failure, including that of the matrix. The specimens were also monitored during loading by means of micrographs taken of the edges to identify the onset of degradation. A micro-focus X-Ray facility was used to correlate the damage observed on the edges during the micrographic survey to the internal failure modes.

Ballistic Testing: The ballistic testing results are presented as additional verification of the progressive failure modelling. No reported means existed to determine the resistance of an FML panel to high velocity impact that was based on the failure characteristics of the panel. The lack of adequate theory resulted in an existing method for analysing the impact resistance of spacecraft being re-formulated to apply to single panels, as opposed to multi-wall structures. Additional relationships were implemented that allowed for the static failure characteristics of the FMLs to be translated as inputs to these relationships. A method was also developed to allow for the analysis of the test data to determine the ballistic limit of the armour.

Summary

The unique aspects of the research pertaining to the static failure modes of titanium / carbon fibre based FMLs are:

- The application of the Cuntze and Puck modified failure models to this type of material.
- The application of a method to predict of the progressive degradation of the panels under load.
- The acoustic monitoring of the test specimens under the application of load to determine the progressive damage modes and also the correlation with X-Ray results.
- A method to determine the ballistic resistance of the panels based on the predicted failure modes of the panels.
- A method to analyse terminal ballistic test data to determine the mass of armour at the ballistic limit.

1.9 Structure of the Thesis

The main body of the thesis is structured around three chapters, namely Chapters 2 through 4. The contents of these chapters reflect the general scope of the work presented in Figure 14, with a more detailed discussion being given below.

Chapter 2 - Numerical Modelling of the Static Failure of Fibre Metal Laminates: The proposed failure model for FMLs consists of three main aspects, namely the modelling of the elastic properties of the FML, the individual failure models for the material constituents and

then the inclusion of these models into a global failure model for the FML. The elastic properties of the FML can be determined by the application of classical laminate theory. The selection of failure models for the composite and metallic material constituents is done by considering published work where the existing failure models are compared to test results. An FML failure model is then proposed which gives a progressive analysis of the failure modes in the laminate as the loading on it increases. These failure predictions differentiate between the matrix and fibre failure in the composite constituents and also include the metallic constituent.

Chapter 3 - Mechanical Tests and Results: Mechanical tests are carried out to provide a laboratory level verification of the proposed FML failure model. The test planning includes a literature survey to determine the most applicable test standards for the study and also an investigation into the specimen geometry that will best avoid localised stress effects. With the specimen geometry fixed, three different composite lamination angles for the specimens are selected that will induce different failure modes. With the specimen geometry and lamination sequence determined the progressive failure prediction of these specimens is then carried out. During the course of the mechanical tests the loads for both the initial and final failure modes are noted. These loads are determined by a combination of strain output, acoustic monitoring, micrographic examination and in some cases micro-focus X-Ray examination. The resulting data is then compared with the failure predictions.

Chapter 4 - Ballistic Panel Theory and Design: The need for light-weight armour for the protection of military vehicles has prompted the study of FMLs in this application. The work as presented was carried out in order to establish the initial research baseline for future armour development. Two models are developed to predict the ballistic performance of FMLs. The background information for these models is drawn from the publications of various space agencies regarding the effect of high velocity impact on spacecraft structures by orbiting debris. The proposed models incorporate the FML static failure model, thereby allowing for further validation of this model under realistic field conditions. FML panels of various masses are then tested against high velocity penetrators at a ballistic range. The residual velocity of the penetrators exiting the panels is measured by means of a flash X-Ray system, proving data which allows for the calculation of the ballistic performance of the panel and correlation with the failure models.

Chapter 2. Numerical Modelling of the Static Failure Modes

2.1 Introduction to the Numerical Modelling

The development of a model for the prediction of the static failure progression of titanium / carbon-fibre based Fibre Metal Laminates (FMLs) is presented in this chapter. The type of FML in question consists of two main material constituents, namely, titanium and carbon-fibre reinforced epoxy. The use of these two material constituents necessitates the identification of suitable separate failure criteria from current practice. The requirements for these criteria will be their applicability to the specific material constituents and their suitability for inclusion into the overall FML failure model. The FML failure model is then presented, which allows for the prediction of the progressive damage occurring in the material as the loading increases up to the point of final failure.

2.2 Overview of Published Work

This section covers the modelling of titanium / carbon FMLs for the determination of failure under static loads. The literature related to this topic is limited, as noted in section 1.4.

Cortes and Cantwell [3] investigated the progressive failure of Titanium-Graphite (TiGr) laminates for a variety of fibre orientations. The FML used for that study consisted of a titanium 15-3-3-3 alloy and APC-2, a unidirectional AS4 carbon and PEEK based thermoplastic from Fiberite. A PEEK interlayer was also used to ensure bonding between the composite and the metal.

The angle θ is taken as being the angle between the uni-directional lamina fibres and the longitudinal axis of the test specimen. The stacking sequence for the FML in terms of this angle is $[Ti, -\theta, +\theta]_s$, where the subscript s denotes a plane of symmetry [3]. The FML lamination is shown in Figure 16. The interlayers are not shown, but constitute the interface between the metal and carbon layers. The lamination angle θ is varied in fifteen degree steps from 0° to 90°.

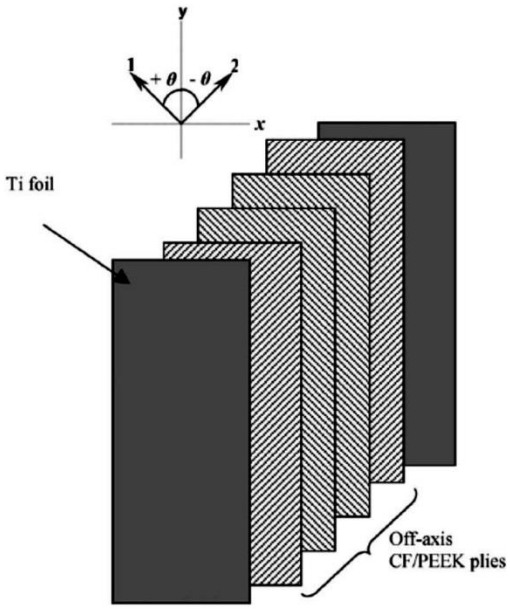

Figure 16: Ti 15-3 / APC-2 FML stacking sequence [3]

The authors used two separate degradation models for the composite laminae, depending on the angle θ. For the 0° to 15° lamination angles it was assumed that individual lamina failure would be in the fibre direction and the longitudinal Young's modulus E_1, the shear modulus G_{12} and Poisson's ratio ν_{12} terms were removed from the calculation upon the onset of failure. For higher fibre angles it was assumed that the lamina failure would be in the resin and the transverse E_2 term was removed instead upon the onset of failure, together with the G_{12} and ν_{12} terms. Plastic failure was assumed for the titanium and interlayers, except in the case where these were the last plies to fail.

The results of the tensile tests on the material are given in Figure 17 for the stress-strain response and in Figure 18 for the variation in stiffness with lamina angle.

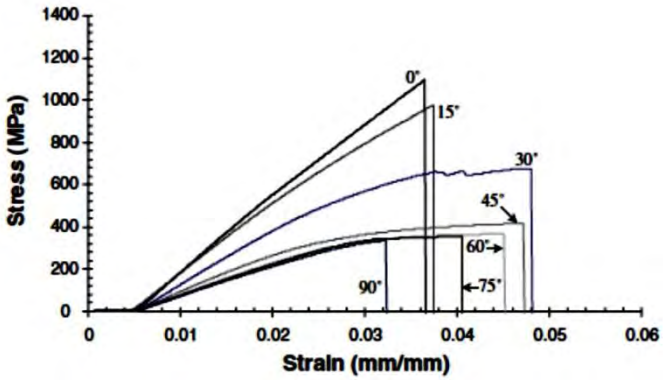

Figure 17: Ti 15-3 / APC-2 FML tensile test results for various values of θ [3]

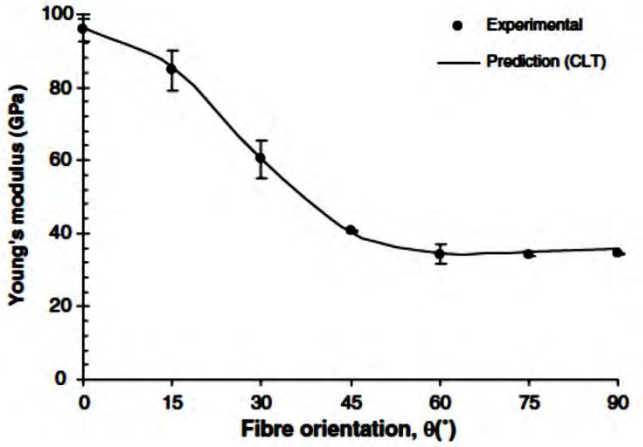

Figure 18: Ti 15-3 / APC-2 FML stiffness variation with θ [3]

A microscopic examination was carried out to determine the failure modes of the laminates [3]. The failure initiated in the composite material for all lamination angles. The failure initiation for the 0° laminate was in the fibre, with no propagation being observed along the fibre-matrix interface. The 15° laminate showed failure initiation in the fibres once again, but with the subsequent propagation being along the fibre / matrix interface. All laminates with a fibre angle or 30° or larger showed the failure initiation and the subsequent propagation as being localized to the matrix.

FMLs are often processed at higher temperatures during manufacture than occur during operation, resulting in residual thermal stresses in the laminate. This matter is of interest for the manufacturing process development of test specimens. The thermal forces $\{N^{TH}\}$ and moment resultants $\{M^{TH}\}$ that are induced can be related to the mid plane strains $\{\varepsilon^0\}_{x,y}$ and curvatures $\{k\}_{x,y}$ through Equation 1 for the case of no external mechanical loading and the laminate not being constrained during manufacture [3], [49].

$$\begin{Bmatrix} N^{TH} \\ M^{TH} \end{Bmatrix} = \begin{bmatrix} A & B \\ B & D \end{bmatrix} \begin{Bmatrix} \varepsilon^0 \\ \kappa \end{Bmatrix} , \qquad \text{Equation 1}$$

where A, B and D are the extensional, coupling and bending stiffness matrices respectively.

The thermal stresses and moment resultants per lamina k can be expressed in terms of the lamina stiffness matrix [Q], coefficient of thermal expansion α, distance from mid-plane z, lamina thickness t and the difference between curing and operating temperatures ΔT. These expressions are given in Equation 2 and Equation 3 [3].

$$\{N^{TH}\}_{x,y} = \sum_{k=1}^{n} [Q]_{x,y}^{k} \{\alpha\}_{x,y}^{k} \Delta T \cdot t_k \ . \qquad \text{Equation 2}$$

$$\{M^{TH}\}_{x,y} = \sum_{k=1}^{n} [Q]_{x,y}^{k} \{\alpha\}_{x,y}^{k} \Delta T \cdot z_k \cdot t_k \ . \qquad \text{Equation 3}$$

The residual stresses due to thermal effects in lamina k are given in Equation 4.

$$\{\sigma^{TH}\}_{x,y} = [Q]_{x,y}^{k} \left(\{\varepsilon^{0}\}_{x,y} + z\{k\}_{x,y} - \{\alpha\}_{x,y}^{k} \Delta T\right) \ . \qquad \text{Equation 4}$$

Camanho et al investigated the bearing strength of titanium / carbon FMLs used for bolted joints under static loads [35]. The investigation was motivated by the need for the mechanical fastening of composite components used in aerospace applications. The drawback of this joining technique for composites is that the material typically has a low bearing strength, which is further exacerbated by the sensitivity of the bearing strength to the laminate orientation. The strength issue is normally addressed by means of additional plies of composite materials being applied in the area of the bolted connection. This method results in an increase in both laminate thickness and mass, and may also add further eccentricity to single lap joints. The alternative method that was investigated was to apply the local reinforcement by substituting composite laminae with titanium foil. This method, shown in Figure 19, is intended to increase the bearing strength and reduce the laminate orientation sensitivity while adding no extra thickness to the laminate.

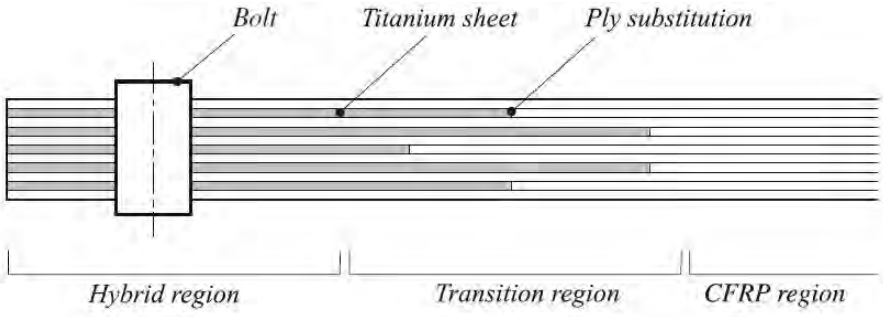

Figure 19: Hybrid joint for a bolted connection [35]

The titanium selected for the joint was a meta-stable beta-alloy Ti-15V-3Cr-3Sn-3Al. This alloy was selected over Ti 6Al-4V primarily due to the better cold workability, thereby allowing for easier manufacture of the thin foils. The carbon fibre reinforced epoxy was a uni-directional pre-impregnated type with the designation of M40-J/CYCOM 977-2.

Both physical test specimens and numerical models were evaluated [35]. The test specimens were manufactured by direct placement of the composite plies and titanium foils without the addition of adhesive. The titanium foils were treated chemically with the bonding enhancer AC Tech AC-130.

The numerical analysis was carried out using the Abaqus finite element software. The model consisted of 8 node continuum shell elements. The model of the test specimen had a high level of mesh refinement in the region of the bolt hole, with a lower level of refinement away from it, as can be seen in Figure 20.

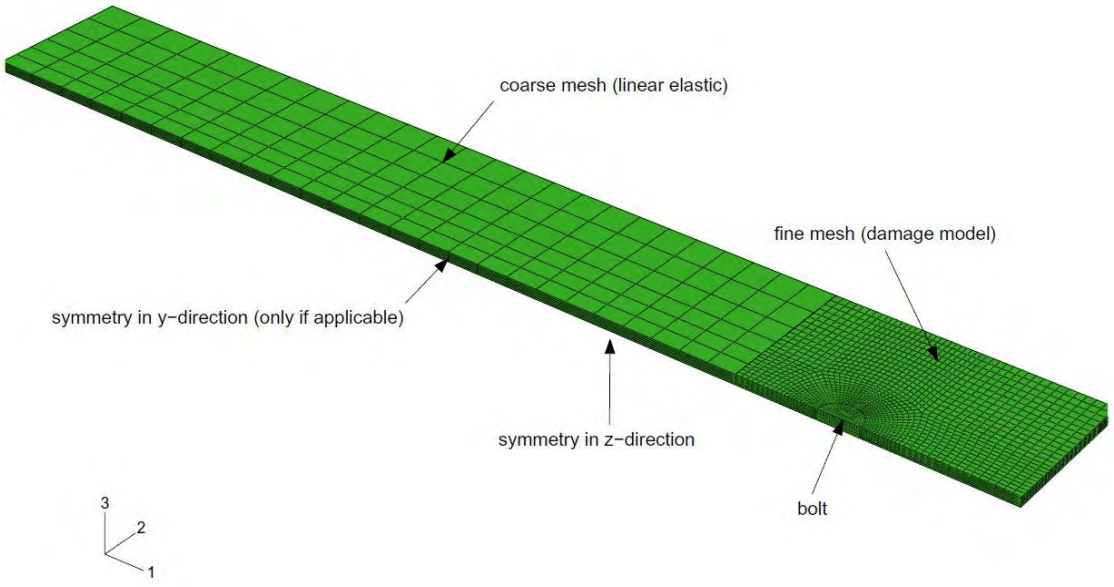

Figure 20: FE model of a bearing test specimen [35]

A progressive failure model was implemented in Abaqus for the area of high mesh refinement [35]. This model used the Hashin failure criterion, which is a pre-existing model in Abaqus, for the carbon / epoxy material. An elastic-plastic material model was used for the titanium foils with the von Mises criterion to predict the onset of plasticity. Isotropic hardening behaviour was used to predict the plastic flow.

The predictions and tests were carried out for a carbon / epoxy specimen without titanium as a reference and also for a variety of carbon / titanium specimens [35]. Figure 21 shows the results for a carbon only specimen (a) as well as a carbon / titanium specimen (b).

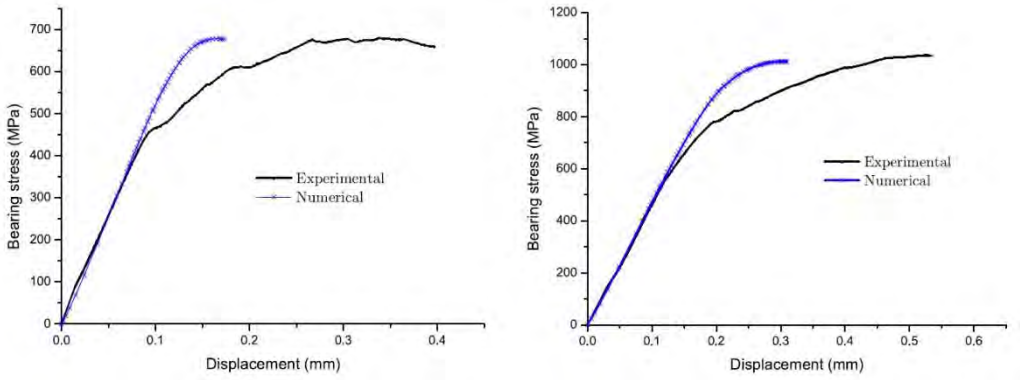

a) Carbon only specimen b) Carbon / titanium specimen

Figure 21: Experimental and test results for bearing behaviour [35]

The Abaqus models had good correlation with the test results when predicting the maximum bearing load that the joint can sustain before failure [35]. The prediction of the elastic limit was reasonable, although with a higher error than was the case for the prediction of the maximum loads. The reason for the errors in the prediction of the elastic loads was stated as being due to the Abaqus damage model, where this model only applies to plane stress conditions. An additional factor was that the Hashin criteria does not account for the contribution of shear stresses to fibre kinking, resulting in an over-prediction of the elastic limit. A micrograph of such a specimen is given in Figure 22 to illustrate the extent of fibre kinking.

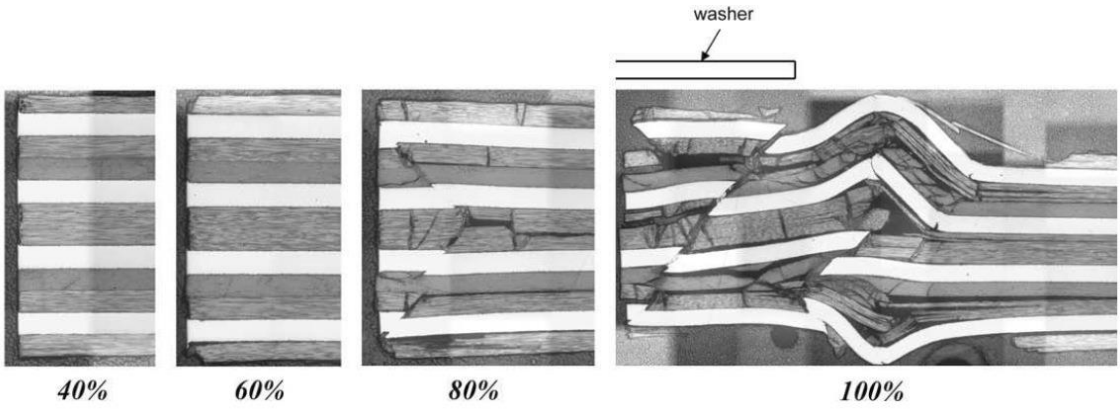

Figure 22: Micrograph of FML under bearing loading [35]

The principle of using titanium foil ply substitution for improving the bearing properties of carbon laminates was taken further by Fink et al [37]. The payload adapter of the EADS CASA VEGA space launch vehicle was chosen as a sample structure to investigate the practical application of the method. The carbon / epoxy adapter was fastened to aluminium joints in such a fashion that the fastening method can account for one quarter of the

component mass. This made the component a good candidate for the optimization of the joint configuration. The component and the details of the bolted attachment to the adapter ring are given in Figure 23.

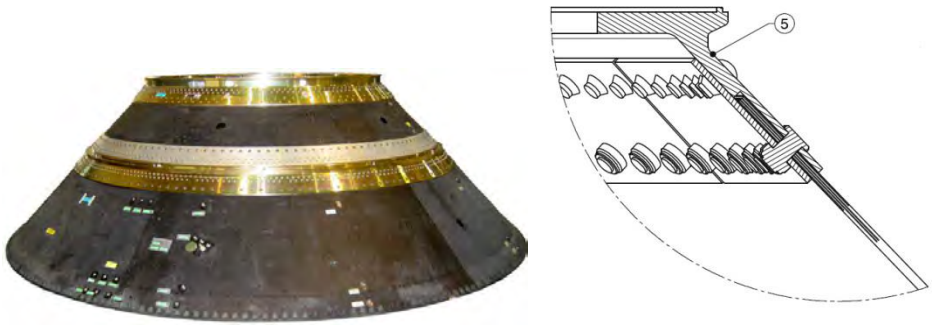

a) Overall structure of conical adapter b) Bolted assembly

Figure 23: Launch vehicle payload adapter [37]

The composite material used for the study was a carbon / epoxy M40-J/CYCOM 977-2, while the titanium alloy was T-15V-3Cr-3Sn-3Al. These are the same materials that were selected by Camanho et al [35], with similar motivations being given for the selection. The analysis was carried out using a specially modified version of the FASTCOMP computer code, which was developed by IN-EGI under European Space Agency Funding. The FASTCOMP software includes the YAFC and Langley Research Centre 03 (LaRC03) failure criteria for the composite materials [50]. One aspect of the LaRC03 criterion that is of relevance to bearing analysis is the incorporation of the interaction between compressive and shear stresses [51]. Fink et al [37] did not subsequently correlate the predictions made in the design phase with the final tests carried out for the development of the payload adapter.

2.3 Determination of Laminate Mechanical Properties

The mechanical properties, and specifically the stiffness matrices, of an FML are required as an input to the calculation of the failure modes. The mechanical properties of the global FML laminate can be determined from the individual properties of the constitutive layers. An overview of the procedure to calculate the mechanical elastic properties of a laminate is shown in Figure 24. Each step is discussed in this section and the specific relationships used in the final numerical failure model are given.

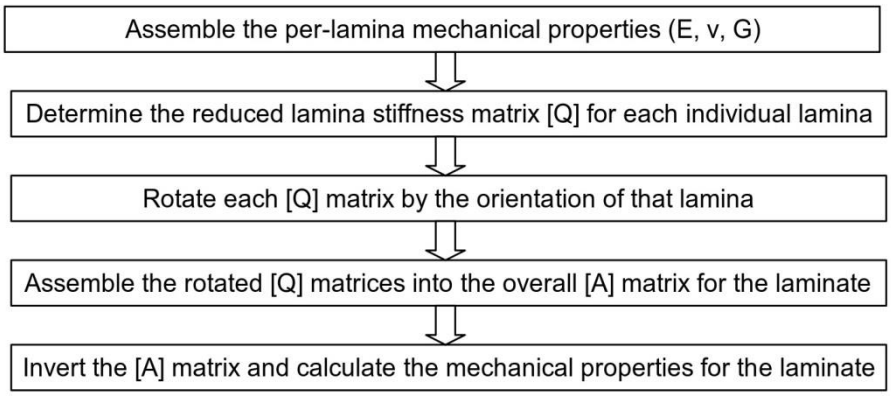

Figure 24: Calculation procedure for laminate mechanical properties

2.3.1 Lamina Mechanical Properties

The first step in determining the FML elastic properties is to assemble the mechanical properties for the individual laminae in the principal material directions. The following properties are needed, where the subscript 1 denotes the fibre direction in the case of the composite and the subscript 2 denotes the direction transverse to the fibres:

E_1: Young's Modulus in the 1 direction
E_2: Young's Modulus in the 2 direction
ν_{12}: Poisson's Ratio in the 12 direction
ν_{21}: Poisson's Ratio in the 21 direction
G_{12}: In-plane shear modulus

2.3.2 Lamina [Q] Matrix

The Q matrix is known as the reduced lamina stiffness matrix [52], or alternatively the plane stress-reduced stiffness matrix [53]. It can be defined in terms of the lamina stresses and strains, as shown in Equation 5, from (2.134) of [54] and (1.3.71) of [53].

$$\begin{Bmatrix}\sigma_1\\ \sigma_2\\ \sigma_6\end{Bmatrix} = \begin{bmatrix}Q_{11} & Q_{12} & Q_{16}\\ Q_{12} & Q_{22} & Q_{26}\\ Q_{16} & Q_{26} & Q_{66}\end{bmatrix}\begin{Bmatrix}\varepsilon_1\\ \varepsilon_2\\ \varepsilon_6\end{Bmatrix} . \qquad \text{Equation 5}$$

The terms in the [Q] matrix for an orthotropic material are described in (1.3.72) of [53] and (2.139) of [54]. These are given in Equation 6.

$$
\begin{aligned}
Q_{11} &= \frac{E_1}{1-\nu_{12}\nu_{21}} \quad , \\
Q_{12} &= \frac{\nu_{12}E_2}{1-\nu_{12}\nu_{21}} \quad , \\
Q_{22} &= \frac{E_2}{1-\nu_{12}\nu_{21}} \quad , \\
Q_{66} &= G_{12} \quad , \\
Q_{16} &= Q_{26} = 0 \quad .
\end{aligned}
$$

Equation 6

The above relationships are for uni-directional materials. Table 2.12 of [54] also presents the relationships for woven fabrics.

2.3.3 Rotated [Q] Matrix

An individual lamina may be rotated by an angle of θ away from the principal direction of the overall laminate. The elements of the rotated Q matrix are given in equation 11 of [52] and equation 2.4.8 of [53].

$$
[\overline{Q}] = \begin{bmatrix} \overline{Q}_{11} & \overline{Q}_{12} & \overline{Q}_{16} \\ \overline{Q}_{21} & \overline{Q}_{22} & \overline{Q}_{26} \\ \overline{Q}_{16} & \overline{Q}_{26} & \overline{Q}_{66} \end{bmatrix} \quad . \qquad \text{Equation 7}
$$

The components of this matrix are given in Equation 8.

$$
\begin{aligned}
\overline{Q}_{11} &= Q_{11}m^4 + Q_{22}n^4 + 2m^2n^2(Q_{12} + 2Q_{66}) \quad , \\
\overline{Q}_{12} &= m^2n^2(Q_{11} + Q_{22} - 4Q_{66}) + (m^4 + n^4)Q_{12} \quad , \\
\overline{Q}_{16} &= [Q_{11}m^2 - Q_{22}n^2 - (Q_{12} + 2Q_{66})(m^2 - n^2)]mn \quad , \\
\overline{Q}_{22} &= Q_{11}n^4 + Q_{22}m^4 + 2m^2n^2(Q_{12} + 2Q_{66}) \quad , \\
\overline{Q}_{26} &= [Q_{11}n^2 - Q_{22}m^2 + (Q_{12} + 2Q_{66})(m^2 - n^2)]mn \quad , \\
\overline{Q}_{66} &= (Q_{11} + Q_{22} - 2Q_{12})m^2n^2 + Q_{66}(m^2 - n^2)^2 \quad , \\
\overline{Q}_{21} &= \overline{Q}_{12} \quad , \\
\overline{Q}_{61} &= \overline{Q}_{16}\overline{Q}_{62} = \overline{Q}_{26} \quad ,
\end{aligned}
$$

Equation 8

where: $m = \cos\theta$,

$n = \sin\theta$.

2.3.4 Laminate [A] Matrix

All of the rotated Q matrices for the individual laminae can be assembled into an overall stiffness matrix for the laminate. This is given in equation 26 of [52] :

$$[\mathrm{A}] = \sum_{\mathrm{i}=1}^{\mathrm{K}} \left[\overline{\mathrm{Q}}\right]^{\mathrm{i}} (\mathrm{z_i} - \mathrm{z_{i-1}}) \quad ,$$

$$[\mathrm{B}] = \frac{1}{2} \sum_{\mathrm{i}=1}^{\mathrm{K}} \left[\overline{\mathrm{Q}}\right]^{\mathrm{i}} (\mathrm{z^{2_i}} - \mathrm{z^{2_{i-1}}}) \quad , \qquad \text{Equation 9}$$

$$[\mathrm{D}] = \frac{1}{3} \sum_{\mathrm{i}=1}^{\mathrm{K}} \left[\overline{\mathrm{Q}}\right]^{\mathrm{i}} (\mathrm{z^{3_i}} - \mathrm{z^{3_{i-1}}}) \quad ,$$

where: K = Total number of plies,
z_i is defined in Figure 25.

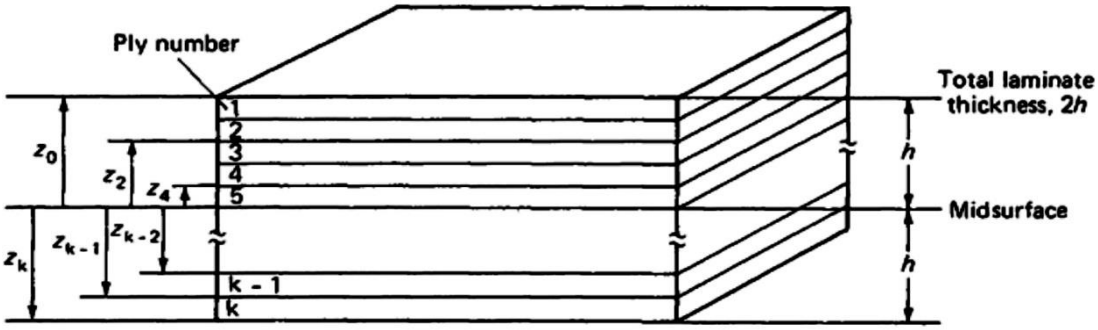

Figure 25: Laminate construction [52]

2.3.5 Laminate Mechanical Properties

The overall laminate mechanical properties may be derived from the elastic compliance matrix [a], which is the inverse of the [A] matrix:

$$[\mathrm{a}] = [\mathrm{A}]^{-1} \quad . \qquad \text{Equation 10}$$

A suitable procedure for the inversion is given in [55] :

$$
\begin{aligned}
|A| &= \left(A_{11}A_{22} - A_{12}^2\right)A_{66} + 2A_{12}A_{26}A_{16} - A_{11}A_{26}^2 - A_{22}A_{16}^2 \ , \\
a_{11} &= \frac{\left(A_{22}A_{66} - A_{26}^2\right)}{|A|} \ , \\
a_{22} &= \frac{\left(A_{11}A_{66} - A_{16}^2\right)}{|A|} \ , \\
a_{12} &= \frac{(A_{16}A_{26} - A_{12}A_{66})}{|A|} \ , \\
a_{66} &= \frac{\left(A_{11}A_{22} - A_{12}^2\right)}{|A|} \ , \\
a_{16} &= \frac{(A_{12}A_{26} - A_{22}A_{16})}{|A|} \ , \\
a_{26} &= \frac{(A_{12}A_{16} - A_{11}A_{26})}{|A|} \ .
\end{aligned}
$$

Equation 11

The mechanical properties can now be calculated according to equation 28 of [52] :

$$
\begin{aligned}
E_x &= \frac{1}{2ha_{11}} \ , \\
E_y &= \frac{1}{2ha_{22}} \ , \\
G_{xy} &= \frac{2}{2ha_{66}} \ , \\
\nu_{xy} &= -\frac{a_{12}}{a_{11}} \ .
\end{aligned}
$$

Equation 12

2.4 Material Failure Criteria

The material failure criteria for both the composite and the titanium constituents will be selected from existing work. Due to the wide range of potential composite failure criteria this aspect will be dealt with in some detail.

2.4.1 Overview of Composite Failure Criteria

Composite failure criteria in their most general form are mathematical expressions based on the stress tensor Σ which applies to the area of interest. The expression also incorporates experimentally derived mechanical properties for the material [56].

The general expression for the failure criteria will take the form:

$$f(\Sigma) \leq 1 \quad . \qquad \text{Equation 13}$$

The case of equality being achieved in Equation 13 defines a boundary surface or failure envelope in stress space [56], beyond which material failure is taken as having occurred.

Sun et al [57] categorizes failure criteria into three overall groups;

- Limit criteria: The lamina stresses or strains in the longitudinal, transverse and shear directions are separately compared with the tested mechanical strengths in those directions. The interaction between the stresses is not considered.
- Interactive criteria: A single polynomial equation of second order or higher that incorporates all of the stresses or strains is used to predict the failure envelope of the material. The failure criteria of this type typically incorporate a ratio of the stresses for the analysis to the measured strengths in order to arrive at relationship in the form of Equation 13.
- Separate mode criteria: Separate relationships are used for the matrix and fibre failures. These relationships may be in the form of a single stress component or alternatively include interaction effects through the use of several different stress to strength ratios.

Camanho [58] defines two overall categories of failure criteria,

- Failure criteria not associated with failure modes: These criteria include polynomial and tensor expressions, and correspond to the interactive criteria described by Sun et al [57]. The expressions are adjusted to match strength curves obtained by experiment.
- Failure criteria associated with failure modes: This category includes two sub-categories. The first is the non-interactive criteria where no interaction between the stresses or strains acting on the laminate are considered. This category corresponds to the limit criteria given by Sun et al. The second sub-category contains the interactive criteria, which are the same as the separate mode criteria of Sun et al.

Hinton et al [59] defines the categories for failure criteria in a similar fashion to Camanho, and also notes the emerging field of damage mechanics based criteria that aims to predict the entire failure process in the material.

A considerable number of failure criteria for composite materials have been proposed over last 50 years [59]. Review papers on the topic of composite failure criteria identify the most prevalent criteria by looking at the frequency of their occurrence in the literature. Commonly occurring failure criteria are summarised below in order to provide an overview of the field. These criteria will be classified according to the category groupings provided by Sun et al [57]. The Hashin criterion will also be included since this method is often applied to FMLs, albeit those made from materials other than titanium / carbon and typically subjected to impact loads rather than static loads [60], [61], [62], [63], [64]. The criteria are presented relative to their groupings are given in Table 5.

Table 5: Groupings and descriptions of failure criteria

Criteria Grouping	Criterion Designation	Example References	Notes on Criteria
Limit criteria	Maximum Stress	[54]	Frequently applied to orthotropic and transversely isotropic laminates
	Maximum Strain	[54]	Similar to the maximum stress criterion with similar applications
	Puck Simplified	[65], [66]	Separate limits for longitudinal fibre and transverse matrix failure without interaction
Interactive criteria	Tsai-Hill	[67]	Derived from the Hill criterion for anisotropic materials
	Tsai-Wu	[68]	Difficult to apply due to the required material properties. Simplifications exist
	Puppo-Evenson	[69]	Allows for the analysis of an entire laminate through the use of simple per-lamina calculations
Separate mode criteria	Grant Sanders	[66]	Uses several discrete terms to evaluate the failure due to different modes. More material characterisation required than for most criteria
	Hashin	[70], [71]	Defines four discrete failure modes for the laminate. A general version for three dimensional stress states and a simplified in-pane version exist

2.4.2 Evaluation of Composite Failure Criteria

The selection of the most applicable composite failure criterion for the analysis of FMLs requires a study of existing comparisons done between the different criteria. There are a

number of comparisons of composite failure criteria in the literature, where the World-Wide Failure Exercise [59] (WWFE) is of particular note. This exercise originated in 1991 as an assembly of international experts on the subject “Failure of Polymeric Composites and Structures: Mechanisms and Criteria for the Prediction of Performance”. The organisers of the meeting were the UK Science and Engineering Research Council and the UK Institution of Mechanical Engineers. The purpose of the event was to establish confidence in the methods used for predicting the failure of fibre reinforced polymer composites. Two immediate key findings emerged, namely that there was a lack of confidence in the failure criteria that were then in use and also that there was no universal definition for what qualified as a failure in composites.

One of the contributing factors to the lack of maturity of predictive methods was that the methods were generally used in practice only for calculating the initial sizes of composites panels. Thereafter experimental means were used to determine the design allowable strengths for structures. This practice is particularly widespread in the aerospace industry, where large databases of test results have been established. Smaller industries may follow a similar strategy, but with reduced amounts of testing together with higher safety factors to lower the development costs. The drawback of this approach is that the testing takes up time and adds noticeably to the cost of development [59].

The original assembly that led to the WWFE concluded that three overall aims needed to be addressed [59]:

- Investigate the existing theories for the failure prediction in fibre reinforced plastics in order to determine the level of maturity of these theories. This was the main theme of the subsequent survey.
- Bring the knowledge of the theoreticians in the field and the designers closer together.
- Develop more robust and accurate means of predicting failure that the designers would have confidence in.

These aims were realised in a two-phase survey that ran over twelve years. Splitting the investigation into two phases allowed for an initial blind test where the authors of the theories had no insight into how their work compared to the others. The authors were given feedback as part of the second phase and were allowed to refine their theories in order to further the science. These two phase were known as Part A and Part B [59].

Part A of the study started with the authors of the various theories being presented with the detailed specifications of a number of test cases for which they were required to provide failure predictions [59]. Invited papers on the foremost failure theories were collated. These papers contained detailed descriptions of the failure theories and the failure predictions for the test cases that had been set. The organisers of the WWFE used these papers to compare the methodologies of each theory that was presented and the accuracy of the predictions contained in the papers.

Part B of the study saw each of the participants being presented with the detailed experimental results of the test cases for which they had made predictions [59]. Each participant then presented a second paper containing a comparison of their predictions to the experimental results, a discussion of the comparison and any subsequent refinements to their theories, if desired. The various theories and the correlation with experiment in the second group of papers were then compared. The validity of each theory was then ranked. Any shortfalls in both the theories and the experimental results were noted.

The theories included in the survey fell into several overall categories, including [59]:

- Interactive failure theories,
- Physically based criteria,
- Damage mechanics,
- Standard design codes,
- Commercial software.

The list of participants and the theories that they supported are given in Table 6. The vendors of commercial finite element software declined to participate in the survey. The result was that the implementations of the composite failure analysis methods in the various software packages remain untested. The US AIAA Composites Structures Subcommittee conducted an industry survey to identify the failure theories most commonly used by designers [72]. The conclusion was that 90% of the respondents used the Maximum-Stress theory, Maximum-Strain theory or one of several quadratic polynomial theories. All of these theories are well represented in the WWFE [73].

Table 6: Summary of contributors and theories for the WWFE (derived from [59])

Contributor	Approach Represented	Theory Designation
Bogetti	Maximum strain theory	Bogetti
Chamis	ICAN and CODSTRAN software	Chamis
Cuntze	Failure modes Concept (FMC)	Cuntze
Eckold	British Standard pressure vessel codes BS4994	Eckold
Edge	In-house design method	Edge
Hart-Smith	Generalised Tresca theory	Hart-Smith(1)
Hart-Smith	Maximum strain theory	Hart-Smith(2)
Hart-Smith	Ten-per-cent rule	Hart-Smith(3)
Huang	Micromechanics, Generalised maximum stress	Huang
Mayes and Hansen	Multi-continuum theory	Mayes
McCartney	Physically based damage mechanics	McCartney
Puck and Schuermann	3-D phenomenological model	Puck
Rotem	Interactive matrix and fibre failure theory	Rotem
Sun	Linear analysis	Sun (Linear)
Sun	Non-linear (FE based) analysis	Sun (Non-Linear)
Tsai	Interactive quadratic failure criterion	Tsai
Wolfe and Butalia	Maximum strain energy method	Wolfe
Zinoviev	Development of Maximum stress theory	Zinoviev

The experimental data for the test cases was derived from literature searches and notices placed in journals and conference proceedings calling for good quality test data to be forwarded to the organisers. A total of fifteen test cases were identified that would challenge the theories while exploring a range of fundamental issues related to the response of composite materials [59], [74]. The test cases are summarised in Table 7.

Table 7: Summary of laminate test cases (Derived from [59], [74])

Test Case	Laminate lay-up	Material	Description of Required Prediction
1*	0°	E-glass/LY556 epoxy	σ_y versus τ_{xy} envelope
2*	0°	T300/BSL914C carbon/epoxy	σ_x versus τ_{xy} envelope
3*	0°	E-glass/MY750 epoxy	σ_y versus σ_x envelope
4*	(± 30°/90°)	E-glass/LY556 epoxy	σ_y versus σ_x envelope
5*	(± 30°/90°)	E-glass/LY556 epoxy	σ_x versus τ_{xy} envelope
6*	(0°/ ± 45°/90°)	AS4/3501–6 carbon/epoxy	σ_y versus σ_x envelope
7	(0°/ ± 45°/90°)	AS4/3501–6 carbon/epoxy	Stress-strain curves for σ_y :σx =1:0
8	(0°/ ± 45°/90°)	AS4/3501–6 carbon/epoxy	Stress-strain curves for σ_y :σ_x =2:1
9*	±55°	E-glass/MY750 epoxy	σ_y versus σ_x envelope
10	±55°	E-glass/MY750 epoxy	Stress-strain curves for σ_y :σ_x =1:0
11	±55°	E-glass/MY750 epoxy	Stress-strain curves for σ_y :σ_x =2:1
12	(0°/90°)	E-glass/MY750 epoxy	Stress-strain curves for σ_y :σ_x =0:1
13	±45°	E-glass/MY750 epoxy	Stress-strain curves for σ_y :σ_x =1:1
14	±45°	E-glass/MY750 epoxy	Stress-strain curves for σ_y :σ_x =1 :–1
15	± 55°	E-glass/MY750 epoxy	Stress variation and development of failure in a tube under pressure

* Biaxial failure stress envelopes

Part A of the survey included a direct comparison of the different theories to each other. The criteria for comparison included the failure models used and the number of different types of failure modes that the theory attempts to address. The inclusion of the prediction of non-

linear effects and thermal stresses was also of relevance. The reliance on software codes or numerical methods was also noted [59].

Part B of the exercise focussed more on how closely the predictions of individual theories compared to experimental data. Here the theories were ranked according to their predictive accuracy against the test data and any shortcomings were noted. The refinements introduced by the authors of the theories in light of the comparison during part B of the exercise were also noted. A total of eleven of the participants elected to revise their theories [59].

A qualitative assessment of the theories was carried out in accordance with a ranking system. The ranking system rated weaknesses into categories, namely Minor, Significant and Fundamental. These theories were then split into the three groups, as shown in Table 8, according to the following criteria [74]:

- Group 1: Good predictive capabilities, with at most only one fundamental weakness and predominantly minor weaknesses. In this grouping the Bogetti theory was regarded as the most marginal since it had the largest number of weaknesses and inaccuracies in the strength prediction of a unidirectional lamina.
- Group 2: A higher number of significant and fundamental weaknesses were present.
- Group3: A significant number of fundamental weaknesses or test cases that were outside the predictive capability of the theories.

Table 8: Grouping of failure theories (Derived from [59], [74])

Group	Theories	General characteristics
1	Puck, Zinoviev, Tsai, Sun (Linear), Cuntze, Bogetti	Exhibiting good predictive capability, none or one fundamental weakness and many relatively minor weaknesses
2	Edge, Chamis, Wolfe, Rotem, Mayes, Huang, Hart-Smith	Having a few more significant and fundamental weaknesses.
3	Eckold, McCartney, Hart-Smith, Sun (Non-linear)	Having clear limitations and many fundamental weaknesses and /or test cases not solved.

An additional quantitative assessment was done where the predictive capabilities of the theories were compared to five major categories of lamina response that were split into a total of 125 ranking cases [59], [74]:

- Predicting the biaxial strength of a unidirectional laminate: The Tsai, Cuntze, Wolfe-B and Chamis theories showed the best performance.

- Predicting the initial failure of multi-directional laminates: Some doubts were expressed about the ability of the theories to predict the initial failure of laminates. This was of particular concern when predicting the stress-strain curves of test case 12 of Table 7. The better performers were the Bogetti, Zinoviev and Wolfe-B theories.
- Predicting the final failure strengths of multi-directional laminates: The best performing theories were those of Puck, Cuntze, Tsai-B and Zinoviev, primarily due to their modelling of the post-initial failure response of the laminates. The paucity of experimental data in the compression-compression quadrant meant that the theories could not be validated for that case.
- Predicting the deformation of multi-directional laminates: The majority of the theories were incapable of predicting the matrix dominated non-linear deformation of angle ply specimens. The Puck and Zinoviev approaches gave the best overall correlation, while the Puck, Cuntze and Bogetti approaches gave the best predictions at moderate strain levels. After implementing refinements to the model in part B of the exercise the Cuntze theory received an improved rating.
- Prediction of a selection of general features: A total of 41 quantifiable features of composite failure were identified, for example the specific modes of failure. Cuntze's theory proved to be the best at predicting these features, followed by Puck.

The quantitative assessment process gave the top ranking to the Zinoviev, Bogetti, Puck and Cuntze theories, with very similar final scores.

The organisers also published their impressions on the best overall failure theories for use by designers. One consideration was that the recommended theories should avoid providing for an unsafe design through being non-conservative, while at the same time avoiding an uneconomic design through being too conservative [59], [75].

The Puck, Cuntze and Tsai theories were recommended for the prediction of the response of a lamina, with the possible simultaneous use of the theories also being proposed. The recommendations for the prediction of initial failure were less well defined. This was due to the lack of reliable test data, uncertainty over whether the recorded first failure in tests properly corresponded with the initial failure mode of the relevant theory and the theoretical treatment of residual thermal stresses. The organisers declined to make a recommendation for this case, although the theories of Bogetti and Zinoviev gave the best correlation with test data, with the caveat that these theories ignore the effect of thermal stresses. The prediction

of the final strength of multidirectional laminates was better defined, with the organisers recommending the Puck and Cuntze theories [59], [75].

The various selection processes from the WWFE as discussed above are summarised in Table 9 to aid in the selection of the failure model most applicable to the FML modelling for this work.

Table 9: WWFE selection processes and recommended failure models

WWFE Selection Process	Recommended Failure Models
Qualitative assessment for models showing no fundamental weaknesses and exhibiting good predictive capabilities	Puck, Zinoviev, Tsai, Sun (Linear), Cuntze, Bogetti
Quantitative assessment against a range of lamina responses	Zinoviev, Bogetti, Puck, Cuntze
Recommendations for designers for the prediction of lamina response under combined loading	Puck, Cuntze, Tsai
Recommendations for designers for the prediction of final strength	Puck, Cuntze

The recommendations summarised in Table 9 point to both the Puck and Cuntze theories being applicable to a wide range of laminate configurations and loading conditions while being identified in all of the selection processes. The Puck model poses some challenges when it comes to practical application due to the requirements for material properties that are not normally available and are difficult to test for. This leads to the Cuntze criterion being selected for application to the FML failure modelling for this work.

A failure criterion that was not evaluated in the WWFE that also requires consideration is the Puck modified theory. This theory was proposed at the Fokker-VFW alliance and was propagated in the Engineering Sciences Data Item number 83014 [66]. The Puck modified method entered use in the South African and international aerospace industry, however, the method remains largely unreported in the literature. Examples of the use of the theory in the South African context include the design of the OVID aircraft and a carbon-fibre drop tank, both of which demonstrated good structural integrity during testing [76].

The confidence in the method is also evidenced by the publications of the European Cooperation for Space Standardization (ECCS) [77]. The ECCS publishes standards to which contractors working for the European Space Agency must adhere to in order to improve standardization in the European space sector. The handbook that prescribes the design calculation methods that must be used for launch vehicles and spacecraft [78] explicitly allows for the use of the Puck modified criterion for laminated composites

These considerations lead to two composite failure criteria being selected for application to FML failure modelling for this work, namely the Cuntze and Puck modified criteria.

2.4.3 Description of Selected Composite Failure Criteria

The selected composite failure criteria, namely the Cuntze and Puck modified methods, are presented below.

The Cuntze Failure Criterion:

The notation normally used for the Cuntze criterion is in accordance with the German guideline VDI 2014, which is summarised in Figure 26. This notation will be used to present the criterion.

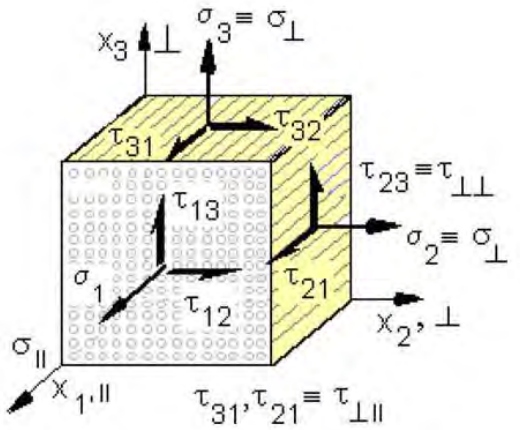

Figure 26: Stress notations of an element in a UD laminate [79]

The lamina element of Figure 26 can now be given the context of a lamina k within an overall laminate subjected to a 2D stress state, as shown in Figure 27.

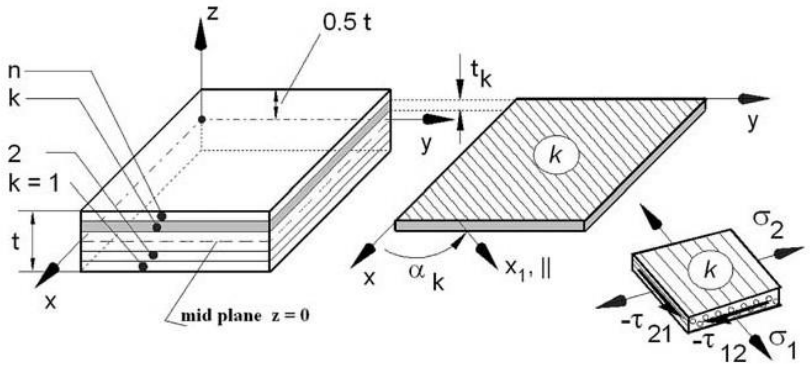

Figure 27: Laminate in a state of plane stress [79]

There are also five uni-directional strengths associated with the lamina depicted in Figure 26, which are [79]:

- $R_{\parallel}^{t}$: Tensile strength parallel to the fibre direction
- $R_{\parallel}^{c}$: Compressive strength parallel to the fibre direction
- $R_{\perp}^{t}$: Tensile strength transverse to the fibre direction
- $R_{\perp}^{c}$: Compressive strength transverse to the fibre direction
- $R_{\parallel\perp}$: Shear strength transverse / parallel to the fibre direction

The nomenclature of these strengths can take two overall forms [79]:

- R: The mean or typical strength
- $\overline{R}$: The statistically based design allowable strength.

Cuntze defines his failure criteria in terms of his Failure Mode Concept (FMC) [79]. This concept introduces a number of criteria for a uni-directional lamina that can be used to determine of the failure mode of the lamina and ultimately the laminate. The FMC groups lamina failures into two overall categories, namely Fibre Failure (FF) and Inter Fibre Failure (IFF), where the IFF modes are also sometimes referred to as matrix failure [79], [80]. The IFF mode normally indicates the onset of failure in a laminate, while FF is normally associated with the final failure [80]. These two general failure categories are then expanded into five specific failure modes [79], [80], which are also shown in Figure 29:

- FF1: Fibre failure under tension,
- FF2: Fibre failure under compression,
- IFF1: Matrix failure under transverse tension,

- IFF2: Matrix failure under shear,
- IFF3: Matrix failure under transverse compression. This mode causes a wedge shaped failure surface, as indicated in Figure 29. Further compression on the lamina may then cause an out-of-plane displacement which may result in local delamination or buckling of adjacent laminae, as shown in Figure 28. These effects on the surrounding laminae may initiate final failure.

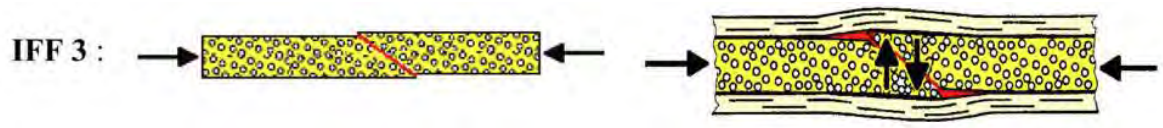

Figure 28: IFF3 wedge type failure [79]

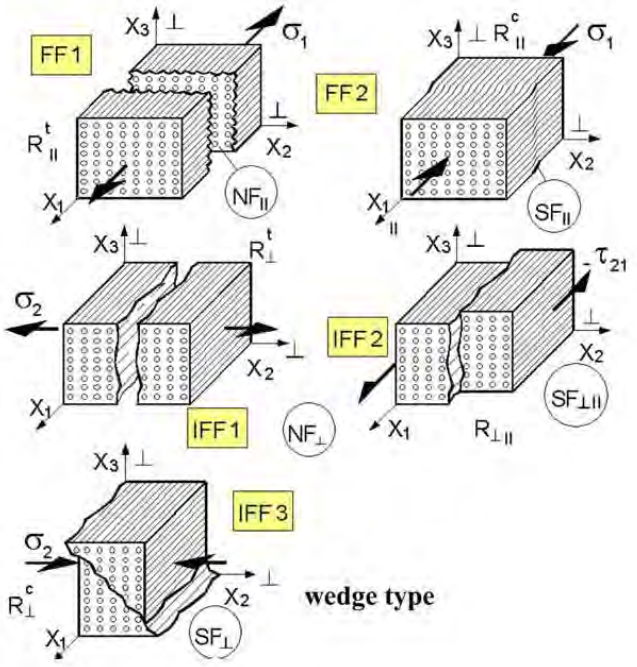

Figure 29: FMC fracture modes [79]

The stresses shown in Figure 26 are used to define five invariants that are chosen to best represent the multi-axial behaviour of the composite material [80].

$$
\begin{aligned}
I_1 &= \sigma_1 \ , \\
I_2 &= \sigma_2 + \sigma_3 \ , \\
I_3 &= \tau_{31}^2 + \tau_{21}^2 \ , \\
I_4 &= (\sigma_2 - \sigma_3)^2 + 4\tau_{23}^2 \ , \\
I_5 &= (\sigma_2 - \sigma_3)(\tau_{31}^2 - \tau_{21}^2) - 4\tau_{23}\tau_{31}\tau_{21} \ .
\end{aligned}
$$

Equation 14

The use of curve parameters derived from material tests is inherent to the derivation of failure criteria. Cuntze states that such criteria are most suitable for practical engineering applications if the number of curve parameters required are minimised, while the computational resources required are also kept low [79]. The failure criterion should also directly describe the physical effects on the lamina. These requirements led to the definition of a failure mode concept that requires only three experimentally derived points for the curve parameters [80].

Each of the five distinct failure modes can be characterised by a failure function F, where the condition for failure within that mode is achieved when F(σ) = 1 [79] .

$$
\begin{aligned}
&\text{FF1: } F_{\parallel}^{\sigma} = \frac{I_1}{\bar{R}_{\parallel}^{t}} \ , \\
&\text{FF2: } F_{\parallel}^{\tau} = \frac{-I_1}{\bar{R}_{\parallel}^{c}} \ , \\
&\text{IFF1: } F_{\perp}^{\sigma} = \frac{I_2 + \sqrt{I_4}}{2\bar{R}_{\perp}^{t}} \ , \\
&\text{IFF2: } F_{\perp\parallel} = \frac{I_3^{3/2}}{\bar{R}_{\perp\parallel}^{3}} + b_{\perp\parallel}\frac{I_2 I_3 - I_5}{\bar{R}_{\perp\parallel}^{3}} \ , \\
&\text{IFF3: } F_{\perp}^{\tau} = (b_{\perp}^{\tau} - 1)\frac{I_2}{\bar{R}_{\perp}^{c}} + \frac{b_{\perp}^{\tau}\sqrt{I_4}}{\bar{R}_{\perp}^{c}} \ .
\end{aligned}
$$

Equation 15

Equation 15 contains two curve parameters, namely $b_{\perp\parallel}$and $b_{\perp}^{\tau}$. These parameters may be obtained from multi-axial test data in a stress domain appropriate to the parameters. This may be done at a single pre-selected calibration point on each of the two curves, with several specimens tested for each of these calibration points. A more rigorous approach would be to apply curve fitting through the entire test range by means of a regression analysis [81]. The appropriate test data is applied to Equation 16 to determine the curve parameters [80].

$$b_{\perp\parallel} = \frac{1 - \left(\frac{\tau_{21}^{\perp\parallel}}{\overline{R}_{\perp\parallel}}\right)^2}{\frac{2\sigma_2^c \cdot \tau_{21}^{\perp\parallel 2}}{\overline{R}_{\perp\parallel}^3}} \text{ from } \left(\sigma_2^c, \tau_{21}^{\perp\parallel}\right) \ ,$$

$$b_{\perp}^{\tau} = \frac{1 + \frac{(\sigma_2^{cr} + \sigma_3^{cr})}{\overline{R}_{\perp}^c}}{\frac{(\sigma_2^{cr} + \sigma_3^{cr})}{\overline{R}_{\perp}^c} + \frac{(\sigma_2^{cr} - \sigma_3^{cr})^2}{\overline{R}_{\perp}^{c^2}}} \ .$$

Equation 16

The curve parameters may also be determined by experience if there is a lack of bi-axial test data. Cuntze has refined his estimates for the acceptable ranges for the parameters over the course of several publications and selected the range given in Equation 17 as being suitable for GFRP, CFRP and AFRP composites [79].

$$0.05 < b_{\perp\parallel} < 0.2 \ ,$$
$$1.0 < b_{\perp}^{\tau} < 1.1 \ .$$

Equation 17

An engineering approach is recommended in [81] for the cases where sufficient bi-axial test data is not available. The curve parameters are reduced to their simplest form, namely $b_{\perp\parallel}$=0 and $b_{\perp}^{\tau}$=1. It is noted that this simplification may result in an underestimate of the lamina strength in the case of bi-axial compression. This approach was adopted for the modelling of FML failure in this work due to the lack of suitable bi-axial material data.

Puck Modified Criterion

The original failure models for composite materials were extensions of continuum models. Puck was the first researcher to formulate a mechanics-based approach to predict the strength of composite materials [82]. This theory presents separate equations for the failure of the fibres and the matrix. These two failure equations are superimposed upon each other within a single lamina, and do not interact with each other, although the stress components of a load condition may interact to arrive at an overall failure mode.

The original, or simplified, Puck criterion is based on the assumption that longitudinal failure in a uni-directional lamina occurs in the fibres and can be predicted by the longitudinal stress only [65]. Similarly the transverse failures will be in the matrix and can be predicted using the

normal and shear stresses. The original form of the criterion as expressed in the Engineering Sciences Data Unit 83014 [66] is given in Equation 18.

$$\sigma_1 = X_t \text{ or } -X_c \ ,$$
$$\text{or } \left(\frac{\sigma_2}{Y}\right)^2 + \left(\frac{\sigma_6}{Q}\right)^2 = 1 \ , \qquad \text{Equation 18}$$

where:

- X_t = Allowable in-plane stress in the fibre direction in tension,
- X_c = Allowable in-plane stress in the fibre direction in compression,
- Y_t = Allowable in-plane stress transverse to the fibre direction in tension,
- Y_c = Allowable in-plane stress transverse to the fibre direction in compression,
- Y = Y_t or Y_c depending on the sign of σ_2,
- Q = Allowable in-plane shear stress,
- σ = The lamina stresses which are defined in Figure 30.

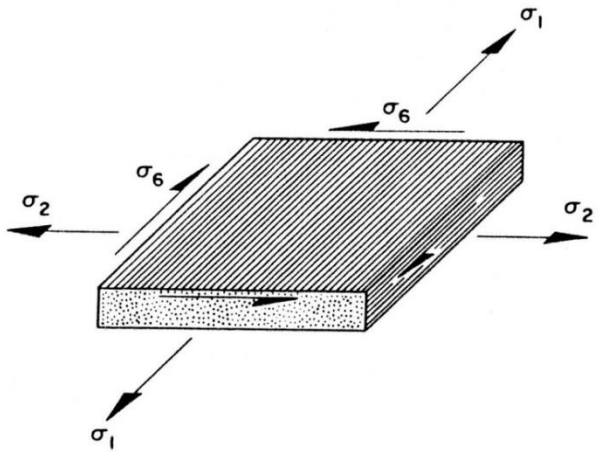

Figure 30: Lamina stress directions for the Puck failure criterion [66]

A modified Puck criterion was proposed for cases where there may be notable differences between the tensile and compressive strengths of the material in the transverse direction. This modified theory describes an ellipse through the transverse tensile, compressive and the shear strengths of the material [66]. The theory is given in Equation 19.

$$\sigma_1 = X_t \text{ or } X_c \ ,$$
$$\frac{\sigma_2^2}{Y_t Y_c} + \sigma_2\left(\frac{1}{Y_t} - \frac{1}{Y_c}\right) + \left(\frac{\sigma_6}{Q}\right)^2 = 1 \ . \qquad \text{Equation 19}$$

The Puck modified criterion, as given in Equation 19, is used in this work.

2.4.4 Titanium Failure Criteria

The analysis of failure in a metal first requires a definition of failure. The common definitions for failure are yielding and fracture. The evaluation of criteria will therefore include the selection of a failure theory including yield and fracture criteria. These criteria must be based on the stress in the material to ensure analytical compatibility with the failure criteria for the composite materials.

The failure criteria proposed for the analysis of metals have most typically used either the principal stresses or the maximum shear stresses as the indicator of failure. The Rankine Theory, also known as the maximum normal stress criterion, uses the maximum principal stress in the material. The initiation of the inelastic deformation of a material is taken as the point at which the maximum principal stress due to the applied loads reaches the yield strength of the material [83].

The Tresca Theory for ductile materials differs from the Rankine Theory by using the maximum shear stress for failure prediction [83], and is thereby also referred to as the maximum shear stress criterion. The theory predicts failure when the maximum shear stress in the material due to the applied loads reaches the maximum shear stress in a tensile test specimen of the same material at the point where yield is taken to have occurred, as expressed in Equation 20. The physical basis of the theory is that the yielding mechanism of metals is due to slip in the crystal planes. This is a shear deformation phenomenon which is driven by the shear stress in the material [84].

$$\tau_o = \tau_{max} \text{ (at yielding)}. \qquad \text{Equation 20}$$

The von Mises theory determines the distortion energy of the material at yield and is mathematically identical to the octahedral shear stress yield criterion. The theory is also referred to as the distortion energy criterion [83]. This criterion determines the shear stress on the octahedral planes and defines failure as occurring when a critical limit is achieved.

The physical basis of the von Mises theory is that yielding does not occur in a material under hydrostatic stress. A plane is defined where this stress occurs as a normal stress and the

remaining shear stress then defines the failure criterion [84]. The shear stress on the octahedral planes is defined in terms of the principal normal stresses σ_1 ,σ_2 and σ_3.

$$\tau_h = \frac{1}{3}\sqrt{(\sigma_1 - \sigma_2)^2 + (\sigma_2 - \sigma_3)^2 + (\sigma_3 - \sigma_1)^2}. \quad \text{Equation 21}$$

Failure is predicted when the octahedral shear stress reaches a critical value τ_{ho}. This critical shear stress may be defined in terms of the normal yield strength σ_0 from tensile test data [84].

$$\tau_{ho} = \frac{\sqrt{2}}{3}\sigma_0. \quad \text{Equation 22}$$

The phenomenological models described above are applied to the analysis of failure due to either yield or fracture. The Rankin model is generally not favoured due to an inability to predict the behaviour of the material when the two principal stresses are of different signs. The Tresca and von Mises criteria are therefore the most commonly used, even though these also have some limitations. Both of these theories have drawbacks when predicting the behaviour in all four quadrants of the biaxial stress state. Due to this limitation the modelling of plastic flow in a material may be better predicted through nonlinear distortion energy criteria or the Hill criterion [83].

The Tresca and von Mises criteria give identical results only under special cases, for example pure tension. The results from the two criteria are however always within 15% of each other, with the Tresca criterion being the most conservative [83].

A comparison has been made between a number of failure theories, including some not discussed here, for aluminium alloys [85]. These theories include constant equivalent strain, Xue-Wierzbicki, Wilkins, Johnson-Cook, CrachFEM, maximum shear stress and the fracture forming limit. These theories were all compared under conditions of plane strain. This restriction allowed for a direct mapping between the stress and strain spaces, thereby allowing for criteria formulated in terms of both stress and strain space to be directly compared. The comparison between the multi-axial test results and the predictions of the failure theories was carried out according to two requirements, namely performance and cost. The performance was the accuracy of the theory in predicting the test results, while the cost was the number of calibration tests required for the material to generate the data needed for the theory. The maximum shear stress criterion was found to be the best

according to these requirements. This criterion followed the test results with a good degree of accuracy and also needed only one test for calibration. The primary drawback that was noted was that the criterion does not apply to axisymmetric loading conditions.

Stroughton and Yoon [86] provided additional corroboration for the maximum shear stress criteria when applied to aluminium alloys. The maximum shear stress criterion showed very good correlation with test data. An additional finding was that the criterion is not strongly related to the test specimen geometry, but rather the stress state. The criterion has also been applied to steels by Tachibana and Iyoku [87] due to the prescriptions in some nuclear design codes for the method of elastic-plastic analysis. The investigation of the applicability of failure theories to titanium alloys has seen less attention, although Wang [88] has noted that the formation of the adiabatic shear banding in the material appears to be in accordance with the maximum shear stress criterion.

The maximum shear stress criterion will be applied to the failure analysis of fibre metal laminates in this work due to the confidence expressed in the method. An overview of the criterion is given below [84], [89].

The maximum shear stress is defined as being the largest of the three principal shear stresses [84]. The principal shear stresses are expressed in terms of the principal normal stresses in Equation 23.

$$\tau_1 = \frac{|\sigma_2 - \sigma_3|}{2} \quad ,$$
$$\tau_2 = \frac{|\sigma_1 - \sigma_3|}{2} \quad , \qquad \text{Equation 23}$$
$$\tau_3 = \frac{|\sigma_1 - \sigma_2|}{2} \quad .$$

The yield criterion can therefore be stated, where τ_0 is the shear yield stress:

$$\tau_o = \mathrm{MAX}\left(\frac{|\sigma_1 - \sigma_2|}{2}, \frac{|\sigma_2 - \sigma_3|}{2}, \frac{|\sigma_3 - \sigma_1|}{2}\right) (\text{at yielding}) \quad . \qquad \text{Equation 24}$$

The shear yield stress τ_0 is normally determined from the uniaxial tensile yield stress σ_0. In a uniaxial test the following stress state applies:

$$\sigma_1 = \sigma_{0,}, \qquad \sigma_2 = \sigma_3 = 0 \ . \qquad \text{Equation 25}$$

Substitution of Equation 25 into Equation 24 yields the maximum shear stress in terms of the tensile stress.

$$\tau_o = \frac{\sigma_0}{2} \ . \qquad \text{Equation 26}$$

Equation 24 may now be expressed in terms of σ_0.

$$\frac{\sigma_o}{2} = \text{MAX}\left(\frac{|\sigma_1 - \sigma_2|}{2}, \frac{|\sigma_2 - \sigma_3|}{2}, \frac{|\sigma_3 - \sigma_1|}{2}\right) \text{(at yielding)} \ , \qquad \text{Equation 27}$$

or alternatively,

$$\sigma_o = \text{MAX}(|\sigma_1 - \sigma_2|, |\sigma_2 - \sigma_3|, |\sigma_3 - \sigma_1|) \text{ (at yielding)} \ . \qquad \text{Equation 28}$$

The maximum shear stress criterion is shown graphically in Figure 31 for a state of plane stress where $\sigma_3 = 0$. Any points outside of the hexagon are subject to yielding.

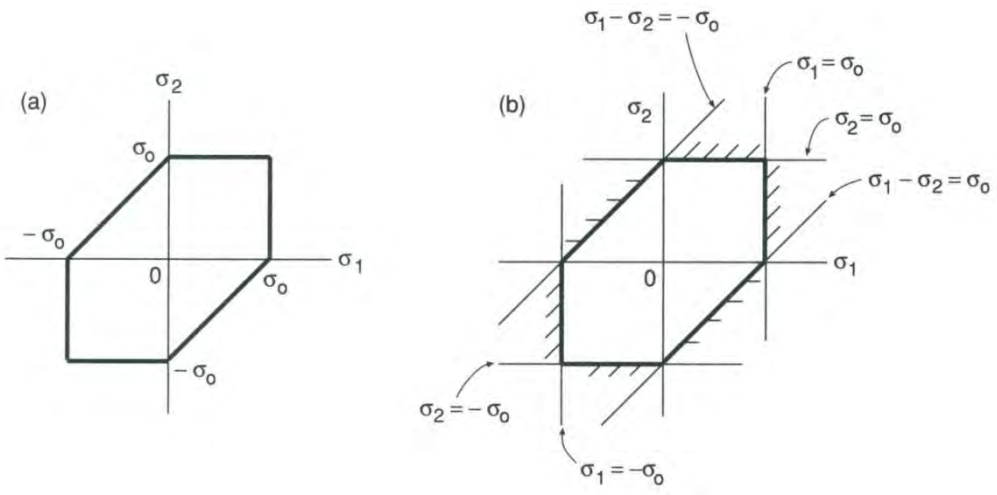

Figure 31: Failure locus for the maximum shear stress criterion [84]

The material of interest in this work for the post-yield modelling is titanium 6Al-4V. This alloy exhibits nearly ideal elastic-perfectly plastic behaviour, with minimal work hardening resulting in a relatively abrupt transition between the elastic and plastic states [90], [91], [92]. The adoption of this model is further supported by the tensile test results presented in section 3.3.2.

The elastic-perfectly plastic behaviour model can be defined as the stress-strain relationship being flat beyond yielding, with no increase in stress beyond this point [84]:

$$\sigma = E\varepsilon \ (\sigma \leq \sigma_0) \ ,$$
$$\sigma = \sigma_0 \ \left(\varepsilon \geq \frac{\sigma_0}{E}\right) \ . \qquad \text{Equation 29}$$

2.5 Proposed Degradation Model

Software was developed for this thesis to carry out the failure analysis of the fibre metal laminates through the embodiment of the selected constituent material failure criteria. The input to the software is the overall configuration of the laminate, including the metal and composite constituents, the material properties and the ratio of the loads acting on the laminate. The output is a progressive analysis of the failure modes in the laminate as the loading on it increases, from the point of initial failure up to final failure. The matrix and fibre failure modes in the composite constituents are differentiated from each other, where both the Puck modified and Cuntze criteria were implemented to allow for this the prediction of the different failure modes. The overall methodology for determining the failure progression is similar to that of ESDU 84018 [93] and the ECCS Handbook 32-20 Part 2A [78].

The first step in the analysis is the calculation of the laminate stiffness matrices that will be used for the subsequent lamina loading calculations. Provision has been made to allow for the analysis of the case where an unbalanced laminate that has been held flat for storage, transport or handling during manufacture. The moments required to hold the laminate flat are calculated and applied. Any resin damage that may result from this action is then used to remove the resin stiffness from the affected laminae before the main analysis commences. The moments used to hold the laminate flat are not re-applied for the main failure analysis since they constitute a separate load case prior to the main loading that will induce failure.

The loads are then applied in the specified ratio. The loading is increased to the point where the selected failure criterion indicates the first occurrence of damage in a lamina. The relevant stiffness for this lamina is removed from the overall laminate stiffness. The stiffness to be removed will depend on whether the failure is in the composite matrix or fibre, or else in the metal. A composite matrix failure is taken to be in-plane and both the transverse and shear stiffness contributions are removed from the lamina. In this case the fibres will retain

stiffness in their longitudinal direction and the integrity in the through-thickness shear direction will also be retained.

The failure analysis for the laminate is re-run at the same load with the reduced stiffness to determine if any further failure progression will occur. Once the damage progression in the laminate has stabilised a check is done to see if total laminate failure has occurred. In the case of exclusively composite matrix failures the load is increased further until another lamina failure is predicted. The same process is followed to stabilise the failure progression in the laminate and the sequence is repeated until total laminate failure occurs. The software was verified by means of alternative spreadsheet based calculations that were carried out on some instances of the mechanical test sample analysis that is presented in Section 3.2.3. The results from both methods were in agreement.

2.6 Conclusions on the Numerical Modelling

The derivation of a progressive static failure model to predict the behaviour of a titanium / carbon FML requires the inclusion of several existing analytical models from the literature into the overall failure model. These existing models include those for determining the failure of each of the titanium and carbon-fibre material constituents, in addition to determining the overall stiffness of the FML.

A requirement of the failure models for the material constituents is that these models can differentiate between failure modes, thereby allowing for the inclusion of progressive damage prediction into the global model for the FMLs. The models for carbon-fibre specifically should be able to differentiate between matrix and fibre failure under all potential loading conditions to satisfy this criterion. A study of the existing literature led to the selection of both the Cuntze and Puck modified models for this thesis. The selection of a failure model for the titanium 6Al-4V alloy was approached by both a study of existing literature and mechanical testing to confirm the applicability of existing criteria to this alloy. The outcome of this process was the selection of the maximum shear stress criterion for this work. The method for determining the stiffness of the FML is the classical laminate theory from existing work. The existing failure and stiffness models are incorporated into an overall progressive failure model for this thesis. In this model the load on the FML is increased to the point where a failure event is predicted. The stiffness associated with the predicted failure is removed from the stiffness of the overall FML and the process is repeated until complete failure of the FML occurs.

Chapter 3. Mechanical Testing of Fibre Metal Laminates

3.1 Introduction to Mechanical Testing

The mechanical testing of Fibre Metal Laminates (FMLs) is carried out to verify the progressive failure analysis model. The specimens are tested in a laboratory environment so that the predicted failure modes may be compared with the test results. Different failure modes are induced by means of test specimens with several laminate configurations.

The overall specimen geometry is fixed through the identification of a suitable test standard, while the thickness is determined in order to minimise the influence of free-edge stresses. With the geometry fixed the progressive failure model is then used to determine the lamination angles for three types of test specimens that will exhibit different failure modes. The tests are carried out such that the maximum data can be gathered for the determination of all the failure modes occurring in the specimens. The data gathered includes strain, extension, acoustic events, micrographic examination and X-Ray imagery. A comparison between the test results and the progressive failure predictions can then be made.

3.2 Test Specimen Design and Analysis

3.2.1 Selection of a Test Standard

The use of a standardised test method is desirable due to the standard methods having been well developed over time, as opposed to a non-standard method where considerable verification of the method would be required. There are currently no standard methods available specifically for FMLs, and therefore a method will be chosen from the standards that apply to metals and fibrous composites.

A representative standard for the tensile testing of metals is ASTM E 8M [94]. This standard prescribes a number of specimen geometries for different material types and manufacturing processes. These specimens can be grouped into two overall categories, namely flat specimens from plate or sheet and also round specimens. Due to the manufacturing methods required for FMLs the specimens would need to be flat. A typical flat specimen design from ASTM E 8M can be seen in Figure 32. This type of specimen has a reduced

cross sectional area, where the shoulder areas are of concern for the composite constituent of the FML laminate. The cutting of fibres in the shoulder areas may allow for stress concentrations that could then precipitate premature failure.

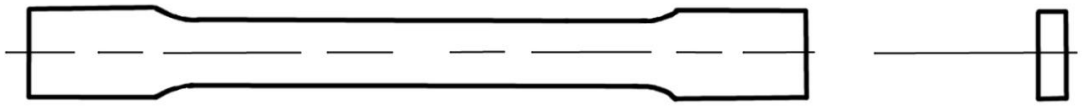

Figure 32: Rectangular tension test specimen from ASTM E 8M (derived from [94])

The representative standard for the tensile testing of composite materials is ASTM D3039 [95]. The specimen designs presented in this standard are all rectangular and vary primarily in the width and the tab arrangement. The specified widths are dependent on the material type. A typical tabbed specimen is shown in Figure 33. This type of specimen has a geometry that is intended to reduce the edge effects associated with composite tests, and therefore appears to be better suited to the testing of FMLs than the ASTM E 8M standard.

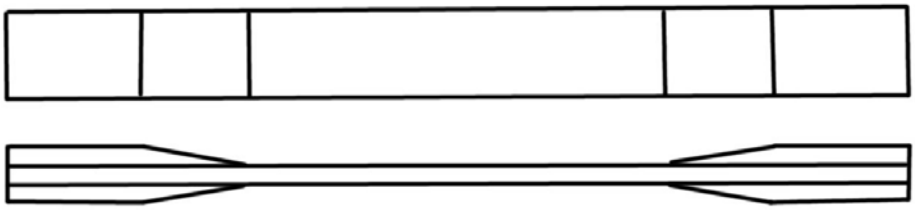

Figure 33: Tension test specimen from ASTM D3039 (derived from [95])

A review was carried out to determine what standards are applied to the static tensile testing of FMLs. Due to the scarcity of information on the carbon fibre / titanium type FMLs the review was extended to cover FMLs of all constituent types. A summary of the information relevant to the testing of this material type is presented in Table 10. Of note is the extensive usage of the ASTM D3039 test standard.

Table 10: Review summary of published static tensile tests

Author	Constituent Materials	Applied Standards	Specimen Details	Test Notes
Botelho [96]	Glass fibre reinforced epoxy and aluminium	ASTM D3039	Length: 247 mm Width: 25.4 mm Thickness: 2 mm Straight edged rectangular specimens.	Instrom test machine with a cross-head speed of 1.27 mm / minute. Strain was measured using a laser optical system.
Carillo [97]	Self-reinforced polypropylene composite and aluminium	ASTM D3039	A variety of specimen sizes were used to determine scaling effects. All were straight edged rectangular specimens.	Instrom screw-driven test machine with a constant stain rate of 0.04 per minute. An extensometer was used to monitor strain.
Iaccarino [98]	Glass fibre reinforced epoxy and aluminium	ASTM D3039	States that the specimens were ASTM D3039 compliant. Aluminium end tabs were used.	MTS servo-hydraulic test machine under displacement control at 2 mm / min. An extensometer was used to monitor strain.
Kawai [99]	Glass fibre reinforced epoxy and aluminium	JIS K7073 and ASTM D3039	Length: 200 mm Width: 20 mm Thickness: 1.44 mm Straight edged rectangular specimens with aluminium end tabs.	MTS servo-hydraulic test machine under displacement control at 1 mm / min. An extensometer was used to monitor strain.
Khalili [100]	Glass fibre reinforced epoxy and aluminium and steel	ASTM D3039	Straight edged rectangular specimens with end tabs.	Instrom test machine with a cross-head speed of 5 mm / min.
Lee [101]	Self-reinforced polypropylene composite and aluminium	ASTM D3039	Length: 175 mm Width: 25 mm Thickness: 2 mm Straight edged rectangular specimens.	Displacement control at 2 mm / min.
Moussavi-Torshizi [102]	Combined Kevlar and glass fibre reinforced epoxy and aluminium	ASTM D3039	Length: 175 mm Width: 25 mm Thickness: 2 mm Straight edged rectangular specimens.	Instrom test machine with a cross-head speed of 1 mm / min.
Vasumathi [103]	Combined jute and carbon fibres reinforced epoxy and aluminium or magnesium	ASTM D3039	Straight edged rectangular specimens.	Instrom test machine.
Xue [104]	Carbon fibre reinforced epoxy and aluminium	Non-standard	Length: 150 mm Width: 12.7 mm Thickness: 1.8 mm Straight edged rectangular specimens with end tabs.	MTS servo-hydraulic test machine under displacement control at 0.5 mm / min.

For the purposes of this work the ASTM D3039 standard will be adopted for the FML tests due to the minimisation of detrimental edge effects and the broad acceptance of the standard in publications.

3.2.2 Specimen Geometry

An important aspect of setting the specimen geometry is to determine the ratio of the thickness to width in order to minimise the negative impact of edge effects on the test results. Murthy and Chamis [105] investigated the effect of the free-edge delamination of composite test specimens as a function of the laminate width and thickness. This was a finite

element based investigation of four layer angle ply composite laminates at a variety of orientations. Typical results for the free-edge stresses, both interlaminar shear σ_{xz} and interlaminar normal stresses σ_{zz}, are shown in Figure 34.

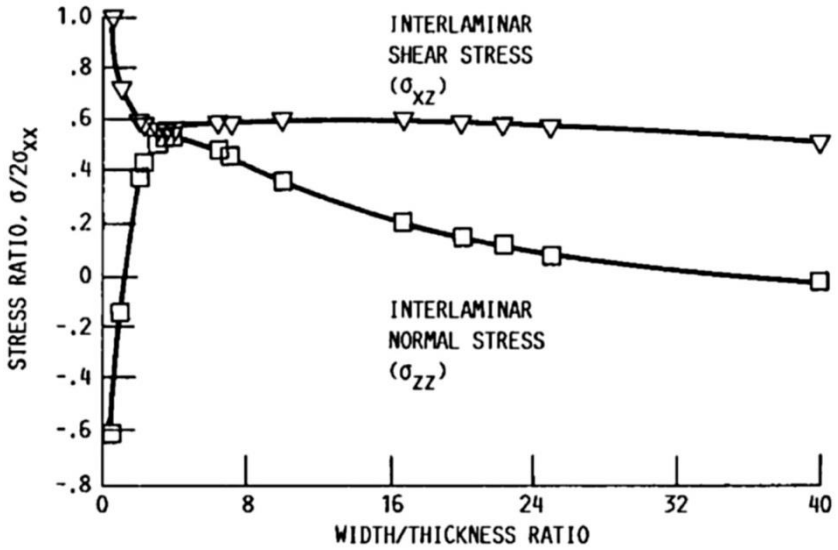

Figure 34: Width to thickness ratio effects of interlaminar free-edge stresses for a ±45° laminate [105]

The interlaminar normal stress σ_{zz} is compressive at a width to thickness ratio of less than 2 [105]. Once this ratio reaches 4, σ_{zz} reaches a peak and then reduces from that point on as the ratio increases. The interlaminar shear stress σ_{xz} is approximately constant for a width to thickness ratio of greater than 2, but increases rapidly when this ratio falls below 2. Murthy and Chamis [105] conclude that edge delamination is primarily driven by the interlaminar shear stress, but may also be triggered by the normal stress. The authors concluded that width to thickness ratios in the range of 4 to 8 give the highest values of the interlaminar normal stress.

The specimen guidelines supplied by ASTM [95] will be followed. These standards recommend a specimen width of 25 mm for balanced symmetric laminates. The titanium sheets available for the facings are 1 mm thick. The minimum number of carbon fibre plies that can be used to give a balanced layup of varying angles is four. The total specimen thickness is calculated in Table 11.

Table 11: Total specimen thickness

Layer Description	Layer Thickness (mm)
Titanium face sheet	1
Adhesive interface	0.13
Carbon fibre lamina	0.33
Carbon fibre lamina	0.33
Carbon fibre lamina	0.33
Carbon fibre lamina	0.33
Adhesive interface	0.13
Titanium face sheet	1
Laminate Total	***3.58***

This makes the width to thickness ratio 7.0, which is slightly less than the minimum of 8 prescribed in [105]. Examination of Figure 34 shows that the width to thickness ratio is outside of the values most severely affected by edge effects, and should therefore be acceptable. The isotropic nature of the titanium sheets may also make these bounding values of the aspect ratio conservative for the FML panels.

The final specimen dimensions can now be fixed, in accordance to [95]. These dimensions are given in Figure 35, Figure 36 and Table 12. Tabs are not included in the final specimen design given in Table 12 due to the clamping surface being metal rather than composite.

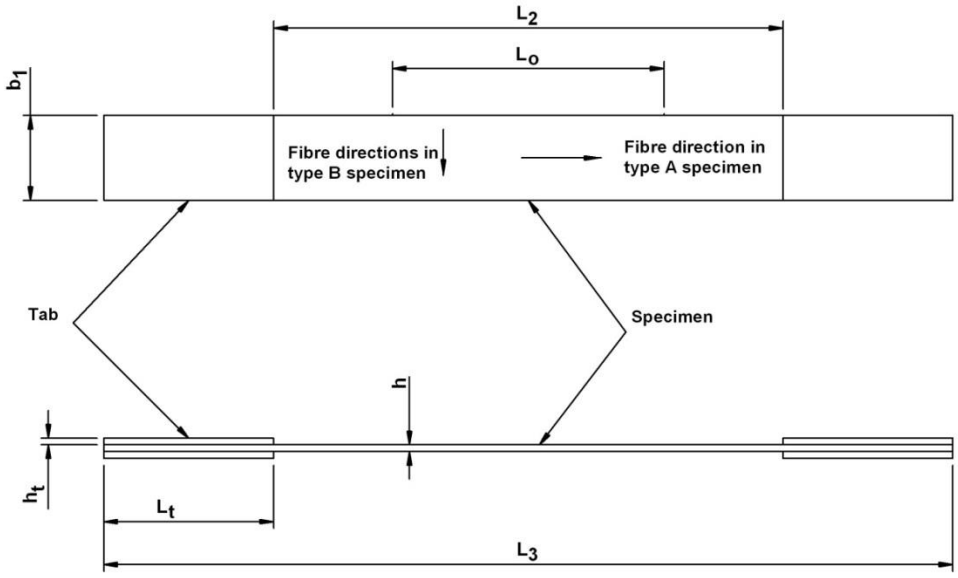

Figure 35: Specimen geometry and dimensions (derived from [95])

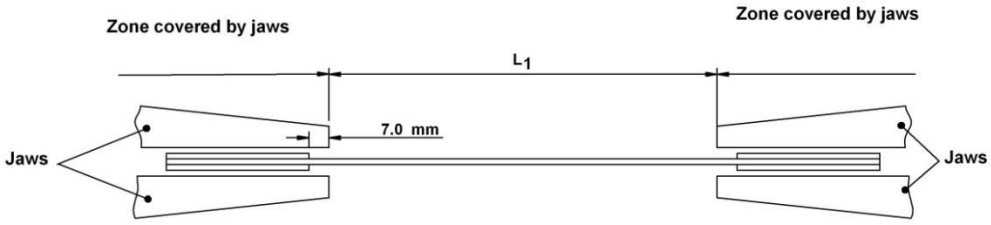

Figure 36: Specimen clamped in jaws (derived from [95])

Table 12: Specimen dimensions with reference to Figure 35 and Figure 36

Dimension	Description	Value (mm)
b_1	Width	25 ± 0.5
h	Thickness	3.58
L_0	Gauge length (b)	50 ± 1
L_1	Nominal initial distance between grips	136
L_3	Overall length (Nominal)	250

The specimens for the titanium material properties were given the same length and width as the FML specimens, and were made from the same 1 mm thick titanium sheet as used for the FML specimens. This was done to ensure that the properties derived from the tests for the titanium were applicable to the final FML tests.

3.2.3 Specimen Failure Analysis

The selection of the lamination angles for the composite constituent of the FML specimens was carried out by means of the application of the progressive failure model described in Chapter 2. The failure model was used to identify the laminate configurations that would result in different failure modes. One type of failure that was required for the tests was the case where the initial failure would not be catastrophic and the specimen would continue to carry further load up to the point of final failure. Another scenario was where the initial failure would simultaneously lead to the subsequent complete failure of the laminate.

The existing published mechanical properties for the FML constituent materials proved to be unsuitable for this study. This was due to the statistical analyses applied to the test results in order to arrive at safe values for design purposes, resulting in conservative values for the strength. The comparison between the progressive failure analysis done for this work and the subsequent test results requires the use of representative material strengths.

The properties of the carbon-fibre reinforced epoxy were taken from the CSIR test report "Sigratex KDU 1092 / Epolam 2022 UD carbon: Technology Innovation Agency Test Report" [106] and the average strengths were used. Several titanium specimens were tested for this work to generate input data for the failure analysis, as given in section 3.3.2. Where the compressive properties of the material are not known, these are set to the same values as the tensile properties. The properties used for the analysis are presented in Table 13.

Table 13: Material properties for analysis

Property	Sigratex KDU 1092 / Epolam 2022 UD carbon	Titanium 6Al-4V
Thickness of layer - t (mm)	0.33	1
Modulus of elasticity in the local 1 direction - E_1 (GPa)	93.12	122.09
Modulus of elasticity in the local 2 direction - E_2 (GPa)	7.169	122.09
In-plane shear modulus - G_{12} (GPa)	3.946	45.49
Longitudinal Poisson's ratio - ν_1	0.3060	0.342
Tensile strength in the local 1 direction - X_t (MPa)	1338.5	952.09
Compressive strength in the local 1 direction - X_c (MPa)	1338.5	952.09
Tensile strength in the local 2 direction - Y_t (MPa)	15.92	952.09
Compressive strength in the local 2 direction - Y_c (MPa)	15.92	952.09
In-plane shear strength - Q (MPa)	46.24	550

The numerical failure analysis for the test specimens was done using the previously developed software utilising both the Puck modified and Cuntze failure criteria, while using the material properties as given in Table 13. Various orientation angles of the carbon laminate are presented, with 0° corresponding with the longitudinal (load) direction of the test specimen.

The stress at which failure occurs is designated as σ_x, with the x direction corresponding with the longitudinal direction of the specimen. The stresses are presented for both the first failure and the final failure of the specimen. When the first failure is at a lower stress than the final failure, then the failure mode is inevitably cracking in the epoxy matrix. The final failure is always initiated by yield in the titanium face sheeting, followed by the failure of the carbon / epoxy layers. No failures were predicted in the adhesive between the carbon and the titanium. The analysis results at a variety of orientation angles for the carbon / epoxy in the FML are presented in Table 14.

A summary of this tabular data is also given in Figure 37. It can be seen that no initial matrix failure is predicted while the carbon laminate of the FML is aligned with the load direction. The Puck modified criteria predicts that matrix failure will start occurring before final failure at a lamination angle of approximately 30°. The Cuntze theory predicts that this will start

occurring at approximately 40°. The predicted stresses for both the initial and final failures decrease with an increase in the carbon lamination angle.

Table 14: Summary of specimen failure strength predictions

Carbon Orientation Angle (degrees)	Puck modified Criterion		Cuntze Criterion	
	σ_x First Failure (MPa)	σ_x Final Failure (MPa)	σ_x First Failure (MPa)	σ_x Final Failure (MPa)
0	862	862	862	862
10	845	845	845	845
20	798	798	798	798
30	732	732	732	732
31	705	710	725	725
33	637	695	712	712
35	578	680	699	699
37	526	666	686	686
40	459	646	602	646
45	374	617	448	617
50	314	596	354	596
60	242	573	255	573
70	208	569	212	569
80	193	572	193	572
90	188	574	188	574

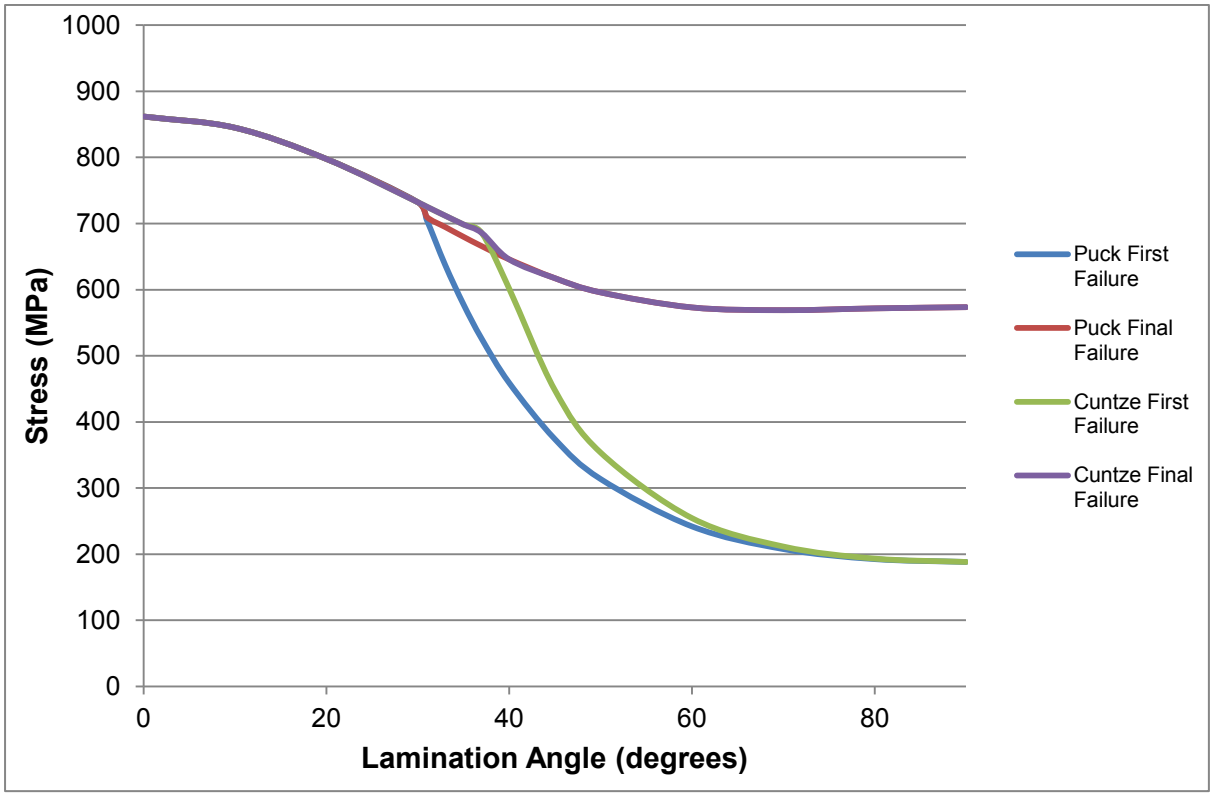

Figure 37: Predicted specimen failure stresses

3.2.4 Selection of Lamination Angles for Test Specimens

The lamination angles of the carbon / epoxy for the test specimens were selected such that various predicted failure modes could be investigated. Three lamination angles were chosen:

- 0°: This will test the case of the specimen undergoing final failure without any initial failures.
- 45°: This will test an intermediate state of initial failure occuring before final failure. The specific angle was chosen due to the widespread adoption of this lamination angle in industry.
- 90°: This will test the most extreme case of the specimen undergoing initial failure before subsequent final failure.

A typical cross section of the specimens is given in Figure 38, as given in the manufacturing drawings for the specimens.

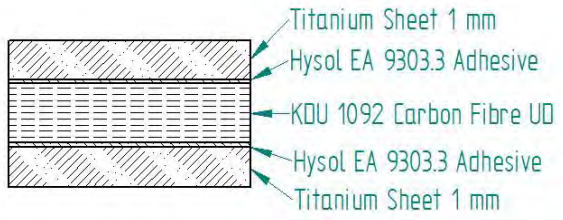

Figure 38 Schematic cross section of a typical specimen (not to scale), adapted from manufacturing drawings

The specific layup sequence for the specimens is given in Table 15 through Table 17. These tables are taken directly from the manufacturing drawings for the specimens.

Table 15: Layup sequence for the 0° specimens, adapted from manufacturing drawings

Layup Sequence for Specimen Type 1		
Layer Number	Material	Orientation (Degrees)
1	Titanium 6AL-4V 1mm thick	
2	Hysol EA 9309.3NA Adhesive	
3	Sigratex KDU 1092 UD Carbon / Epolam 2022	0
4	Sigratex KDU 1092 UD Carbon / Epolam 2022	0
5	Sigratex KDU 1092 UD Carbon / Epolam 2022	0
6	Sigratex KDU 1092 UD Carbon / Epolam 2022	0
7	Hysol EA 9309.3NA Adhesive	
8	Titanium 6AL-4V 1mm thick	

Table 16: Layup sequence for the 45° specimens, adapted from manufacturing drawings

Layup Sequence for Specimen Type 2		
Layer Number	Material	Orientation (Degrees)
1	Titanium 6AL-4V 1mm thick	
2	Hysol EA 9309.3NA Adhesive	
3	Sigratex KDU 1092 UD Carbon / Epolam 2022	45
4	Sigratex KDU 1092 UD Carbon / Epolam 2022	-45
5	Sigratex KDU 1092 UD Carbon / Epolam 2022	-45
6	Sigratex KDU 1092 UD Carbon / Epolam 2022	45
7	Hysol EA 9309.3NA Adhesive	
8	Titanium 6AL-4V 1mm thick	

Table 17: Layup sequence for the 90° specimens, adapted from manufacturing drawings

Layup Sequence for Specimen Type 3		
Layer Number	Material	Orientation (Degrees)
1	Titanium 6AL-4V 1mm thick	
2	Hysol EA 9309.3NA Adhesive	
3	Sigratex KDU 1092 UD Carbon / Epolam 2022	90
4	Sigratex KDU 1092 UD Carbon / Epolam 2022	90
5	Sigratex KDU 1092 UD Carbon / Epolam 2022	90
6	Sigratex KDU 1092 UD Carbon / Epolam 2022	90
7	Hysol EA 9309.3NA Adhesive	
8	Titanium 6AL-4V 1mm thick	

3.2.5 Specimen Manufacture

A variety of methods were evaluated for the manufacture of the specimens using the wet resin processes required by the selected carbon / epoxy system. These methods included both conventional hand lay-up and pre-wetting of the fibres, in addition to an initial investigation into the use of resin infusion moulding. Composite test specimens were manufactured using the different processes and were subjected to mechanical tensile tests for comparative evaluation. These tests were in accordance with ASTM D3039 [95]. A micrographic examination of the specimens was also carried out to determine the resin void content. The relative constituent content of the different specimens was then determined in accordance with ASTM D3171 [107]. In the latter case the ignition loss method of procedure G of ASTM D3171 [107] was employed in conjunction with density measurements in accordance with ASTM D792 [108]. The conclusion was that the process best suited to the composite aspect of the manufacture would be a wet hand-layup. This should be carried out by an experienced laminator using a laser alignment tool to ensure the accuracy of the fibre orientation both during the fabric cutting and the lamination.

The manufacture of the specimens was facilitated by machining slots in an aluminium block, where each slot was the size of a finished specimen. The individual specimens were manufactured in these slots, with the titanium, carbon-fibre and adhesive interlayers being co-cured. The specimens were allowed to cure at room temperature under a compaction load for 24 hours. The specimens were then post-cured at 80°C for two hours. The post-cure cycle was established by first determining the acceptable curing cycles for the adhesive and resin from the product literature. A thermal curing stress analysis was then carried out on the titanium / carbon laminate which was used as input to the failure analysis software. The post-cure cycle given above was determined as having minimal impact on the failure modes of the specimens while still being in keeping with the product curing guidelines for the polymeric materials. A finished test specimen is shown in Figure 39.

Figure 39: FML test specimen

3.2.6 Specimen Numbering

The specimen numbers consist of a prefix followed by a specimen identifier, with the two separated by a dash. The prefix gives the lamination angle of the carbon fibre constituent of the specimen. The prefix T0 represents a lamination angle of 0º, T45 indicates alternating layers at angles of ±45º and T90 indicates an angle of 90º. A total of three specimens were manufactured for each of the lamination angles and were given the identifiers A, B and C. The specimen numbering is summarised in Table 18.

Table 18: FML specimen numbering

Lamination Sequence	Specimen Numbers
0º as per Table 15	T0-A, T0-B, T0-C
±45º as per Table 16	T45-A, T45-B, T45-C
90º as per Table 17	T90-A, T90-B, T90-C

3.3 Mechanical Testing

3.3.1 Test Equipment

Specimen T90-A was tested using a Schenck H1724 load frame due to machine availability at the time. All of the other fibre metal laminate specimens were tested using a Schenck POZ 0857 load frame. The titanium specimens were tested in an Instron Model 1342 load frame. A summary is given in Table 19 and Figure 32. In all cases wedge type grips were used.

Table 19: Test machines used

	FML Specimen T90-A	All Other FML Specimens	All Titanium Specimens
Machine	Schenck H1724	Schenck POZ 0857	Instron Model 1342
Load Cell	Schenck, ±500 kN static capacity	Schenck, ±250 kN static capacity	Instron cat. No. 2518-101, ±50 kN static capacity
Controller	MTS FlexTest 40SF	MTS FlexTest 40SF	Instron FastTrack 8500 with Bluehill software

(a) Schenck H1724 (b) Schenck POZ 0857 (c) Instron Model 1342

Figure 40: Test machines

The load cell and strain gauge data for all specimens was acquired using an HBM MGCplus equipped with an AB22A display and control panel, an ML455 multi-channel amplifier, an ML460 amplifier plug-in module and three ML801B plug-in modules. All of the specimens tested with the Schenck POZ 0857 also had the data acquired in parallel via the MTS FlexTest 40SF controller. In the cases where two sets of data had been acquired for a single specimen, the data sets were compared to each other to ensure consistency. The Instron FastTrack 8500 controller was also used for the graphical presentation of the summary data of the titanium specimen tests. Figure 41 shows the primary data acquisition hardware used.

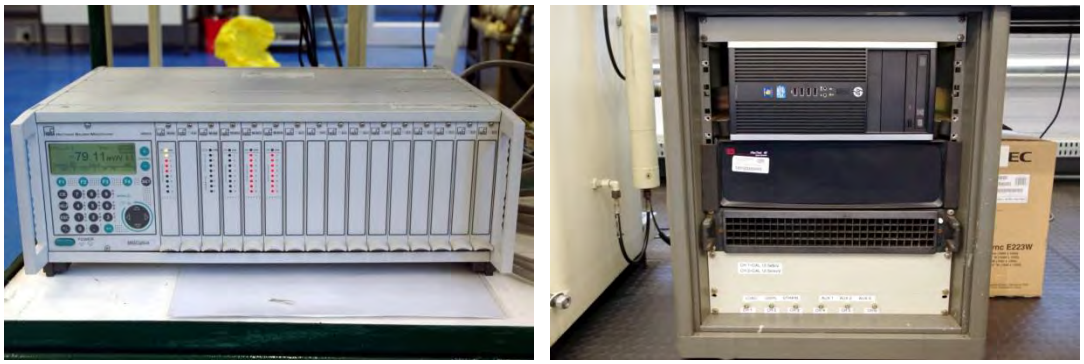

(a) HBM MGCplus (b) MTS FlexTest 40SF

Figure 41: Data acquisition equipment

All of the FML specimens were strain gauged with 350 ohm HBM gauges. This resistance was chosen in order to avoid any potential problems with localised Joule heating on the gauges. The titanium specimens were monitored using an Instron extensometer with a 25 mm gauge length. A Unitron Versamet-2 stereo microscope was placed next to the test machines for the failure monitoring of some of the specimens.

3.3.2 Titanium Tensile Test Results

The titanium specimens were tested in accordance with ASTM D3039 [95] to ensure that the material properties were derived using the same test procedures as the later FML tests. The testing was done under extension control at a rate of 2 millimetres / minute. The onset of yield was taken to be in accordance with the 0.2% offset strain line, which was calculated internally by the Instron FastTrack 8500 controller. The Young's modulus is the chord modulus which was determined between the 200 MPa and 600 MPa points. A summary of the test results is presented in Table 20.

Table 20: Summary of titanium tensile test results

Specimen Number	Area (mm^2)	Tensile stress at Yield (MPa)	Modulus (GPa)	Tensile stress at Maximum Load (MPa)	Elongation %
1	26.4	974.4	121.4	1020.6	5.99
2	26.9	963.4	118.4	1007.4	10.49
3	26.6	963.5	130.7	1008.6	9.88
4	27.2	931.1	118.9	977.0	9.78
5	26.5	928.2	121.1	973.4	8.96
Coefficient of Variation (%)	1.162	2.2061	4.0836	2.1006	19.73
Standard Deviation	0.311	21.004	4.986	20.951	1.78
Mean	26.7	952.1	122.1	997.4	9.02
Range	0.73	46.18	12.27	47.24	4.50
Maximum	27.2	974.4	130.7	1020.6	10.49
Minimum	26.4	928.2	118.4	973.4	5.99

Figure 42 shows the titanium stress vs. strain curves as presented by the Instron controller.

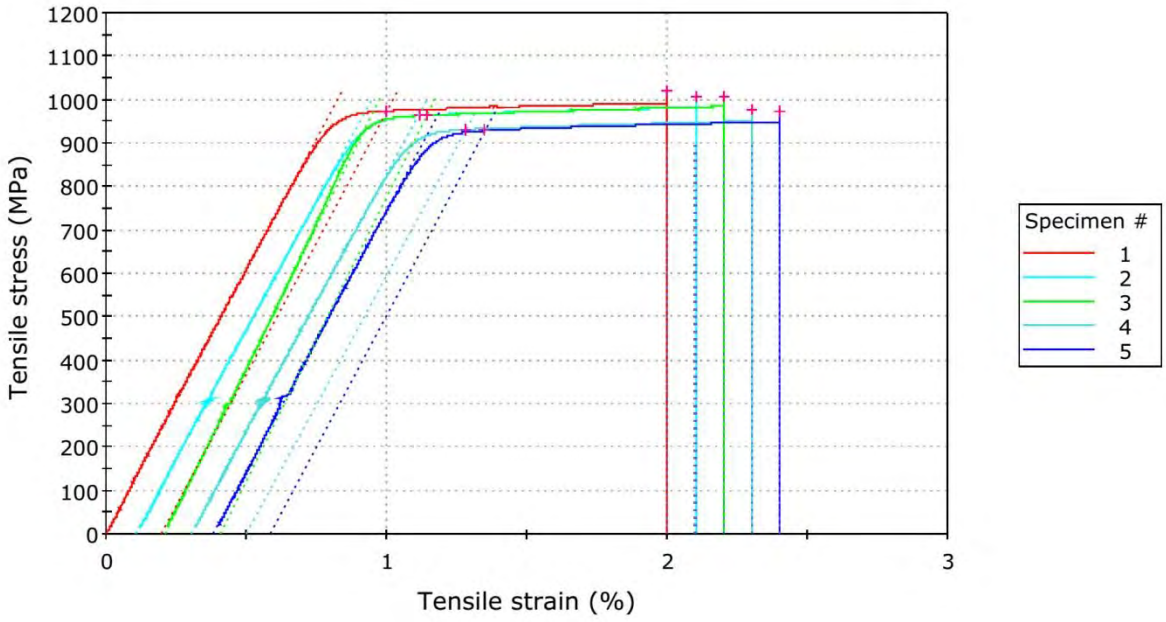

Figure 42: Titanium stress vs. strain curves

3.3.3 FML Tensile Test Results

The FML tensile tests were performed in accordance with ASTM D3039 under displacement control at a rate of 2 millimetres / minute. All specimens were strain gauged. The data was logged to both the HBM and MTS units and the separate data sets were compared to ensure

consistency. The recorded data included the load, strain and test machine stroke. The logged data was used to determine the final failure strengths of the test specimens.

The initial failure modes were also required for correlation with the progressive failure prediction model. To aid in the determination of the initial failure modes of the specimens a stereo microscope was placed next to the test machine. Some of the specimens were removed periodically from the test machine during loading for the purposes of a micrographic failure analysis and then returned to the test machine for further loading. The micrographic analysis concentrated on the edges of the specimens where the matrix failure could be detected. The onset of matrix failure would indicate that initial failure had occurred between the load at which the test had been stopped for the examination and the previous load at which the examination had occurred. This process was only carried out in the elastic range of the specimens. The stress versus strain curves of the various successive load applications for individual specimens were compared to ensure that the elastic limit had not been exceeded.

Acoustic monitoring, through the use of a medical stethoscope, was used to gain additional insight into the initial failure modes of the specimens. This process allowed for the identification of the specific failure modes occurring due to the different types of acoustic emission associated with fibre and matrix failure. The stethoscope was only used for the identification of the initial failure modes and was withdrawn before final failure. All of the specimens were monitored in this fashion.

A number of specimens demonstrated an abrupt and clearly identifiable collapse at the maximum failure mode. These specimens included T0-A, T0-B, T90-B and T90-C. The ensuing stress versus strain curves are shown in Figure 43.

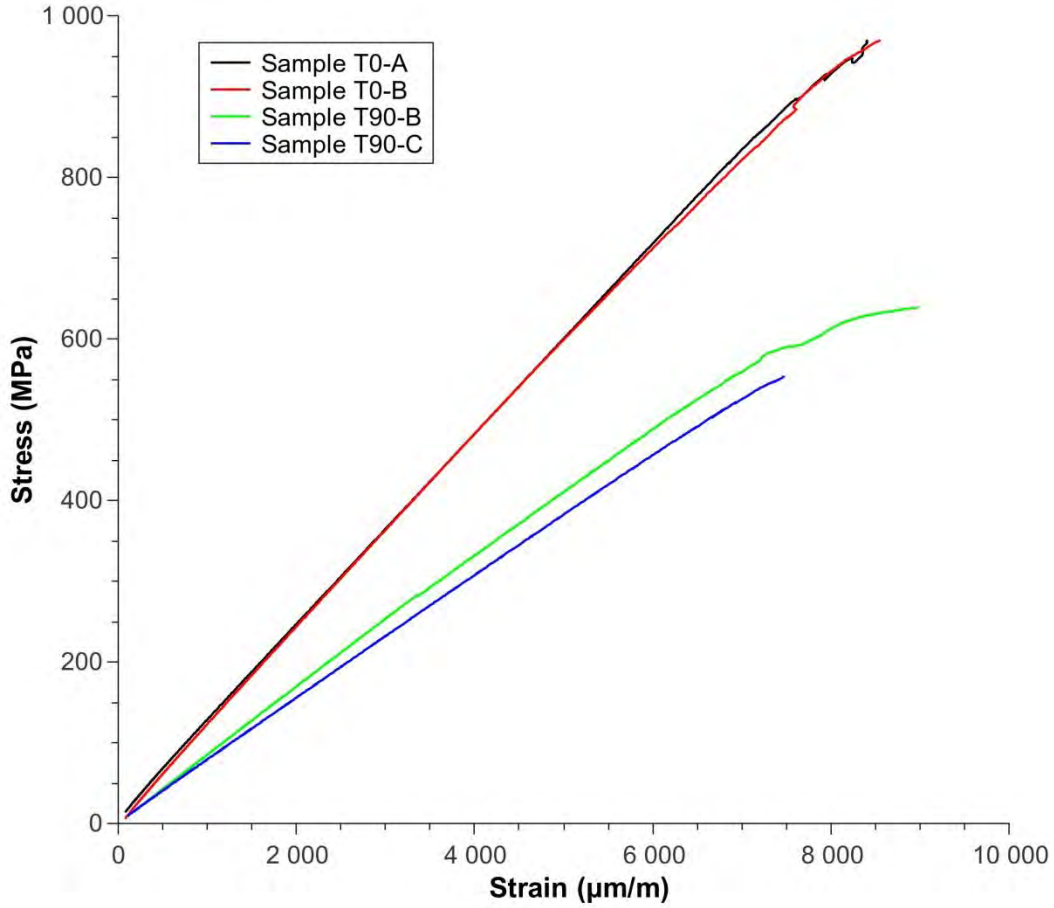

Figure 43: Stress-strain curves for specimens T0-A, T0-B, T90-B and T90-C

Some specimens demonstrated a limited degree of plastic extension in the titanium before final collapse. The failure load of these specimens was determined by the intersection with the 0.2% strain offset line. These specimens included T45-B, T45-C and T-90A, with the stress versus strain curves shown in Figure 44.

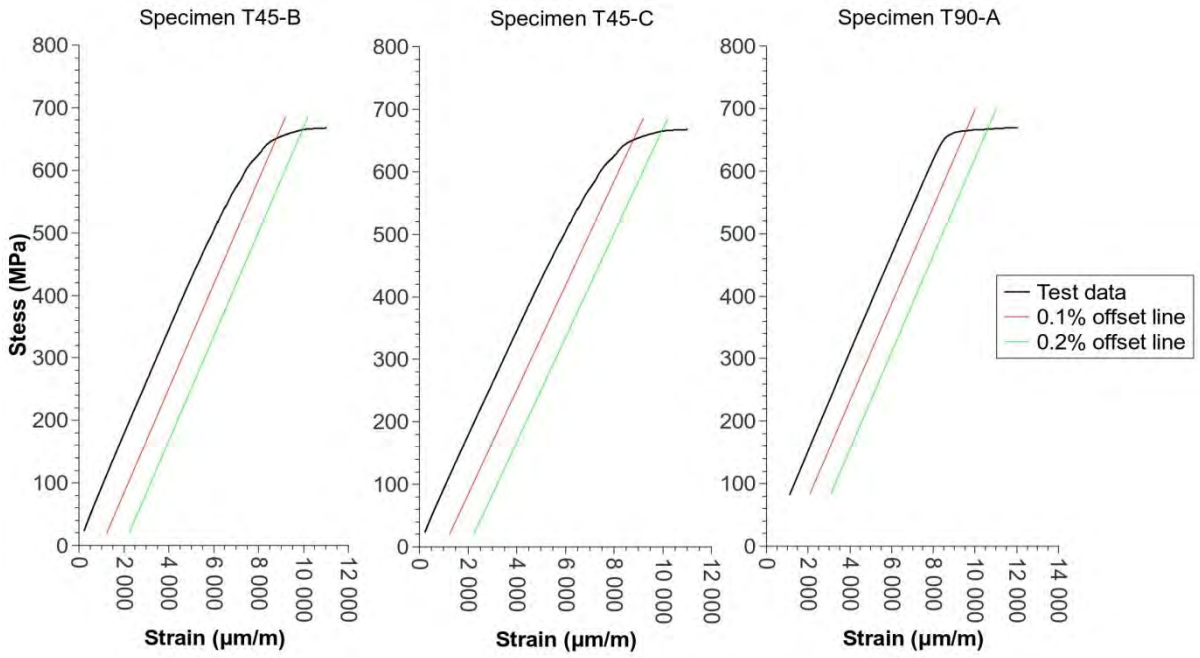

Figure 44: Stress-strain curves for specimens T45-B, T45-C and T90-A

The strain gauges debonded from two of the specimens prior to the final failure load being reached, namely specimens T0-C and T45-A. Specimen T0-C nonetheless showed an abrupt collapse with a clearly identifiable failure stress. The curve of the stress versus the machine extension is given in Figure 45 (a).

Specimen T45-A showed a small degree of plastic extension before collapse, as shown in Figure 45 (a). With no strain gauge data being available at the point of failure, a 0.2% strain offset cannot be identified. An alternative approach was taken to identify the end of the plastic transition zone for the specimen. The slope of the stress-machine extension curve was plotted against the stress, as shown in Figure 45 (b). The plastic transition zone is clearly identifiable, with the transition being complete at a stress of 663 MPa.

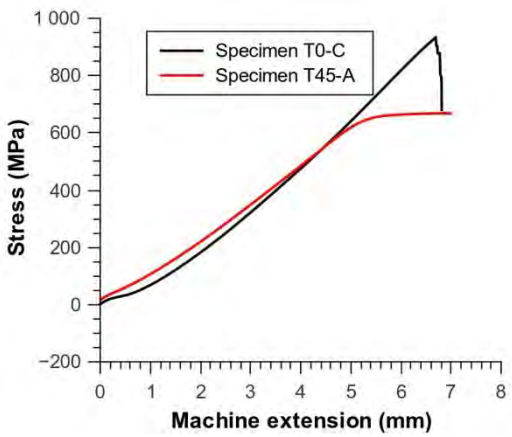

(a) Stress versus machine deflection for specimens T0-C and T45-A

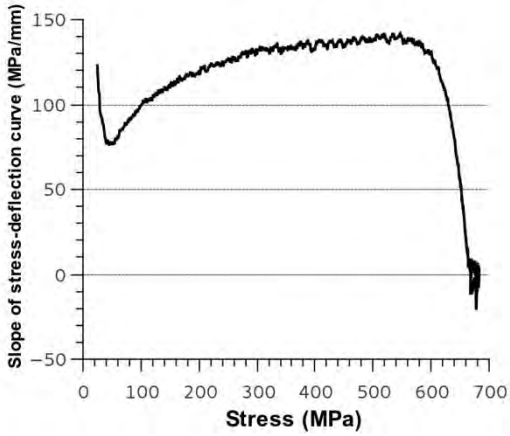

(b) Slope of stress-deflection curve versus stress for specimen T45-A

Figure 45: Mechanical response plots of specimens T0-C and T45-A

A summary of the final failure stresses from the mechanical tests is given in Table 21.

Table 21: Summary of final failure stresses

Specimen Number	Final Failure Stress (MPa)
T0-A	969
T0-B	971
T0-C	933
T45-A	663
T45-B	665
T45-C	667
T90-A	667
T90-B	639
T90-C	553

The monitoring of the specimens with a stethoscope allowed for the identification of the first failure modes, which are summarised in Table 22. The sound characteristics of resin and fibre failure differ considerably, giving insight into the initial failure mode. This was particularly applicable to the specimens where the carbon fibre was in a cross ply orientation.

Two different types of fibre breakage were monitored, namely that of the carbon fibres and also the polyester cross stitching of the fabrics. The polyester fibres had a far lower energy failure mode than the carbon fibres. The polyester fibre breakage was useful for identifying

the failures in the specimens with transverse laminates, where the resin failure occurring between the fibres also resulted in the simultaneous failure of the cross stitching.

Table 22: Summary of initial failure stresses as detected by acoustic emission

Specimen Number	Initial Failure Stress (MPa)	Notes
T0-A	None	No initial failure
T0-B	None	No initial failure
T0-C	None	No initial failure
T45-A	376	Initial failure occurred at 376 MPa in the resin. From 451 MPa onwards fibre breakage was also apparent.
T45-B	375	Initial failure occurred at 375 MPa in the resin. Acoustic events were continuous from this point, including fibre breakage.
T45-C	338	Initial failure occurred at 338 MPa in the resin. Acoustic events were continuous from this point, including fibre breakage.
T90-A	170	Breakage of polyester fibres continuous from 170 MPa.
T90-B	168	Breakage of polyester fibres continuous from 168 MPa.
T90-C	175	Initial breakage of polyester fibres from 175 MPa. The intensity of the breakage increased from 187 MPa.

Some of the specimens were taken up through a series of intermediate load steps leading up to final failure. Upon each step in load the specimen was removed for microscopic examination to determine resin damage. This was done in order to determine the range within which externally visible first failure mode damage occurred. Once the observations were complete the specimen would be returned to the test machine and loaded up to the next target load step and the observations would be repeated. Only the specimens listed in **Table 23** were tested in this fashion; the others were taken directly to failure to confirm that the observation process was not influencing the failure of the specimens.

A stereo microscope was placed next to the test machine to monitor the specimens during the tests. Micrographs were captured using a digital SLR camera attached to the microscope via an adapter. The results of the observations are given in Table 23. The stress at the start of the test range is the maximum stress reached in the previous load step, while the stress at the end of the test range is the stress reached in the load step for which the observation was being made. The two stresses therefore determine the range within which the cracks occurred. The results for all of the specimens tested using this process are presented in the table, including those did not show cracks prior to final failure.

Table 23: Summary of first failure cracks observed during tests

Specimen	Stress at Start of Test Range(MPa)	Stress at End of Test Range(MPa)	Description
T0-A	N/A	N/A	No visible cracks leading up to final failure.
T45-B	N/A	N/A	No visible cracks leading up to final failure.
T45-C	N/A	N/A	No visible cracks leading up to final failure.
T90-B	179.5	257.1	Cracking was observed. The specimen was then taken to failure without any further micrographic observations.
T90-C	155.5	207.3	Initial cracks were observed.
	207.3	262.2	Crack growth observed.
	262.2	308.0	The size and number of the cracks had increased.
	308.0	470.7	The number of cracks had increased. The specimen was then taken to failure without any further micrographic observations.

The micrograph of the initial cracking in specimen T90-B is shown in Figure 46, while that for specimen T90-C is in Figure 47. The micrograph of the more strongly developed cracking in specimen T90-C after the 470 MPa load step is in Figure 48. Due to the limited depth of field offered by the microscope, image stacking was used to extend the depth of focus of the images.

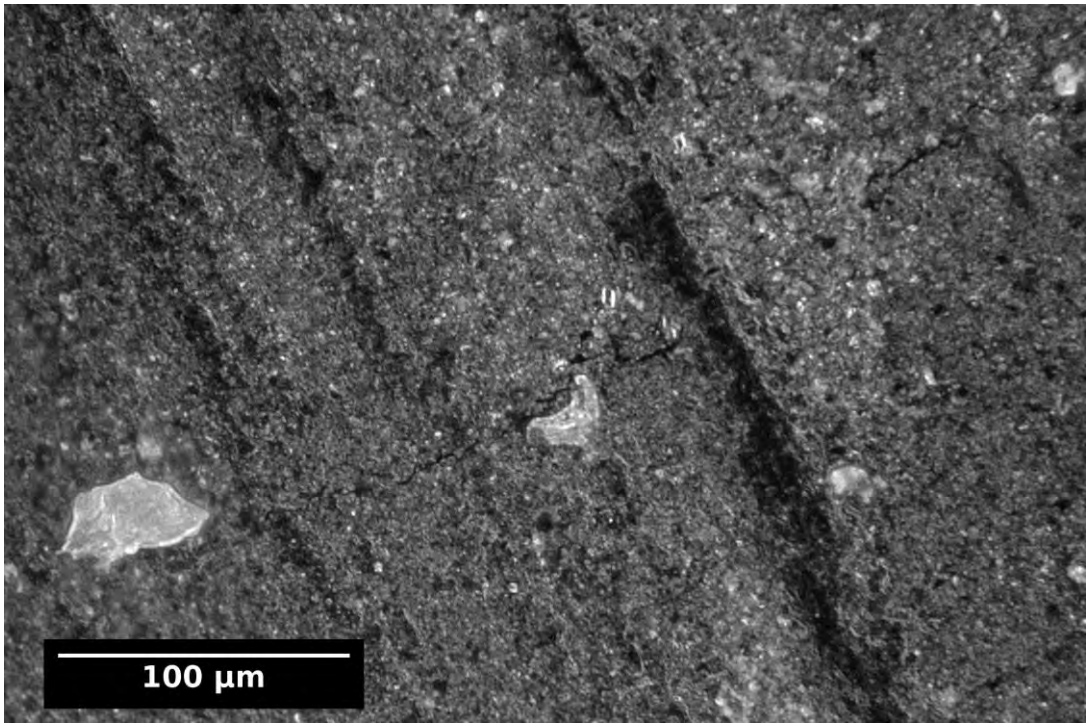

Figure 46: Initial cracking in specimen T90-B

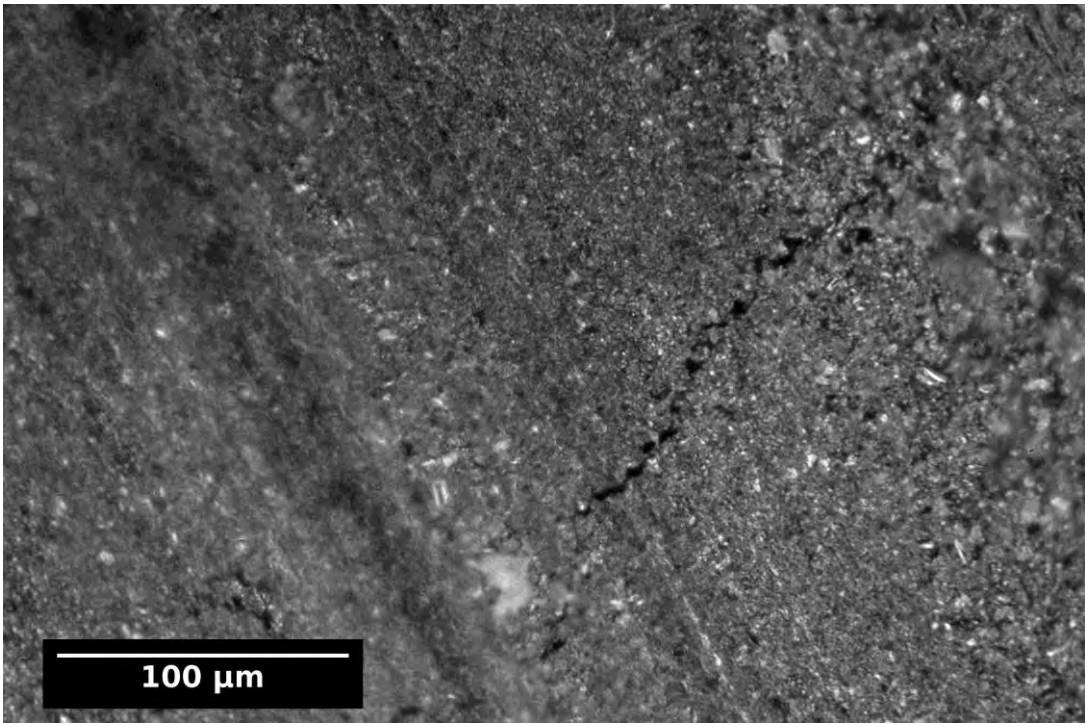

Figure 47: Initial cracking in specimen T90-C

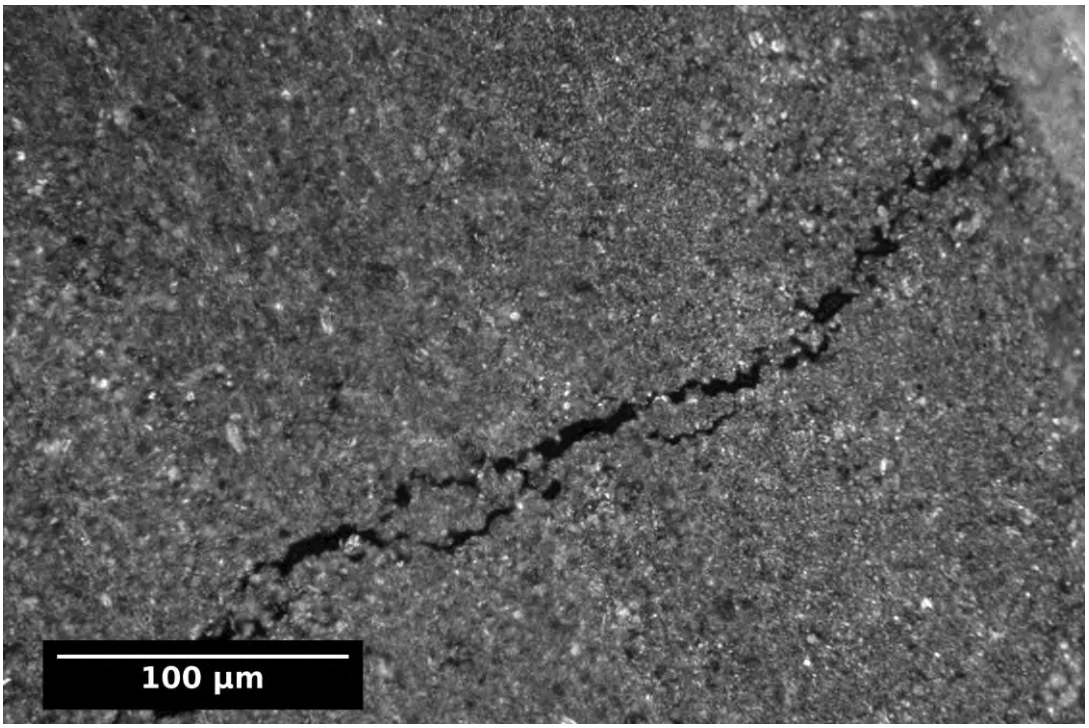

Figure 48: Cracking in specimen T90-C after the 470 MPa load step

The specimens that did not show visible surface cracks during loading did show cracks after failure that were consistent with the expectations for the lamination angles. A failure

associated with specimen T45-B is shown in Figure 49, while that for specimen T0-A is in Figure 50.

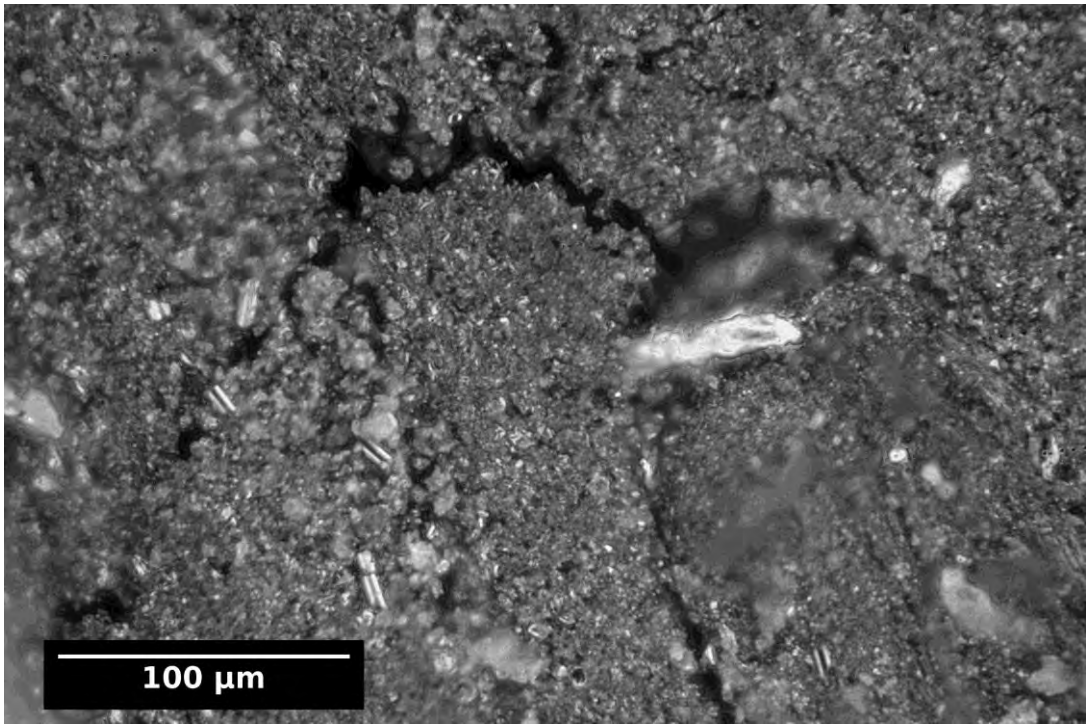

Figure 49: Edge of specimen T45-B after final failure

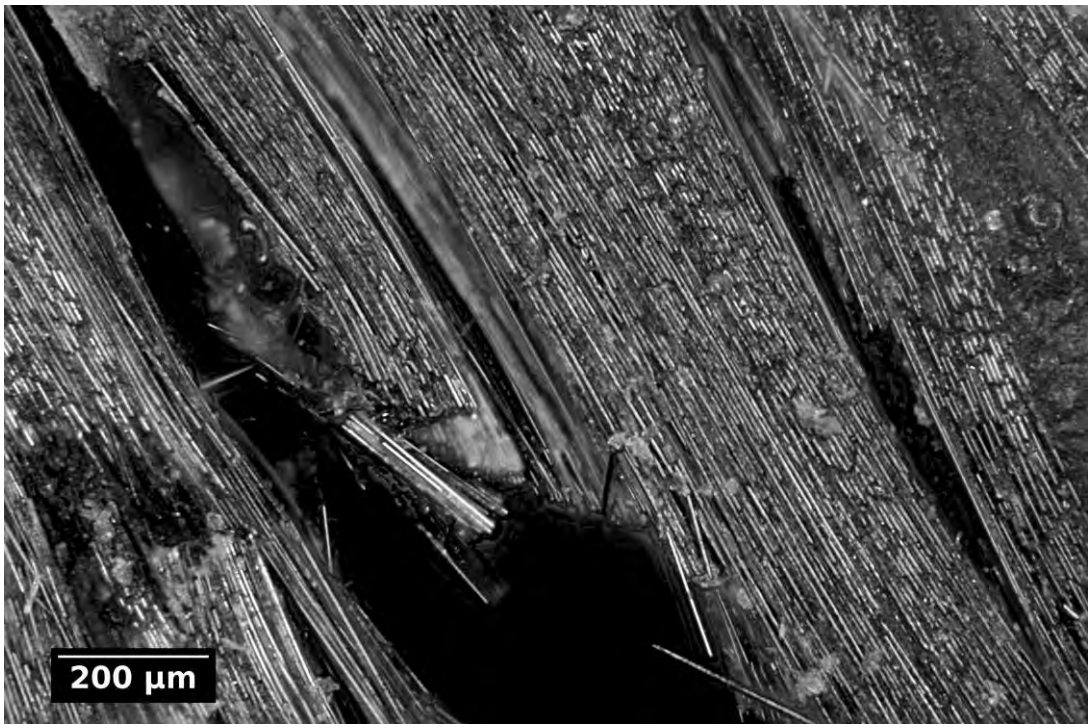

Figure 50: Edge of specimen T0-A after final failure

Several of the specimens were examined after failure using a micro-focus X-Ray system. This was used to assess the internal failure mechanisms without first de-bonding the specimens for examination. The internal failure was compared to the failure shown by the micrographic examination in order to confirm that the cracks observed in the micrographic survey did extend into the specimen, as opposed to being a surface effect. The output for specimen T90-A is shown in Figure 51. The exposure settings were a voltage of 100kV with a current of 215 μA and an exposure time of 40 seconds. The image presented is a negative of the original image in order to enhance the clarity of the matrix cracks.

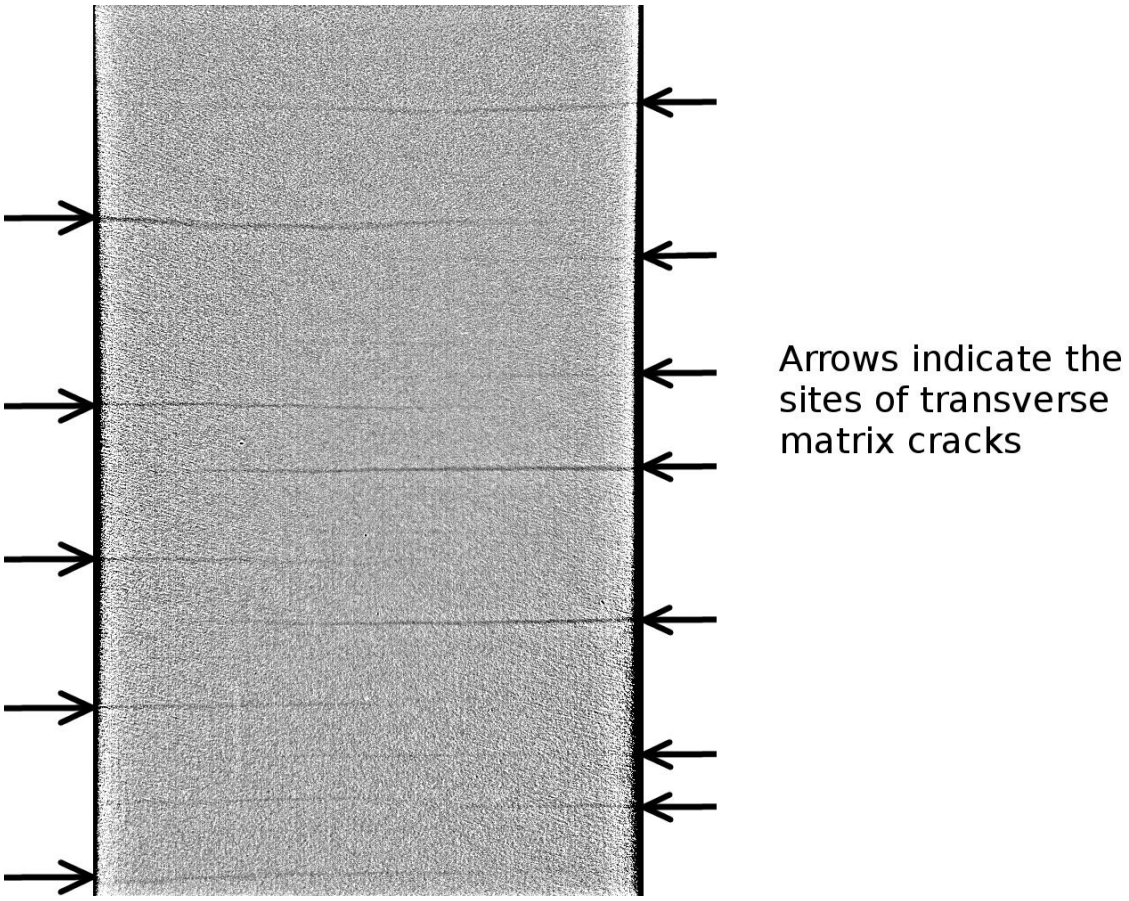

Figure 51: Micro-focus X-Ray image of specimen T90-A post failure, negative image

Specimen T0-B was also assessed, as shown in Figure 52. The settings in this case were a voltage of 85 kV with a current of 150 μA and an exposure time of 125 seconds.

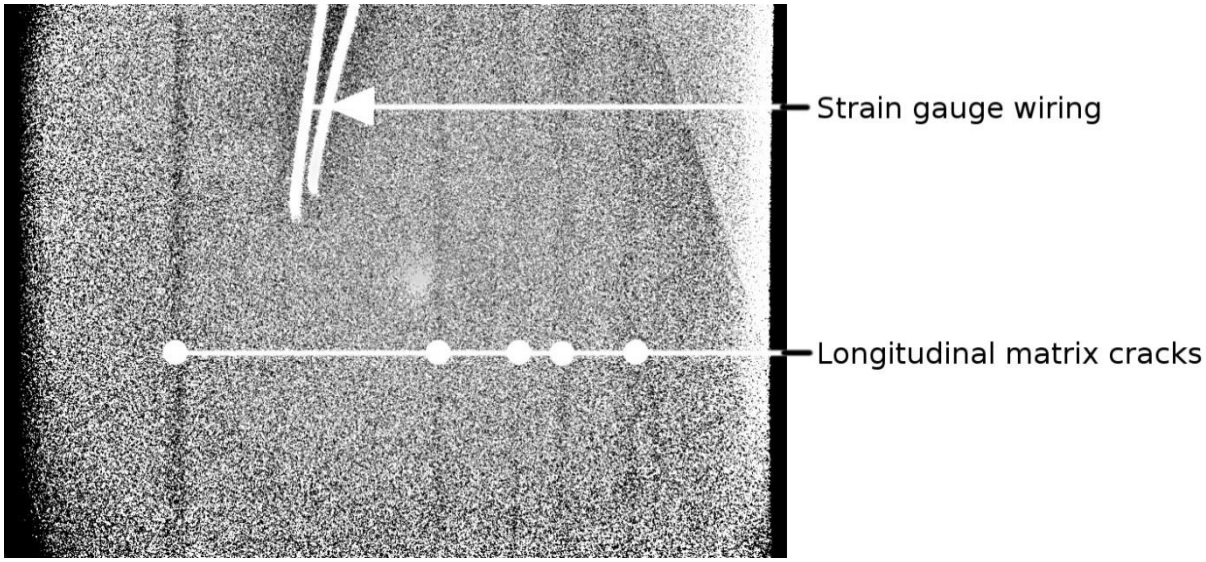

Figure 52: Micro-focus X-Ray image of specimen T0-B post failure, negative image

The micrographic results may be compared with those from acoustic emission in order to determine the validity of the acoustic emission data. The data is summarised in Table 24 and presented graphically in Figure 53.

Table 24: Comparison of acoustic emission and micrographic results for first failure

Specimen	Initial Failure Stress from Acoustic Emission (MPa)	Micrographic: Stress at Start of Test Range(MPa)	Micrographic: Stress at End of Test Range(MPa)
T90-B	168	179.5	257.1
T90-C	175	155.5	207.3

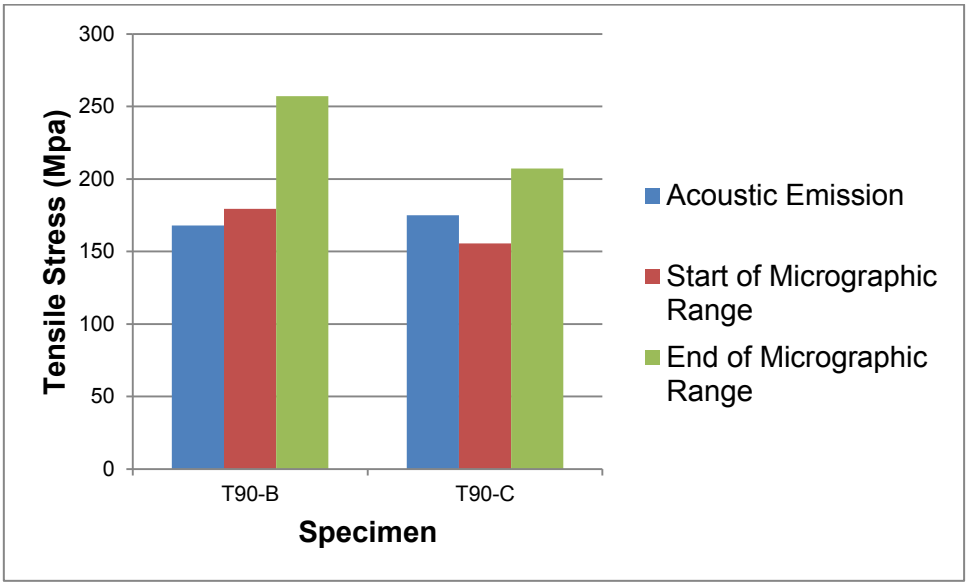

Figure 53: Comparison of acoustic emission and micrographic results

The stress range within which cracking was observed in the micrographs for specimen T90-B starts at a stress that is 6.8% higher than the first recorded acoustic event. The first acoustic event for specimen T90-C was within the stress range where cracking was observed. These observations add confidence to the method of observing the acoustic events as indicators of initial failure.

3.4 Discussion and Conclusions from the Test Results

The initial and final measured failure stresses can be compared to the predicted results. There is some variation in the thicknesses of the tensile specimens due to small variations in the resin content. A proper comparison requires that these variations are taken into account. The predicted stresses are expressed as stress resultants N_x through the multiplication of the stress by the FML thickness used for the prediction. The N_x value is then divided by the thickness of each individual test specimen in order to obtain the predicted failure stress for that specific specimen. This is done for both the initial and final failure stresses. The resulting predicted stresses from the Puck modified criterion are given in Table 25, while those arrived at by the Cuntze criterion are in Table 26.

Table 25: Predicted failure stress per coupon by the Puck modified criterion

Specimen	Thickness (mm)	N_x Initial Failure (N/mm)	N_x Final Failure (N/mm)	σ_x Initial Failure (MPa)	σ_x Final Failure (MPa)
T0-A	3.15	2862	2862	909	909
T0-B	3.21	2862	2862	891	891
T0-C	3.20	2861	2861	894	894
T45-A	3.20	1239	2050	387	641
T45-B	3.20	1239	2050	387	641
T45-C	3.20	1239	2050	387	641
T90-A	3.19	623	1904	195	597
T90-B	3.16	623	1904	197	603
T90-C	3.39	626	1904	185	562

Table 26: Predicted failure stress per coupon by the Cuntze criterion

Specimen	Thickness (mm)	N_x Initial Failure (N/mm)	N_x Final Failure (N/mm)	σ_x Initial Failure (MPa)	σ_x Final Failure (MPa)
T0-A	3.15	2862	2862	909	909
T0-B	3.21	2862	2862	891	891
T0-C	3.20	2861	2861	894	894
T45-A	3.20	1486	2050	464	641
T45-B	3.20	1486	2050	464	641
T45-C	3.20	1489	2050	465	641
T90-A	3.19	623	1904	195	597
T90-B	3.16	623	1904	197	603
T90-C	3.39	626	1904	185	562

The percentage deviation between the predicted and experimental stress values can be calculated by Equation 30.

$$\% \text{ Deviation} = \frac{\text{Experimental - Predicted}}{\text{Predicted}} \times 100 \quad . \qquad \text{Equation 30}$$

The comparison between the measured and predicted initial failure stresses is presented in Figure 54, with the percent deviation between the two data sets shown in Figure 55. Values are not given for the specimens with 0° carbon laminates since these specimens are not subject to initial failure.

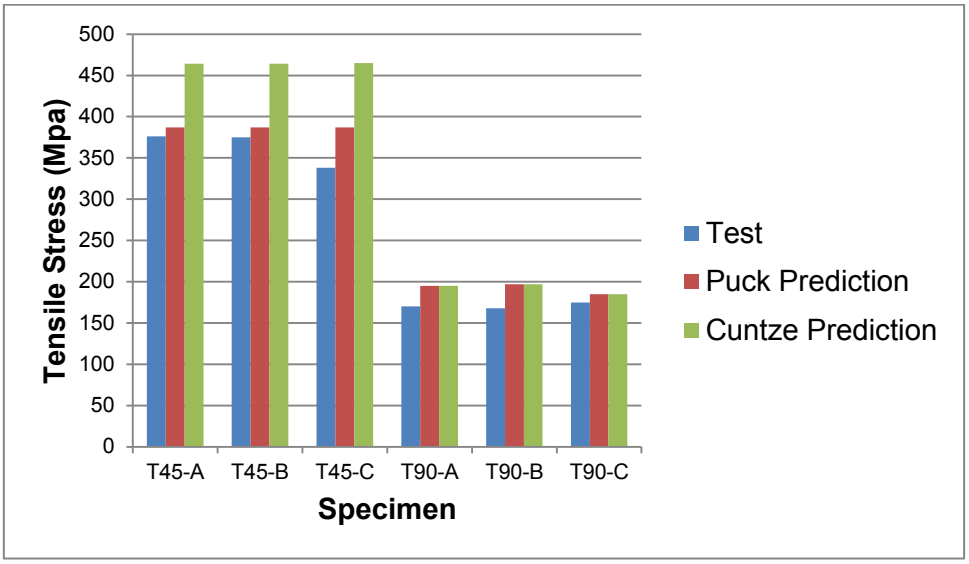

Figure 54: Comparison of measured and predicted initial failure stresses

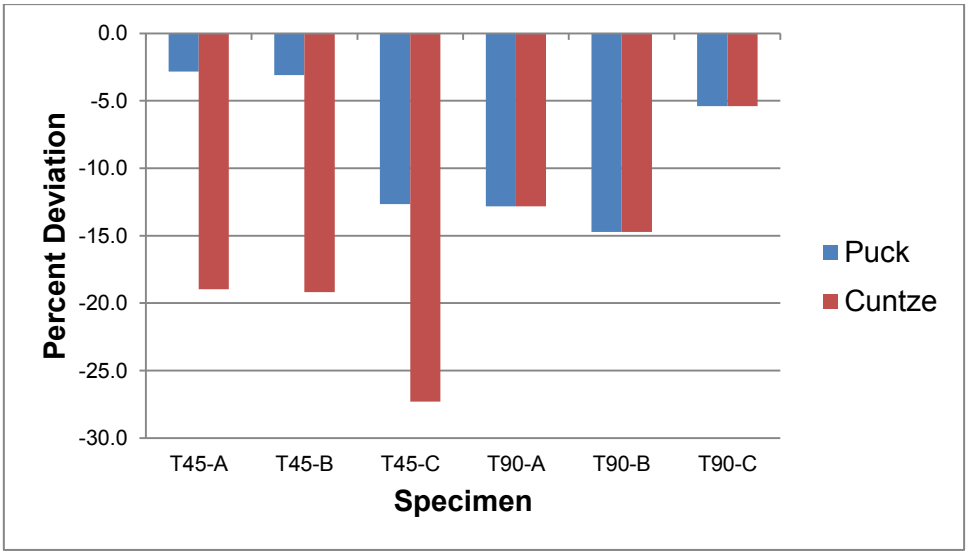

Figure 55: Percent deviation between predicted and measured initial failure stresses

The comparison between the measured and predicted stresses for the final failure modes is shown in Figure 56, with the percentage deviation given in Figure 57. The Puck modified and Cuntze predictions are not given separately due to the two models giving identical final failure stresses.

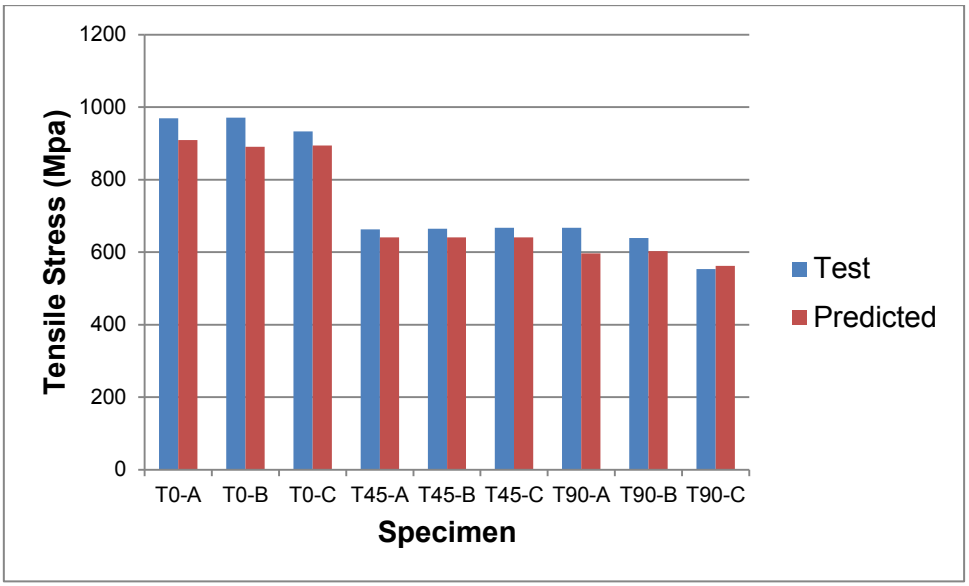

Figure 56: Comparison of measured and predicted final failure stresses

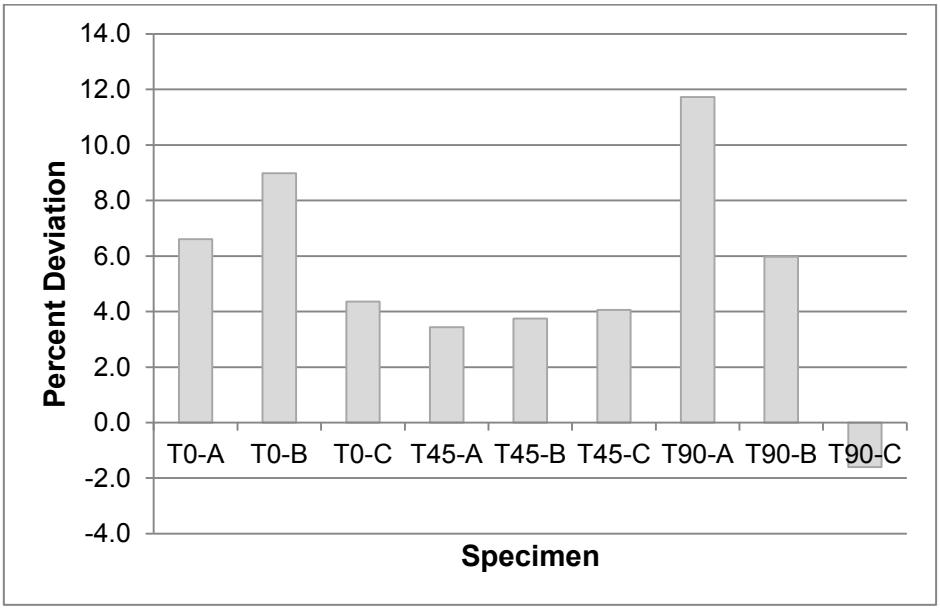

Figure 57: Percent deviation between predicted and measured final failure stresses

For the case where the composite laminae are at 90° to the load direction, the initial stress predictions for both the Puck modified model as well as the Cuntze model give identical results. This is to be expected since both models have an identical formulation for the damage prediction with the laminate in this orientation. The same failure model for the

titanium is applied in each case, resulting in the same predictions from the degradation models. The predictions do differ for the specimens where the composite laminae are at a ±45° angle to the load direction. The Puck modified model gives predictions that are closer to the test results when compared to the Cuntze model. Over the six specimens that are compared, the average deviation of the degradation model that incorporates the Puck modified criterion is -8.6%, while the Cuntze model average deviation is -16.4%. In all cases the predictions are higher than the test results.

The predictions for the final failure modes are identical for the degradation models incorporating both the Puck modified and the Cuntze criteria. The predictions for eight of the specimens were lower than the measured test load at failure, while one prediction was higher than the test load. The average percentage error over all nine specimens was 5.3%.

Both the Puck modified and Cuntze criteria are viable for incorporation into degradation models to be used for design purposes, with the error between the predictions and the test loads being reasonably small. The Puck modified criterion has the advantage of more accurate predictions where the laminate direction is at an angle of ±45° to the load direction. The Cuntze criterion has the advantage of providing more insight into the damage mechanisms that occur during failure due to the larger number of failure modes that are incorporated. A design procedure should ideally use degradation models that incorporate both of these criteria in order to obtain a proper level of insight into the failure modes.

Chapter 4. Ballistic Theory and Testing of Fibre Metal Laminates

4.1 Introduction to Ballistic Theory and Testing

The theory for a method to design Fibre Metal Laminate (FML) based ballistic panels is proposed, together with a candidate design. A common concept that dominates both the theory and design of the panels is that of the ballistic limit. This limit refers to the maximum velocity of a pre-defined penetrator at which it will fail to penetrate the armour.

The threat that the armour must defeat is defined, together with the need to address this threat. A method for predicting the ballistic limit of an FML panel within the velocity range of the threat is then proposed. The prediction of the ballistic limit of Weldox steel plate is also covered as part of the test data analysis. A method is then proposed for the analysis of the test data to determine the ballistic limit of the FML based armour. The mass of a titanium and carbon fibre based FML is given which is anticipated to be sufficient stop the threat.

The objective of this work is to establish a research baseline that is sufficient for the future development of FML armour panels. This baseline will include the numerical modelling, manufacturing, materials selection, ballistic testing and data analysis methods. The work presented here will thereby allow for the expansion of future research to include a variety of FML materials and different means of integration of the armour with vehicles.

4.2 Threat Definition and Need

An emerging threat against armoured vehicles is that of Explosively Formed Penetrators (EFPs). These are mines, often improvised, which are located on the side of the road and which use an explosive to form a metal plate into a penetrator which travels at approximately two kilometres per second. These weapons are capable of penetrating the hulls of infantry fighting vehicles and armoured personnel carriers.

The solution is to add an additional armoured package to the outside of the vehicle hull to provide further protection. Conventional steel armour would impose a weight penalty which would reduce the vehicle mobility. An armour system is therefore required which will allow the vehicle to maintain an acceptable weight.

In order to fully understand the nature of the armour, both the functionality of the EFPs and the armour itself need to be described.

An EFP is a type of self-forging warhead intended to penetrate armour at stand-off distances. An explosive charge is used to deform a metal plate into a penetrator while propelling it towards the target. An overview of the device is shown in Figure 58.

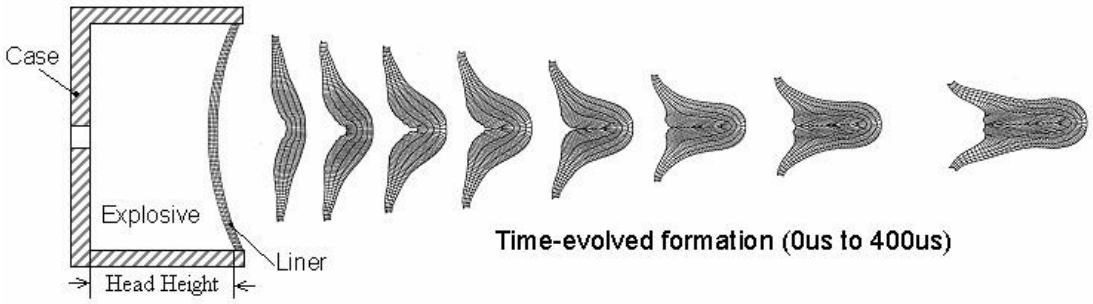

Figure 58: An explosively formed penetrator and the time evolution of the liner [109]

The device is typically made by filling a pipe with explosives. A curved copper or steel disk is fixed to the end of the pipe. The force of the explosion moulds this metal disc into a penetrator while propelling it towards the target. This weapon can typically penetrate a thickness of armour steel equal to half the diameter of the initial disk.

EFPs have been deployed in Iraq as improvised explosive devices against the United States Armed Forces. Five percent of all explosive devices used against US troops in Iraq have been EFPs, but these accounted for one third of all fatalities [110]. There is a risk that the use of these devices might expand to other areas of conflict.

The CSIR tested an EFP against the hull of a Casspir armoured personnel carrier. This device penetrated completely through the vehicle, as can be seen in Figure 59 (a). The effect with the addition of an external armour package is shown in Figure 59 (b), where there is no penetration. Note that the composition of the armour package shown in this figure is not the same as the one described in this work. It is rather one intended purely for demonstration purposes and is too heavy for practical deployment.

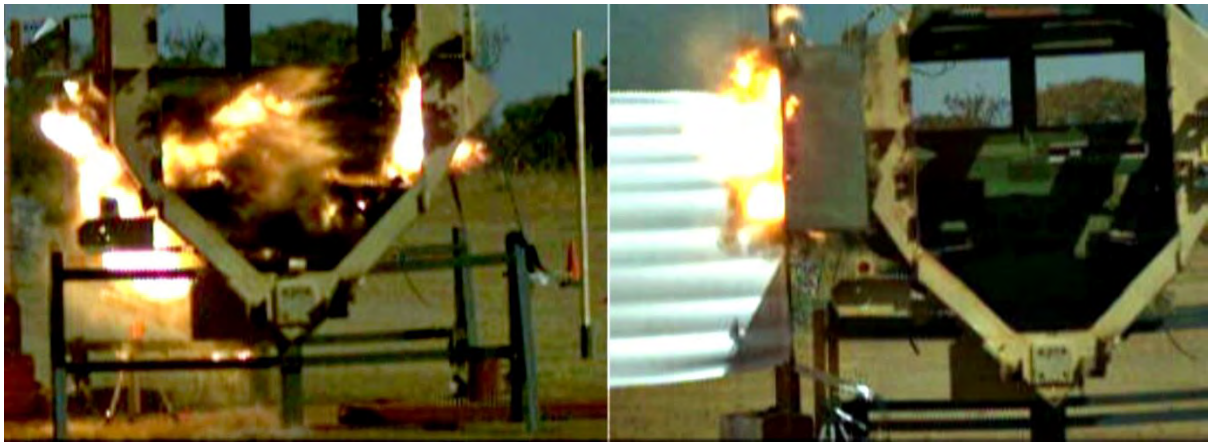

(a) Without armour package (b) With armour package

Figure 59: Effect of an EFP on an armoured personnel carrier

4.3 Prediction of the Ballistic Limit of FMLs

The research into structural behaviour prediction under high and hyper velocity impacts has been driven in part by the requirements of spacecraft design. The investigation gathered impetus during the Apollo programme and has been ongoing since then [111]. The research has focused on the use of gas guns to characterise a range of materials at different impact velocities up to 7.5 km/s, and inhibited shaped charge launchers and hypervelocity launchers for speeds up to 11.5 km/s [112].

The initial work for predicating the effects of hyper velocity impact was done on single wall configurations. The predictive equations for the effect of the impact on different targets needed to account for a variety of factors including crater formation, spallation and penetration [111], [113]. These equations should apply to a variety of materials of differing thicknesses. An examination of the experimental results has led the researchers to develop empirical equations that fit a wide range of conditions accurately while critically offering ease of computation. This latter requirement led to a minimisation in the material properties required for calculation, eventually resulting in the use of density, hardness and Young's Modulus. The effectiveness of this approach has led to these models being propagated through to current research [111]. The use of hardness instead of strength as an input property to the calculations is not ideal for the analysis of FMLs for this work, where the failure strength can be determined but an equivalent hardness of the overall material has no physical basis.

The impact of a projectile on single wall plate is described by the Cour-Palais equation [113]. The impact results in a hemispherical crater in a sufficiently thick plate. As the plate

thickness is reduced there is internal damage to plate which results in incipient spallation. Further reduction in the thickness will result in detached spallation and finally perforation at the limit.

The penetration depth into a monolithic aluminium target can be calculated as per Equation 31 [111], [113], [114].

$$P_{\infty} = 5.24 d_p^{19/18} HB^{-1/4} \left(\frac{\rho_p}{\rho_s}\right)^{\alpha} \left(\frac{V\cos\theta}{C}\right)^{2/3} , \qquad \text{Equation 31}$$

where:

P_{∞}	=	Penetration depth on an infinite plate (cm),
d_p	=	Projectile diameter (cm),
HB	=	Brinell hardness (HB),
ρ_p	=	Density of the projectile (g/cm^3),
ρ_s	=	Density of the shield (g/cm^3),
V	=	Projectile velocity (km/s),
θ	=	Impact angle (radians),
C	=	Speed of sound in the shield (km/s).

The value of the α term Equation 31 varies depending on the reference. Ryan and Christiansen [113], [114] base their values on previous work done by Christiansen which is represented in Equation 32.

$$\alpha = \begin{cases} 0.5 \text{ if } (\rho_p/\rho_s) < 1.5 \\ 2/3 \text{ if } (\rho_p/\rho_s) \geq 1.5 \end{cases} . \qquad \text{Equation 32}$$

Other references by Cour-Palais [111], Hayashida [115] and Schafer [116] set the value of α=0.5 regardless of the density ratio. The majority of the researchers support the single value of 0.5, and therefore this value will be used.

The required level of shielding can be expressed in terms of the penetration depth and the required level of spallation [113]:

$$t_s \geq 3.0 P_{\infty} \text{ to prevent incipient spallation} , \qquad \text{Equation 33}$$

$$t_s \geq 2.2 P_{\infty} \text{ to prevent detached spallation} , \qquad \text{Equation 34}$$

$$t_s \geq 1.8 P_{\infty} \text{ to prevent perforation} , \qquad \text{Equation 35}$$

where t_s is the thickness of the shield (cm).

The ballistic limit of the shield can thereby be defined in terms of the critical diameter of the projectile d_c (cm) as in Equation 36 [113], [114].

$$d_c = \left[\frac{t_s}{k} \frac{HB^{1/4} \left(\frac{\rho_s}{\rho_p} \right)^{\alpha}}{5.24 \left(\frac{V \cos\theta}{C} \right)^{2/3}} \right]^{18/19} , \qquad \text{Equation 36}$$

where the thickness scaling factor k is 3.0, 2.2 or 1.8 as per Equation 33 through Equation 35. The penetration into a monolithic titanium target can be expressed by a modified form of the Cour-Palais relationship, as determined by tests for the James Webb Space Telescope [113], [114].

$$P_{\infty} = 5.24 d_p HB^{-1/4} \left(\frac{\rho_p}{\rho_s} \right)^{1/2} \left(\frac{V \cos\theta}{C} \right)^{2/3} . \qquad \text{Equation 37}$$

The thickness scaling factor k is 3.0 for incipient spall, 2.4 for detached spall and 1.8 for perforation. The critical projectile diameter for a titanium single wall is then predicted as follows:

$$d_c = \left[\frac{t_s}{k} \frac{HB^{1/4} \left(\frac{\rho_s}{\rho_p} \right)^{1/2}}{5.24 \left(\frac{V \cos\theta}{C} \right)^{2/3}} \right]^{18/19} . \qquad \text{Equation 38}$$

An alternative expression for predicting the penetration into a single wall monolithic target is the Schmidt-Holsapple equation [115]. This equation has been verified by test for a wide range of projectiles and target materials in the velocity range of 4 to 8 km/s. Verification tests were also performed using Pyrex projectiles fired into water in the velocity range of 1.5 to 6 km/s. The ballistic limit form of the equation is presented in Equation 39, where a 0.7 factor is used for the spallation limit to prevent penetration from spalling.

$$d = 2.06 t \left(\frac{\rho_p}{\rho_t} \right)^{-0.159} \left(\frac{2.68 F_{tu}}{\rho_p V_n^2} \right)^{0.236} , \qquad \text{Equation 39}$$

where:

d = Projectile critical diameter (in),
t = Target thickness (in),
ρ_p = Density of the projectile (lb/in^3),

ρ_t = Density of the target (lb/in^3),
F_{tu} = Ultimate tensile strength of the target (lb/in^2),
V_n = Impact velocity normal to the target (ft/s).

Further manipulation of the Schmidt-Holsapple equation by Frost and Rodriguez [117] resulted in an expression where the thickness of a composite material target can be expressed as an equivalent thickness of aluminium. This aluminium thickness can then be used in a suitable equation for predicting the penetration, as was verified by Frost and Rodriguez through testing. This expression may also be applied to other metals due to it depending only on the density and strength of the metal.

$$t_{al} = t_{matl}\left(\frac{\rho_{al}}{\rho_{matl}}\right)^{-0.159}\left(\frac{F_{tu\,al}}{F_{tu\,matl}}\right)^{0.236}, \qquad \text{Equation 40}$$

where:

t_{al} = Equivalent thickness of an aluminium target,
t_{matl} = Thickness of original target,
ρ_{al} = Density of aluminium,
ρ_{matl} = Density of the original target material,
$F_{tu\,al}$ = Ultimate tensile strength of the aluminium,
$F_{tu\,matl}$ = Ultimate tensile strength of the original target material.

The research into single wall shields was eventually extended to develop predictive equations for double walled configurations, known as Whipple shields. The double walls were initially treated as single walls with an applied correction factor. This correction factor was based on the overall geometry of the shield. There are additional factors that apply to the double wall shields, primarily driven by the effect of the debris cloud from the first wall that then impinges on the second wall. The requirement for correlation with test data resulted in the hardness term being dropped from the equations and the yield strength of the material was used instead [111]. The understanding of Whipple shields has progressed, which has resulted in scaled single wall equations still being used for velocities of between 0.5 and 3 km/s. For velocities between 7 and 16 km/s more theoretical kinetic energy based relationships used. The intermediate range is predicted by interpolation between the higher and lower velocity ranges, with the predictions being substantiated by test results [118]. Since the Whipple model uses the material strength rather than hardness as an input parameter it is of interest in this work.

A Whipple shield consists of two main parts, as shown in Figure 60 [113]. The projectile first strikes the bumper plate, which is relatively thin and is sacrificial. The remaining debris cloud is then stopped by the rear wall.

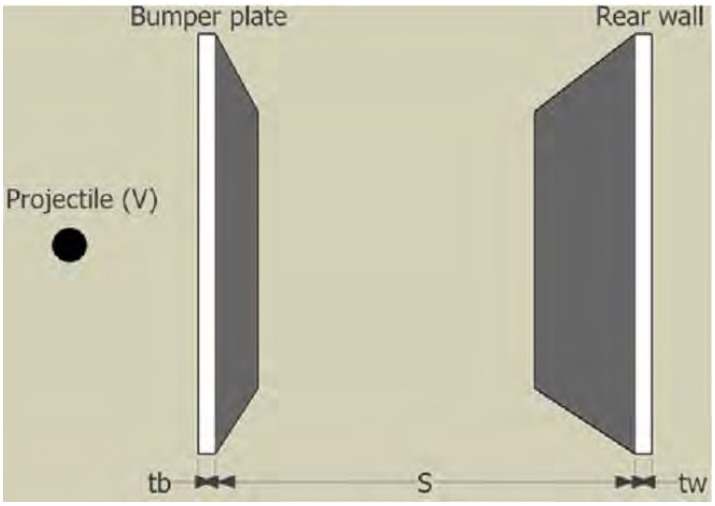

Figure 60: Whipple shield configuration [113]

Low velocity impacts on a Whipple shield are characterised by the perforation of the bumper plate without the projectile fragmenting. This characteristic results in a predominantly intact projectile striking the rear wall of the shield. The low velocity regime is typically less than 3 km/s, but can be determined more precisely by Equation 41 [113], [114].

$$V_{LV} = \begin{cases} 1.436\left(\frac{t_b}{d_p}\right)^{-1/3}, & \text{for } t_b/d_p < 0.16 \\ 2.6, & \text{for } t_b/d_p \geq 0.16 \end{cases} \qquad \text{Equation 41}$$

where:

V_{LV} = Upper bounding velocity of the low-velocity regime (km/s),
t_b = Thickness of the bumper plate (cm).

The critical diameter of the projectile can now be defined for this velocity regime [113], [114], [119].

$$d_c = \left[\frac{t_w\left(\frac{\sigma_y}{40}\right)^{1/2} + t_b}{0.6(\cos\theta)^{5/3}\rho_p^{1/2}V^{2/3}}\right]^{18/19}, \qquad \text{Equation 42}$$

where:

σ_y = Rear wall yield stress (ksi),
t_w = Thickness of the rear wall (cm).

At impact velocities above 7 km/s the magnitude of the shock amplitude is sufficient to cause the projectile to shatter. The critical projectile diameter in this hypervelocity regime can be defined as follows [113], [114], [119]:

$$d_c = 3.918 F_2^* \frac{t_w^{2/3} S^{1/3} \left(\frac{\sigma_y}{70}\right)^{1/3}}{\rho_p^{1/3} \rho_b^{1/9} (V\cos\theta)^{2/3}} \quad , \qquad \text{Equation 43}$$

where:

S = Spacing (cm),
ρ_b = Density of the bumper plate (g/cm^3).

The F_2^* term is used to correct for configurations where the bumper is too thin, and is defined in Equation 44.

$$F_2^* = r_{S/D} - 2\frac{(t_b/d_p)}{(t_b/d_p)_{crit}}(r_{S/D} - 1) + \left(\frac{(t_b/d_p)}{(t_b/d_p)_{crit}}\right)^2 (r_{S/D} - 1) \quad , \qquad \text{Equation 44}$$

where:

$$(t_b/d_p)_{crit} = \begin{cases} 0.2, & \text{for } S/d_p \geq 30 \quad , \\ 0.25, & \text{for } S/d_p < 30 \quad , \end{cases} \qquad \text{Equation 45}$$

and

$$r_{S/D} = \frac{t_w(t_b = 0)}{t_w\left(\frac{t_b}{d_p} = \left(\frac{t_b}{d_p}\right)_{crit}\right)} \quad . \qquad \text{Equation 46}$$

The intermediate regime between the two velocity ranges represented by Equation 42 and Equation 43 is predicted by linear interpolation between these two equations. A graphical representation of these three velocity regimes can be seen in Figure 61, together with a comparison to an equal mass monolithic target.

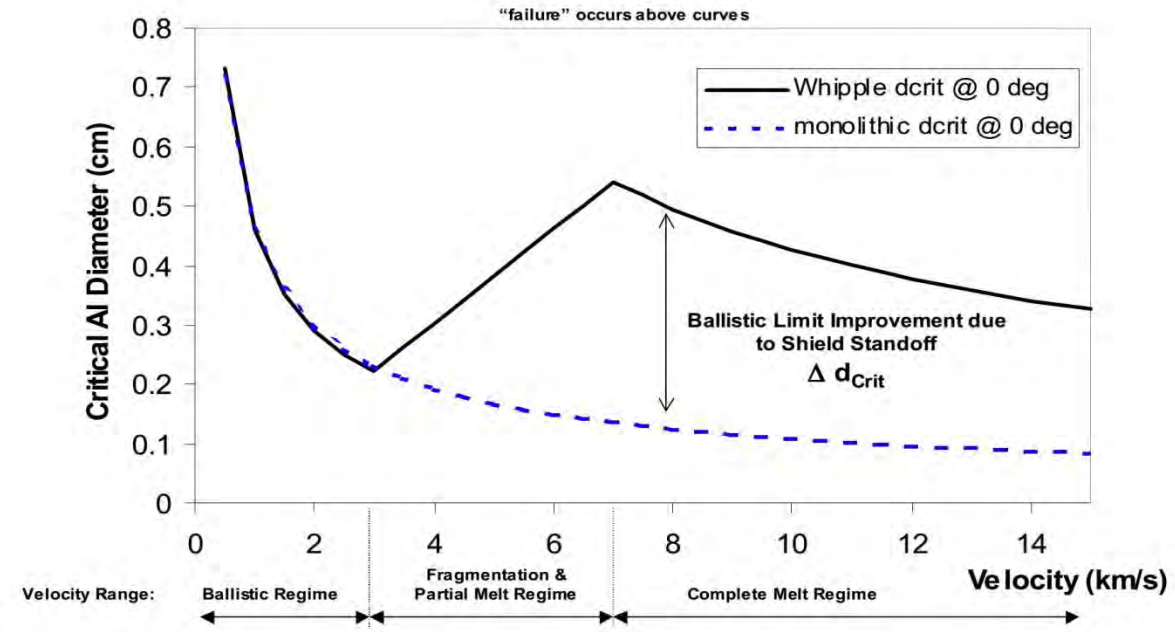

Figure 61: Ballistic limit curve for monolithic and Whipple shield targets [120]

The intent of presenting the double wall Whipple shield equations was for comparison with the single wall equations in order to determine if a strength-based prediction method is feasible for the single wall configuration. A modified form of the Whipple model in Equation 42 is proposed for this work, where the bumper plate thickness is reduced to zero in order to arrive at a single wall relationship,

$$d_c = \left[\frac{t_w \left(\frac{\sigma_y}{40}\right)^{1/2}}{0.6(\cos\theta)^{5/3} \rho_p^{1/2} V^{2/3}} \right]^{18/19} . \qquad \text{Equation 47}$$

A comparison of the single wall and modified Whipple equations is carried out for different aluminium and titanium alloys, specifically Al 2024, Al 6061 and Ti 6Al-4V. Equation 36 predicts the behaviour of the aluminium alloys in a monolithic configuration, while Equation 38 predicts the behaviour of the titanium. Equation 47 is applied to the same monolithic panels for comparison. A shield wall thickness of 3.6 cm and an impact angle of zero degrees are used in all cases. The requirement is resistance to perforation, resulting in the selection of k=1.8.

The comparison of the equations for the material types is shown in Figure 62 through Figure 64. The maximum difference between the two equations in the velocity range of 0.5 to 2.5 km/s for Aluminium 2024 is 3.98%, for aluminium 6061 it is 3.32% and for titanium 6Al-4V it

is 2.26%. These results instil confidence in the application of Equation 47 to monolithic shields in this velocity range.

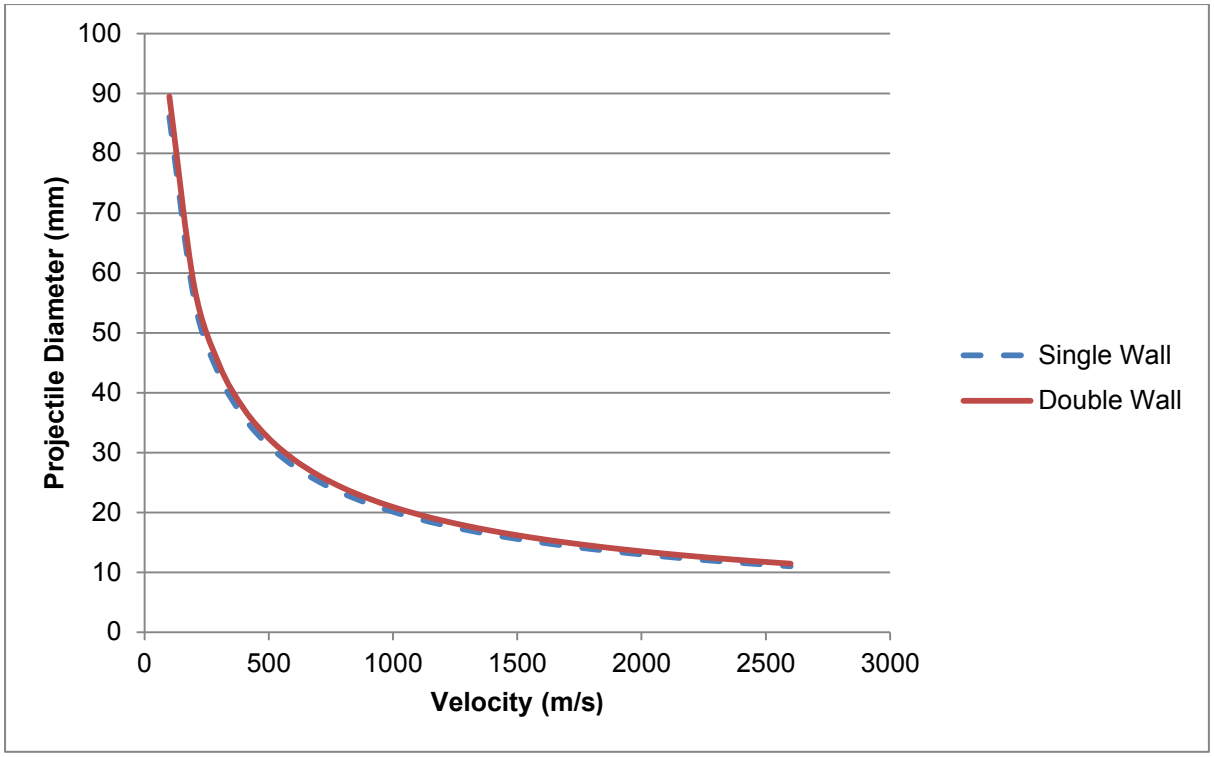

Figure 62: Single-wall and modified Whipple shield equations for aluminium 2024

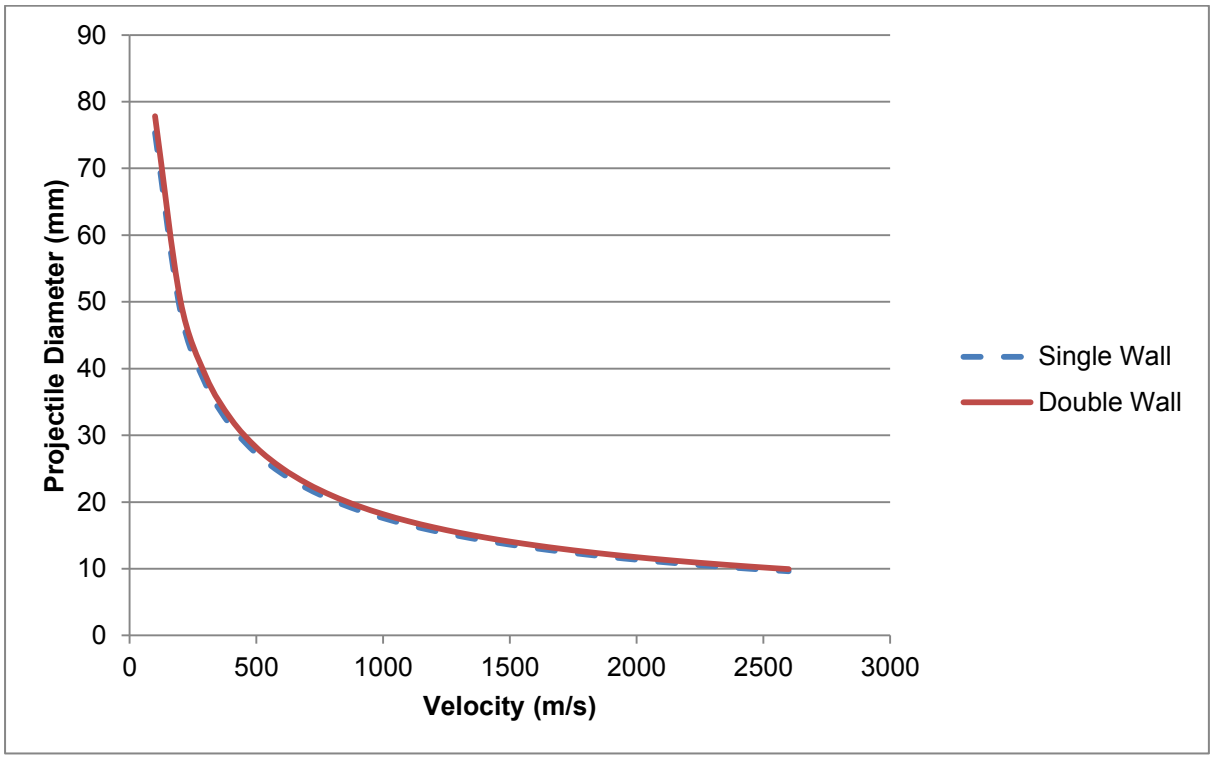

Figure 63: Single-wall and modified Whipple shield equations for aluminium 6061

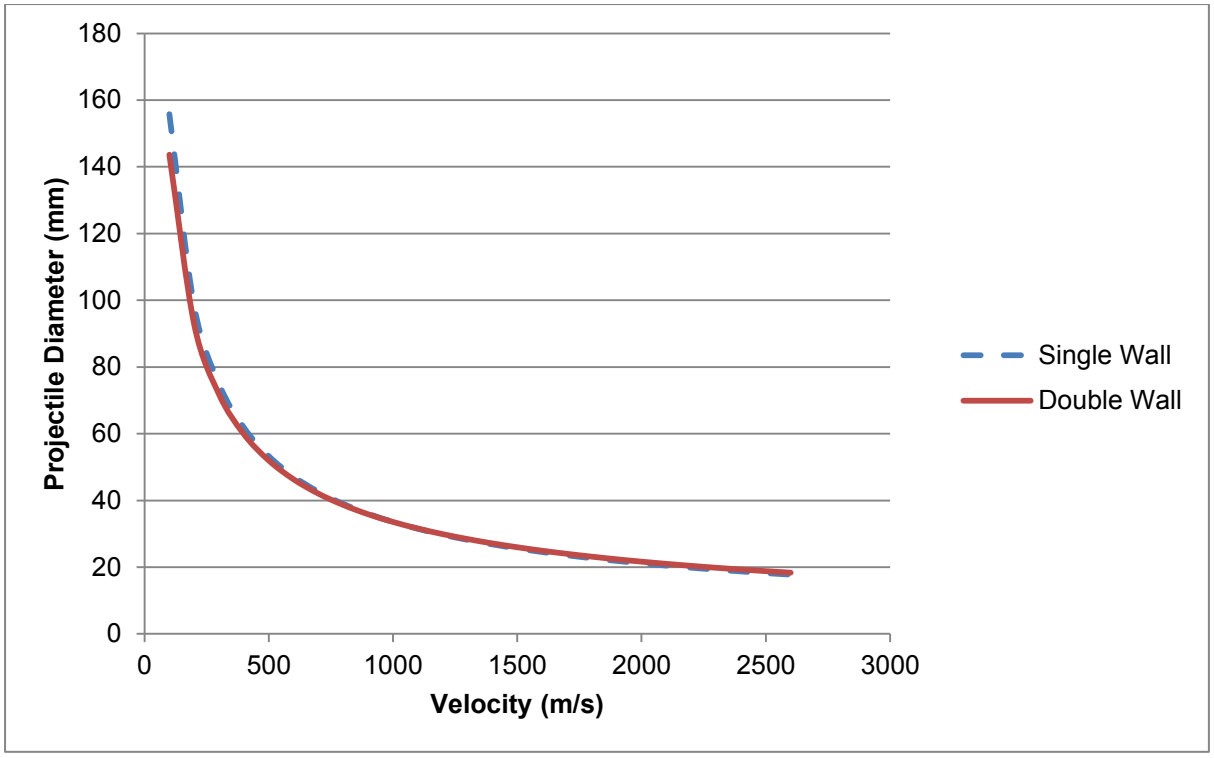

Figure 64: Single-wall and modified Whipple shield equations for titanium 6Al-4V

This study presented here resulted in two proposed methods which use material strength based criteria to determine the critical diameter of a penetrator at the ballistic limit.

4.4 The Ballistic Limit of Weldox Plate

Børvik [121] performed an experimental and numerical investigation of the penetration of Weldox plate by projectiles. Several different numerical models are considered, and the implementation of the Wen-Jones model by Børvik is of specific interest for the determination of the ballistic limit for Weldox plate.

The model assumes a clamped circular plate of radius R and thickness H. The projectile is represented by a blunt cylinder with a diameter of d=2a [121]. Assuming a rigid and perfectly plastic plate, the transverse velocity field of the plate can be expressed as

$$W = W_0 \text{ for } r \leq a \text{ and } W = W_0 \left[\frac{\ln(r/R)}{\ln(a/R)}\right] \text{ for } a \leq r \leq R \quad , \qquad \text{Equation 48}$$

where the transverse displacement of the plate W is at a radius r and W_0 is around the periphery of the interface between the punch and the plate. Applying the principle of virtual

work to the displacement field and the local indentation Δ, a load-displacement relationship can be determined in terms of the total punch displacement W_t, where

$$W_t = W_0 + \Delta = \frac{F - F_c}{K_m} + \left(\frac{F}{F_u}\right)^{1/n} \Delta_c \quad , \qquad \text{Equation 49}$$

where: F_c = Static collapse load of the plate for infinitesimal displacement,
$= \left(4/\sqrt{3}\right)\pi M_0\left[1+\left(1+\sqrt{3}/2\right)/\ln(R/a)\right]$,
K_m = Plate membrane stiffness $= 2\pi N_0/\ln(R/a)$,
N_0 = Fully plastic membrane force per unit length $=\sigma_y H$,
where σ_y is the tensile yield stress,
M_0 = Fully plastic bending moment per unit length $= \sigma_y H^2/4$,
F_u = Shear force at plugging failure $=\tau_u A_s$,
τ_u = Critical shear stress $=\sigma_u[0.41(H/d)+0.42]$,
n = Work-hardening index defined by $\tau = \tau_u(\gamma/\gamma_u)^n$.

The punch indentation as a function of the shear strain γ is assumed to be

$$\Delta = e\gamma = \frac{1+\sqrt{3}}{8} H\gamma \quad , \qquad \text{Equation 50}$$

where e is the half-width of the shear band. From Equation 50, shear failure will occur at a critical indentation $\Delta_c = e\,\gamma_u$, where γ_u is the critical shear strain.

The energy absorbed by a statically loaded plate is

$$E_t = E_{bm} + E_s = \frac{F_u^2 - F_c^2}{2K_m} + \frac{F_u \Delta_c}{1+n} \quad . \qquad \text{Equation 51}$$

Equation 51 may be expressed in an alternative form as

$$\frac{E_t}{\sigma_y d^3} = A\left(\frac{H}{d}\right) + B\left(\frac{H}{d}\right)^2 + C\left(\frac{H}{d}\right)^3, \qquad \text{Equation 52}$$

where:

$$A = 0.138\lambda^2 \ln(R/a) \quad ,$$
$$B = 0.270\lambda^2 \ln(R/a) + 0.451\lambda\gamma_u/(1+n) \quad ,$$
$$C = 0.132\lambda^2 \ln\left(\frac{R}{a}\right) + \frac{0.440\lambda\gamma_u}{(1+n) - \left(\frac{\pi}{12}\right)\ln\left(\frac{R}{a}\right)\left[1+\left(1+\sqrt{\frac{3}{2}}\right)\Big/\ln\left(\frac{R}{a}\right)\right]^2} \quad , \qquad \text{Equation 53}$$

and E_{bm} is the energy associated with bending and membrane actions, E_s is the energy associated with shear deformation, $\lambda = \sigma_u/\sigma_y$ and σ_u is the ultimate tensile strength.

The strain rate sensitivity of the material is accounted for through the Cowper-Symonds relationship

$$\sigma_d = \sigma_y\left[1 + \left(\frac{\dot{\varepsilon}_m}{D}\right)\right] \quad ,$$
$$\dot{\varepsilon}_m = \frac{2W_{OS}V_C}{3\sqrt{2}Ra\,\ln^2(a/R)} \quad , \qquad \text{Equation 54}$$
$$W_{OS} = \frac{F_u - F_c}{K_m} \quad ,$$

where $\dot{\varepsilon}_m$ is the strain rate at plugging failure, σ_d is the dynamic yield stress, V_c is the ballistic limit velocity, W_{OS} is the displacement at failure and D and q are material constants.

At the ballistic limit, the energy absorbed by the plate is equal to the energy of the projectile E_p. In terms of the projectile mass G, $E_p = (1/2)GV_c^2$. Equation 52 can now be used for an approximate relationship to determine the ballistic limit velocity,

$$V_C = \sqrt{\frac{2\sigma_y d^3}{G}\left(\left[1 + \left(\frac{2W_{OS}V_C}{3\sqrt{2}DRa\,\ln^2(a/R)}\right)^{1/q}\right]\left[A\left(\frac{H}{d}\right) + B\left(\frac{H}{d}\right)^2 + C\left(\frac{H}{d}\right)^3\right]\right)^{1/2}} \quad . \qquad \text{Equation 55}$$

The model verification is carried out by comparing the results from Equation 55 with the test results published by Børvik in table 8 of [121]. The material properties and test geometry were taken from the same publication. The comparison between the predictions and test results is presented in Figure 65. A reasonable level of correlation can be seen except for the thickest armour section.

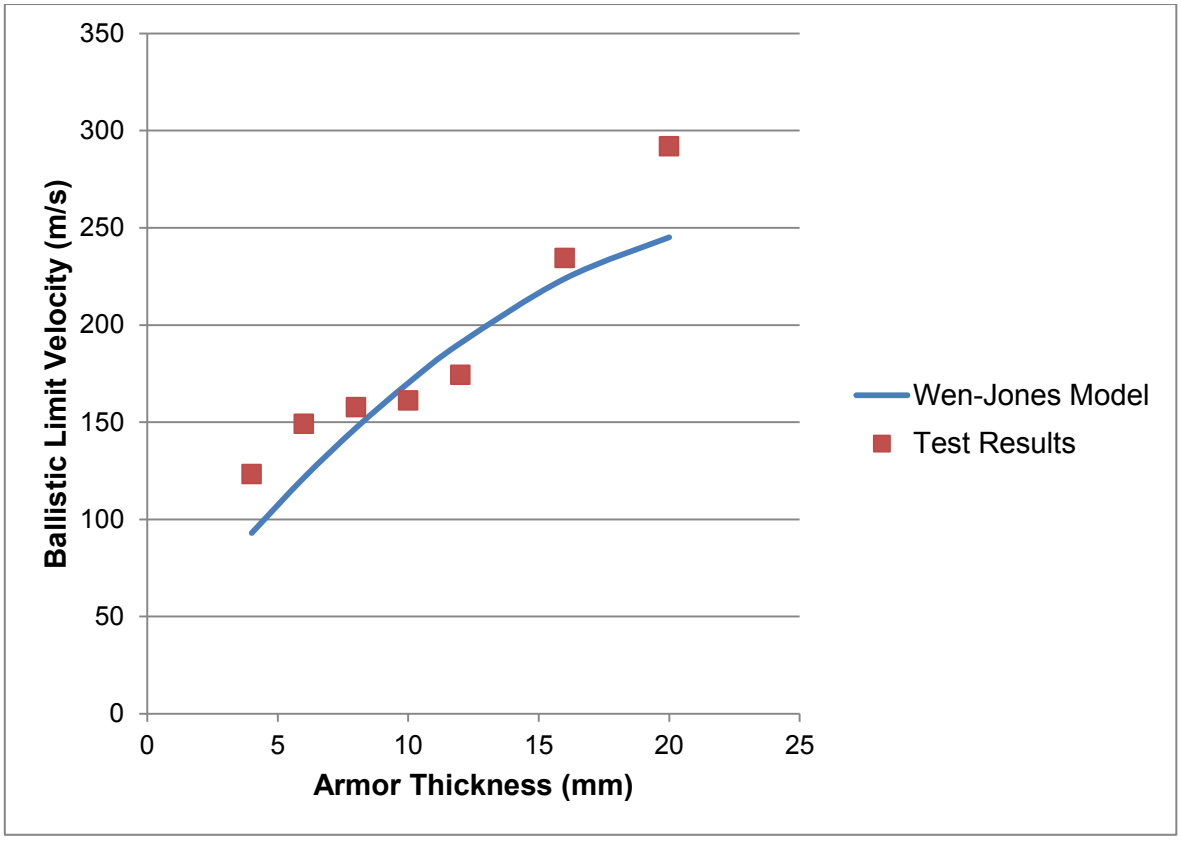

Figure 65: Comparison of the Wen-Jones model predictions and test results

The ballistic limit velocity may now be used in this work to calculate the initial velocity V_i on the plate where the residual velocity V_r is known. This is done by rearranging the Lambert and Jones model of Equation 59 in terms of V_r,

$$V_i = \left(\frac{{V_r}^p}{a^p} + V_C^p \right)^{1/p} . \qquad \text{Equation 56}$$

4.5 Derivation of the Ballistic Limit from Test Data

4.5.1 Definitions and the Determination of the Ballistic Limit

The ballistic limit velocity (V_{bl}) of a given armour panel is defined as the lowest velocity at which a certain projectile will consistently and completely achieve full penetration [122]. An alternative definition may also be given as the velocity at which the projectile consistently fails to penetrate the armour. In reality, a testing regime will yield a zone of results where the projectile will sometimes completely penetrate the armour or fail to do so under apparently

identical conditions. This scatter in the test data can be analysed statistically to determine the velocity (V_{50}) at which complete and incomplete penetration are equally likely to occur.

The overall procedure for performing these tests is given in MIL-STD-662 [122]. This standard specifies that the armour composition and thickness remain constant for all tests. Furthermore, the projectiles must remain consistent. The only variable is the initial velocity (V_i) of the projectiles. The initial velocity and the residual velocity (V_r) are measured and used to determine V_{50}. This method is not suitable for applying to the tests presented in this thesis, where the velocity of the projectile is held constant while the armour thickness is varied.

4.5.2 Current Analytical Models

A variety of analytical models are in existence, where those based on an approach of energy and momentum balance are of interest. One frequently cited method is that of Recht and Ipson [123] for relatively thin plates ($b/L_{imp} < 0.5$, $b/d < 0.5$), where b is the thickness of the plate, L_{imp} is the length of a cylindrical projectile and d is the diameter of the projectile. The formula for the residual velocity, which is based on energy and momentum balance, is:

$$V_r = a\left(V_i^2 - V_{bl}^2\right)^{1/2}, V_i \geq V_{bl} \quad , \qquad \text{Equation 57}$$

where:

$$a = \frac{m_p}{m_p + m_{pl}} \quad . \qquad \text{Equation 58}$$

The terms m_p and m_{pl} are the masses of the projectile and plug respectively.

Lambert and Jonas [124] identified deficiencies in the method presented in Equation 57, especially due to factors related to the variability of target deformation of thick panels. In response to these potential deficiencies they proposed a more flexible relationship, as given in Equation 59.

$$V_r = a\left(V_i^p - V_{bl}^p\right)^{1/p}, V_i > V_{bl} \quad . \qquad \text{Equation 59}$$

The value of p is derived from the test data by means of the least squares technique, with the constraint of p > 1.

A comparison was made between the Recht-Ipson equation and the Lambert-Jonas equation by Ben-Dor et al [125] using previously generated test data. The conclusion was that there is no significant difference between the two methods for the data that was analysed.

4.5.3 Proposed Analytical Model

The Recht-Ipson and Lambert-Jonas models are well suited to the analysis of data where the target thickness is fixed while the projectile velocity changes. An alternative model is required for the case where the target thickness varies while the velocity of the projectile remains constant.

This study proposes an alternative energy balance model. This model must also account for the practical issue of tests where the ejected material may be widely dispersed on the test range, making the measurement of the mass of the ejecta and the residual mass of the projectile impossible. To this end, a work term W is introduced. The term incorporates the work done internally within the panel and the kinetic energy of the ejecta. The resulting energy balance is given in Equation 60. This type of relationship is also proposed by Recht and Ipson for the case of a sharp impactor without plug formation [123].

$$\frac{1}{2}\left(m_i V_i^2\right) = W + \frac{1}{2}\left(m_i V_r^2\right) \quad . \qquad \text{Equation 60}$$

Rearranging Equation 60 for V_r:

$$V_r = \sqrt{\frac{m_i V_i^2 - 2W}{m_i}} \quad . \qquad \text{Equation 61}$$

Rearranging Equation 60 for W:

$$W = \frac{m_i}{2}\left(V_i^2 - V_r^2\right) \quad . \qquad \text{Equation 62}$$

Defining the work per areal mass of the panel, where A_m is the areal mass:

$$W_a = \frac{W}{A_m} \quad . \qquad \text{Equation 63}$$

At the ballistic limit where $V_r = 0$, substituting the zero value of V_r into Equation 60 yields Equation 64. Subsequently incorporating Equation 63 allows for the determination of the areal mass of the panel at the ballistic limit, as given in Equation 65.

$$\frac{1}{2}\left(m_i V_i^2\right) = W, \quad \text{for } V_r = 0 \qquad \text{Equation 64}$$

$$= W_a A_m \quad .$$

$$A_m = \frac{m_i V_i^2}{2W_a} \quad . \qquad \text{Equation 65}$$

It is assumed that the W_a term remains constant for the various panels. This assumption is based on the observation that the penetration resistance of a projectile through a composite laminate is constant as it traverses the thickness [126]. This behaviour makes the penetration energy directly proportional to the thickness of the panel and thereby also proportional to the areal mass. Abrate [126] examined a variety of ballistic tests on various composites and fibre metal laminates, and in all cases the energy of the projectiles that was lost in the panels was proportional to the thickness.

The proposed calculation method for a projectile that has set properties and several panels of varying mass is given below:

1. Tabulate the measured residual velocities and areal masses for each shot.
2. Determine the work term for each individual panel using Equation 62.
3. Divide the work term for each individual panel by the areal mass of that panel using Equation 63.
4. Check the results of the above calculation to determine if the assumption of the W_a term remaining reasonably constant for the different panels actually holds.
5. Determine the average W_a value for all the panels.
6. Use the average W_a value in Equation 65 to calculate the predicted areal mass of a panel that will reduce the residual velocity to zero.

7. The average W_a value may be substituted back into Equation 61 to derive the predicted curve of V_r against A_m. This curve may be used to compare the predictions made on the basis of W_a against the test results.

4.6 FML Ballistic Panel Design

The methods presented in section 4.3 to determine the ballistic limit of panels can be applied to the design of FML panels intended to resist a pre-defined threat. The process for carrying out such a design is presented, and subsequently the application of the proposed method to an FML panel that will stop an EFP is given.

4.6.1 The Design Process

The proposed design process is iterative, where the configuration of the FML panel is updated until convergence is reached. An assumed configuration of an FML is taken as a starting point and a progressive failure analysis, as per section 2.5, is carried out to determine the strength of the panel. The critical diameter of the penetrator for this panel is then calculated by two different methods. For the first method the equivalent thickness of a monolithic titanium plate for the FML is determined. This is done using the Frost method given in Equation 40. This thickness is used as an input to the modified Whipple relationship of Equation 47 to determine the critical diameter. The second method involves the use of the Schmidt – Holsapple relationship of Equation 39 to determine the critical diameter. The two predicted critical diameters are compared as a check. They should be similar in value. The critical diameter that has been predicted is then compared to the actual threat and the composition of the FML is changed accordingly. The process is repeated until convergence is achieved, where an overview is shown in Figure 66.

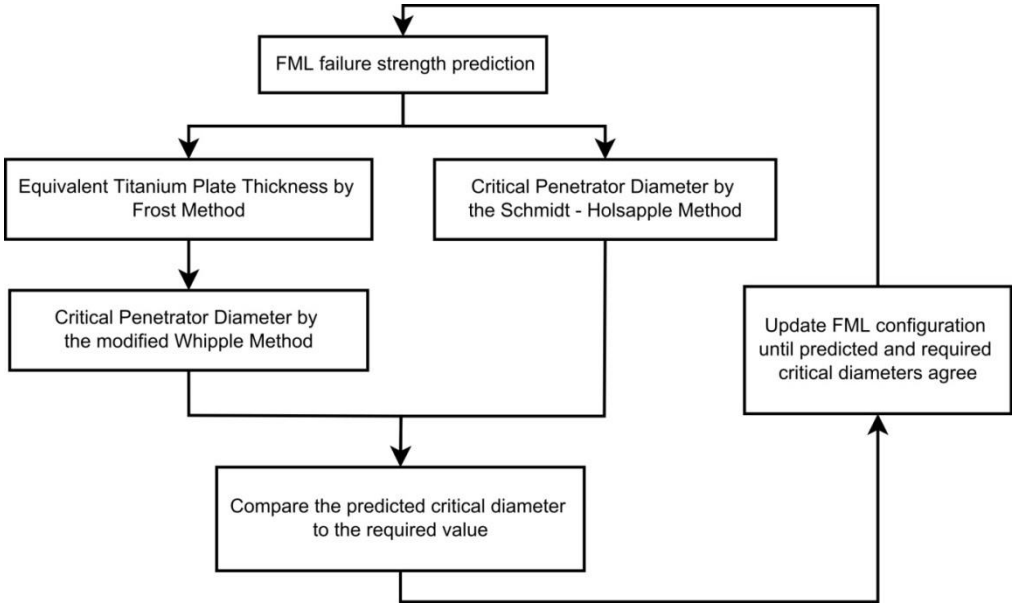

Figure 66: Overall ballistic design process

The variables used in this design method are given in Table 27. The initial inputs are given in the first column, where these values must be collated before the analysis begins. The intermediate results given in the second column are calculated from the initial inputs. The final results are then calculated from a combination of the initial inputs and the intermediate results.

Table 27: Factors in the design of an FML ballistic panel

Initial Inputs	Intermediate Results	Final Results
• Prediction of the failure strength of the FML using the Cuntze or Puck modified models • Carbon fibre areal mass • Number of carbon laminae • Fibre mass fraction • Titanium volume • Titanium density • Titanium sheet thickness • Panel area • Carbon lamina thickness • Titanium yield strength • Schmidt – Holsapple spallation factor • Density of the penetrator • Penetrator initial velocity • Angle of impact	• Mass of the carbon fibres • Carbon / epoxy mass • Titanium mass • FML panel mass • Panel density • Carbon / epoxy thickness • FML panel thickness	• Equivalent metallic plate thickness by the Frost method • Penetrator critical diameter by the Schmidt - Holsapple model • Penetrator critical diameter by the modified Whipple model

The initial inputs are changed according to the value of the predicted critical diameter until the predicted and actual diameters converge. The inputs that are most typically updated are the number of carbon laminae and the titanium sheet thickness. Any changes to these inputs will also necessitate an update to the FML failure prediction due to the change in configuration.

A single iteration of the design methodology is shown diagrammatically in Figure 67.

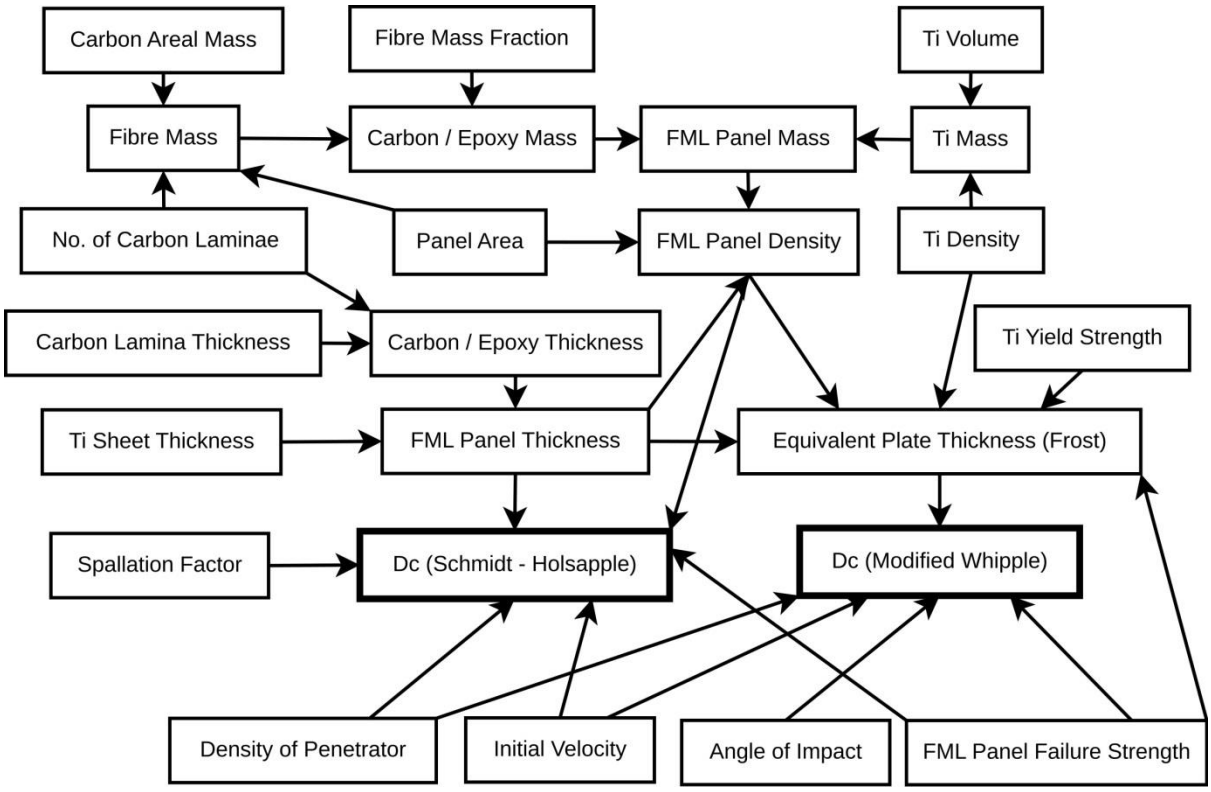

Figure 67: FML ballistic panel design methodology

4.6.2 Design of an FML Ballistic Panel

The method described above for the design of an armour panel was applied to a titanium / carbon-fibre epoxy FML panel, with the carbon fibres distributed in a cross-ply orientation. The material input properties were identical to those used for the mechanical tests in Chapter 3 since the same materials are used.

The results from the final iteration of the Cuntze based progressive failure analysis are presented in Figure 68. This a polar plot showing the first and last failure loads at various angles relative to the primary fibre direction. The specific analysis points are indicated as markers on the curves. There are several points where the final failure loads are less than

the initial failure loads. In these cases the initial failure is of the resin in all of the carbon epoxy laminae in the IFF1 mode. Subsequent to this level of failure the panel is not able to sustain this load level any further, with the final failure able to occur at a reduced load.

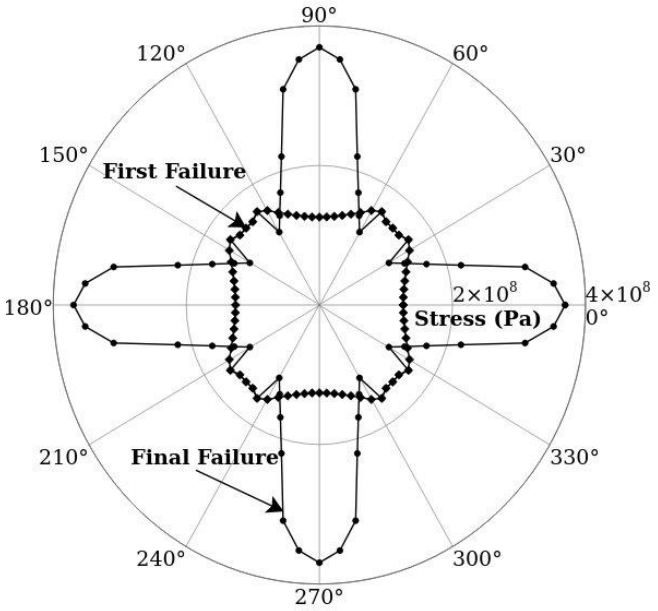

Figure 68: Failure polar of an FML armour panel using the Cuntze model

The results from the final iteration of the Puck based failure analysis is shown in Figure 69. The overall failure loads that are predicted are similar to Figure 68, although the shape of the first failure curve is different due to the different means of predicting the matrix failure.

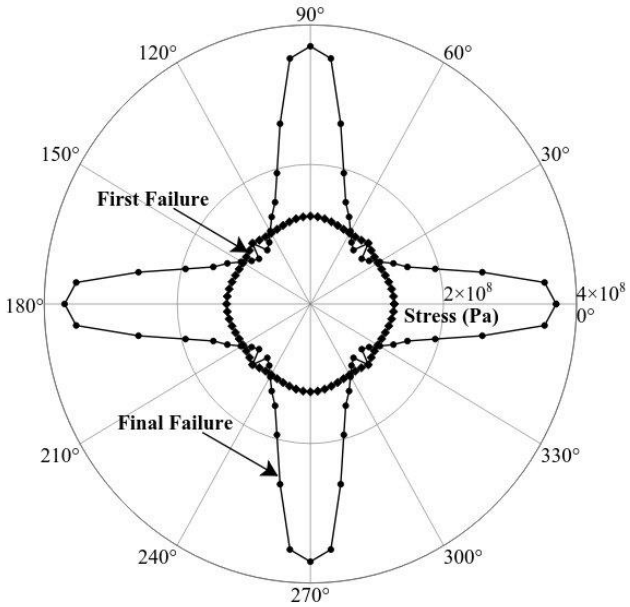

Figure 69: Failure polar of an FML armour panel using the Puck modified model

Examination of panels previously subjected to ballistic tests shows that the failure progressed preferentially in the direction of lowest material strength. This observation led to the selection of the lowest strength directions from the polar plots to provide the failure values as input to further analysis.

The threat has been identified as an EFP formed from a copper liner with a kinetic energy of 267 kJ. This threat definition, together with the material based inputs, allows for the calculation of the areal mass of a panel which would be sufficient to stop the threat. The areal masses calculated using the modified Whipple and the Schmidt – Holsapple methods are given in Table 28. The two different methods are in close agreement with each other.

Table 28: FML areal masses to stop an EFP

Method	Areal Mass (kg/m^2)
Modified Whipple	168.6
Schmidt - Holsapple	171.5

4.7 Ballistic Panel Development

4.7.1 Development Overview

The armour panel design process gives the thickness of the titanium and the carbon / epoxy composite, in addition to the lamination sequence for the composite. Further development is also required in order to translate the design into a viable manufactured panel that meets the performance requirements. A total of three test campaigns were initially carried out as part of the armour development programme before the fourth testing campaign was entered into. The insight gained as a result these initial campaigns guided the development of the design methods used, in addition to material selection and manufacturing methods.

The configuration of the armour panel selected for the fourth test campaign can be seen in Figure 70.

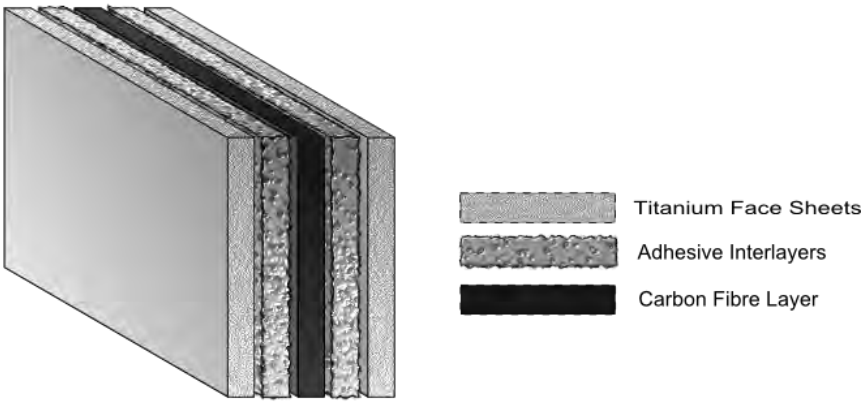

Figure 70: Composition of a typical armour panel

The armour panel configuration points towards several key elements that need to be addressed in a development programme, which are listed in Table 29. Some of the key elements cannot be dissociated from each other in a development programme, and these are grouped into overall categories. The description of the development work follows the structure of these categories.

Table 29: Key elements for armour panel development

Key Elements	Category
Metallurgical selection of the face sheets for best performance.	Face Sheet Material Selection
Surface treatment of the face sheets for optimal bonding.	Bonding and Surface Preparation
The toughened adhesive system to be used.	
The type of composite fibre for optimum strength and the geometry of the fibres for a balance of strength and through the thickness properties.	Composite Material Test Iterations
Selection of the matrix system to resist delamination	

4.7.2 Bonding and Surface Preparation

The initial ballistic panel tests showed significant delamination in the panels which was contributing to the failure modes. This delamination occurred both between the composite and metal face sheets in addition to internal delamination within the composite material. The ballistic resistance of the panels could therefore be enhanced by reducing the amount of delamination attributable to both in-plane shear failures and out-of-plane peel failures within the bonds. In many of the damage sites between the composite and the titanium the delamination was driven by cohesive failure, namely the adhesive separating from the underlying substrate. This failure mechanism was be addressed by an investigation into the surface preparation of the materials. An example from an early test firing showing an

adhesive surface that has incurred cohesive failure with the titanium face sheet is shown in Figure 71.

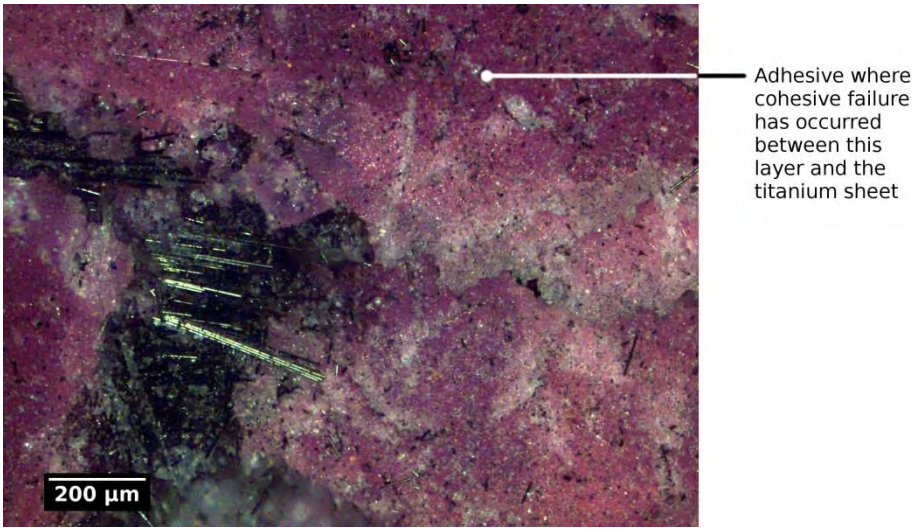

Figure 71: Cohesive failure between the adhesive and the titanium face sheet, focused stack

A view of the exit hole on a panel from an initial test shows no adhesive adhering to the titanium in the damaged area, adding a further indication of cohesive failure.

Figure 72: Exit hole from an initial test

The proper surface treatment of the titanium is a key factor in achieving maximum bond strength. The surface treatment is intended to modify the surface topography of the material through the introduction of surface roughness. This roughness allows the polymer adhesive

to effectively interlock with the crevices that have been formed. Three methods of surface treatment were investigated:

- Mechanical modification: The surface is abraded by means of grit blasting and subsequently cleaned with solvent to remove contamination.
- Sodium hydroxide anodisation: The anodisation process gives stable oxides on the surface which manifest as surface roughness.
- Laser ablation: This ablation process directly introduces micro roughness to the surface in a way that is highly repeatable.

The integrity of the bond between the adhesive and the resin of the composite was achieved by means of co-curing. The adhesive and laminate were manufactured simultaneously and allowed to cure together. This resulted in a chemical bond between the two materials.

The feasibility of the use of sodium hydroxide anodisation was first evaluated through a small-scale test, as shown in Figure 73. Initial trials of a sodium hydroxide based scheme were carried out to determine the overall process parameters on a small bench scale. The parameters of interest were the electrical current per unit area of titanium, the anode to cathode distance, total process duration and the applicability of the chemical concentrations used.

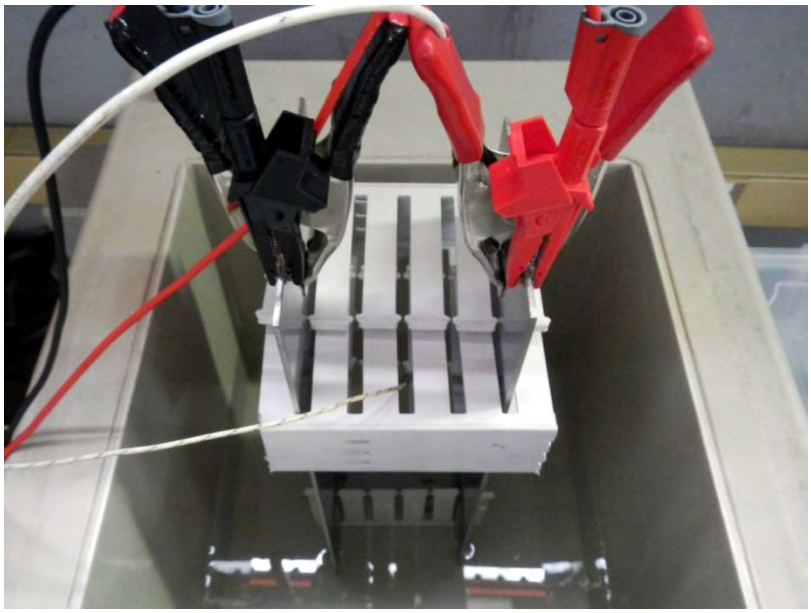

Figure 73: Small-scale anodisation test

Based on the results of the small-scale tests, a full-scale sodium hydroxide based anodisation facility was designed and established, as shown in Figure 74. Two titanium

sheets could be placed in a dipping frame and treated simultaneously. This facility was used to treat some of the titanium subsequently used for the armour tests.

(a) Dipping frame in tank (b) Tank and fume cupboard

Figure 74: Full-scale titanium anodisation facility

Bond strength tests were carried on the anodised titanium and also on similar sized grit-blasted specimens for direct comparison. The specimens were prepared from the hanging tabs that were used to suspend the titanium sheets into the sodium hydroxide bath. As a result of the geometry of these tabs the specimen size deviated from normal ASTM standards, and therefore the grit blasted specimens were made to an identical size to allow for direct comparison. The dimensions for both specimen types are as follows, with a test specimen shown in Figure 75:

- Length of titanium piece: 95 mm
- Length of carbon piece: 96 mm
- Specimen width: 39 mm
- Bonded overlap: 25 mm
- Titanium thickness: 3.2 mm
- Carbon thickness: 1.5 mm
- The carbon orientation is zero degrees along the length of the specimen.

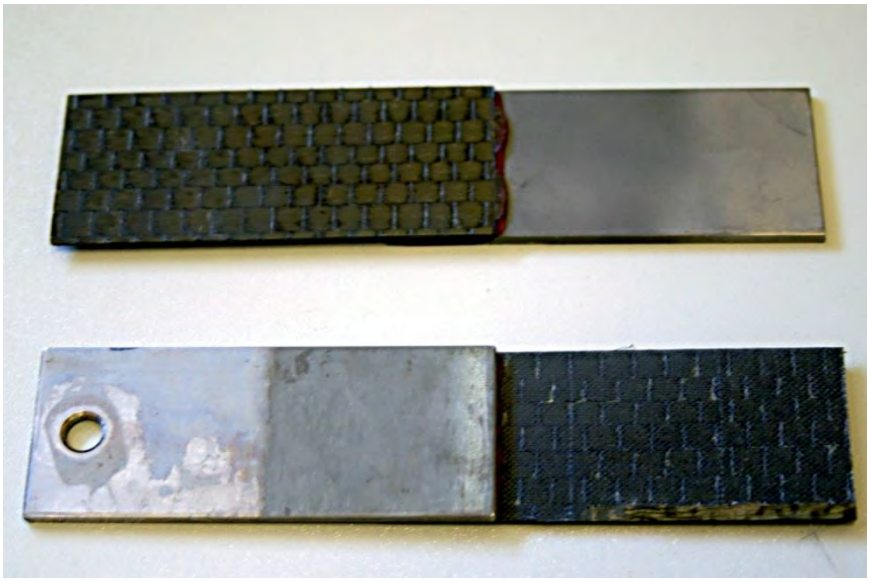

Figure 75: Adhesive test specimen for evaluating the anodisation process

The results of a comparative test can be seen in Figure 76, where specimen 1 has an anodised surface, while specimen 2 has a grit-blasted surface. The specimen with the anodised surface fails well before the other grit blasted specimen. Examination of the specimens shows that the bond failed due to the peel loading inherent in a single sided lap joint, where the brittle anodised surface was unable to sustain the peel loading.

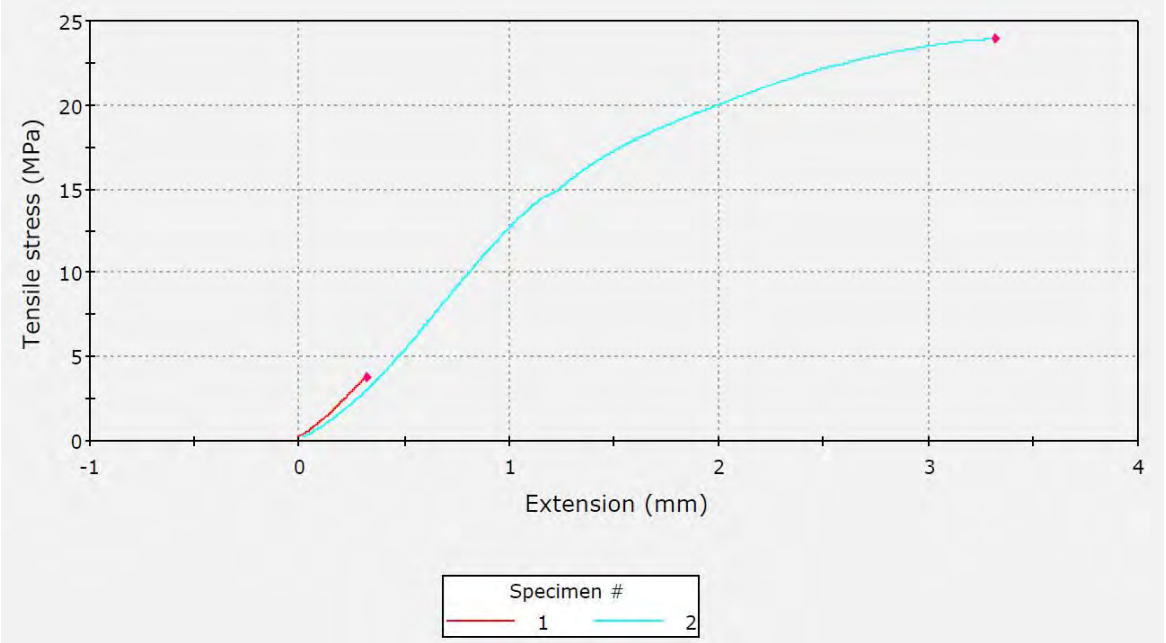

Figure 76: Bond strength test of anodised and grit-blasted specimen

The conclusions from the comparative adhesion tests are also reflected in the results of the first three armour panel test campaigns. The panels manufactured using grit-blasting for the surface preparation showed superior ballistic performance to those which used anodisation

as the method of surface treatment. The level of delamination was also lower with the panels where grit blasting was used. Some of the initial armour panels also included the use of hand abrasion for surface treatment, which was soon discontinued due to low ballistic performance.

The laser ablation of titanium 6Al-4V alloy was investigated as a more repeatable and controllable process than grit blasting. To this end, a series of test specimens were prepared that had been subjected to differing levels of laser ablation. These specimens were intended to determine the shear strength of the bond as a result of varying the ablation parameters. A number of standard tests were evaluated before settling on the ASTM D 1002 [127] test method. This method uses a single lap joint and has tension applied to it to induce shear in the adhesive holding two strips of metal together. The reasons for selecting this method are twofold: The method is relatively inexpensive in that it avoids the need for the manufacture of specialised jigs for the tests. Finally the test method also induces some out-of-plane peel stresses on the bond, an additional a relevant loading case which can show drawbacks in the surface treatment method.

Five test coupons were prepared, which required the ablation of the bond area on ten titanium strips. In all cases the laser was set to a pulse frequency of 35 kHz, line spacing of 10 microns and a spot size of 40 microns for surface treatments lasting 3 minutes. The primary parameters that were varied were the power in the range of 30 % to 70 % and the feed velocity of in the range of 300 to 400 mm/s. There was also some variation in the number of layers and the feed direction.

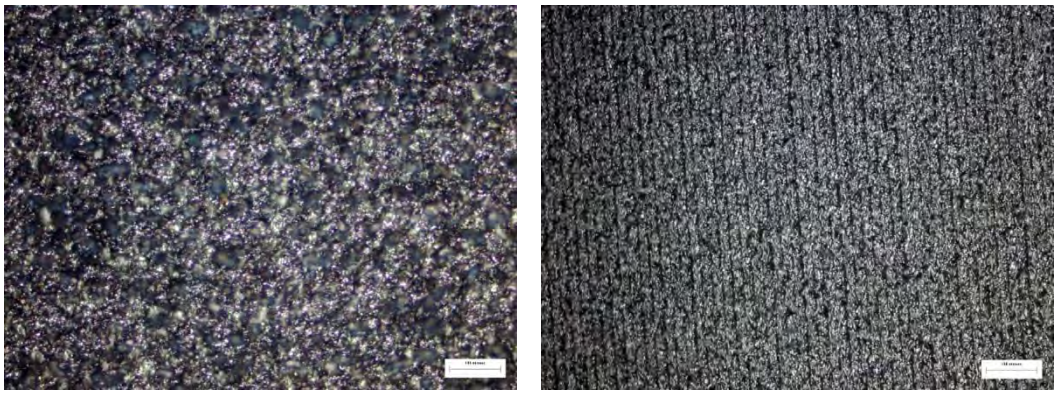

(a) 70 % Power Setting (b) 30 % Power Setting

Figure 77: Micrographs of laser ablated surfaces under 10x magnification

Subsequent to ablation the titanium strips were etched in a mixture of hydrofluoric and nitric acid for one minute to remove the surface oxidisation caused by the initial process. Pairs of

strips were then bonded together into test specimens using a Hysol 9309 adhesive. These specimens were tested to failure in a tensile test machine and the average shear stresses in the adhesive at failure were calculated. The following conditions applied to the tests:

- Load Frame: Instron Model 1342
- Load Cell: Instron rated at 50 kN static, 25 kN dynamic
- Data Acquisition: Instron Bluehill Software
- Extension Rate: 1.3 mm / minute

A specimen prior to testing is shown in Figure 78.

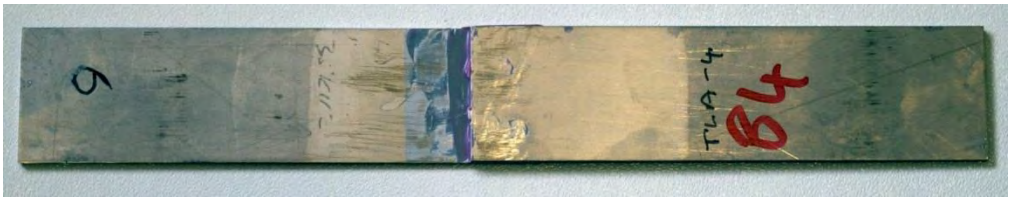

Figure 78: Bond test specimen for laser ablation of titanium

The shear stresses were in the range of 23.7 to 26.4 MPa, which is higher than those recorded for the anodised surfaces under similar combined loading. The mean stress was 25.4 MPa, with a standard deviation of 1.04. The test curves of the specimens are shown in Figure 79. These stresses compared favourably with specimens where grit blasting was used for the surface preparation. The disadvantage of the grit blasting is that unlike the laser ablation it is an uncontrolled process, so consistency cannot be guaranteed.

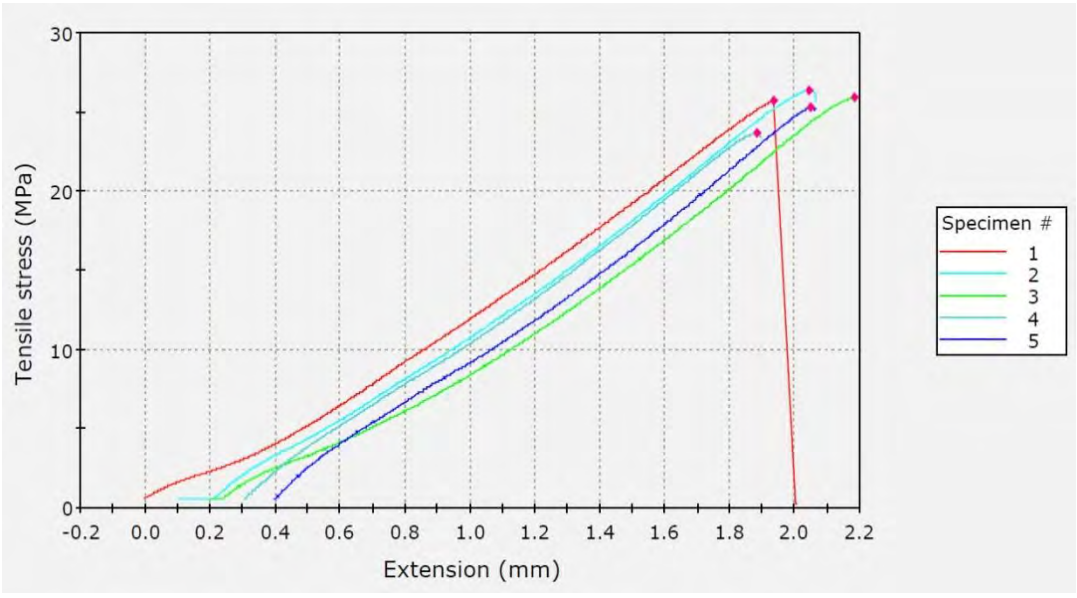

Figure 79: Extension - stress curves of the laser ablated bond test specimens

The laser ablation technique of surface preparation resulted in similar bond strengths to those obtained through the use of grit blasting. The grit blasting was the selected technique for the final armour test panels due to time constraints on manufacture, with the laser ablation technique being reserved for potential future application.

Alternative processes and materials for bonding were investigated further by placing a contract on the Department of Chemical Engineering of the University of Pretoria. The scope of the study was to investigate the bonding of carbon fibre to titanium using thermoplastic adhesives. A total of 118 titanium / carbon pairs were supplied to the University for surface preparation, bonding and testing. Some of the specimens incorporated the epoxy adhesive that had already been selected for this work. The conclusion was that the thermoplastic materials did not offer an advantage over the selected epoxy system, thereby confirming the original selection.

4.7.3 Composite Material Test Iterations

Initial investigations were carried out prior to the manufacture of the first armour panels. These investigations addressed the manufacturing considerations for the composite materials in isolation. The intention was to manufacture the thick composite part of the armour using a wet lay-up moulding process with subsequent consolidation. The reason for the investigation was that, although established manufacturing methods were being used, the composite laminates were unusually thick. This thickness required refinements to the manufacturing processes in order to obtain the required flatness, resin content and void content while avoiding exothermic reactions. The investigation led to guidelines for the ambient temperatures required at the different steps during processing and cure, the consolidation pressures and specific variations on lamination technique.

The series of three test campaigns were then entered into prior to the final ballistics tests, where armour panels were fired on by EFPs. These initial tests allowed for the exploration of material and manufacturing issues prior to the final design. Some of the panels had a composition of two titanium sheets as the outer surfaces together with composite cores, while others used three layers of titanium, with the additional layer being in the centre of the panel. Examination of the residual velocities of the penetrators showed that the configurations with two titanium sheets were the most mass efficient, resulting in this configuration being retained.

Two armour panels were manufactured using a toughened epoxy as part of a woven carbon pre-preg system that was intended for ballistic protection against rifle rounds. This system showed excessive delamination on test with a relatively low reduction in the velocity of the penetrator. Figure 80 shows both the carbon epoxy core and the titanium face sheet subsequent to the test. The composite core has delaminated along the laminar plane, in addition to showing brittle fracture in several locations perpendicular to this plane. The titanium face sheets delaminated completely from the composite core. This system was not retained for further testing.

(a) Carbon core (b) Titanium face sheet

Figure 80: Carbon pre-preg panel subsequent to test

Two armour panels were prepared where the uni-directional carbon epoxy laminae were alternated with woven aramid fibre laminae to aid with inter-laminar stress transfer. These panels delaminated readily under testing, splitting completely into several sections along the laminar planes. Subsequent examination showed that the delamination was attributable to the relative weak resin to fibre interface for the aramid material. A section where the carbon has delaminated from the adjacent aramid layer is shown in Figure 81. This configuration was also discontinued for further tests.

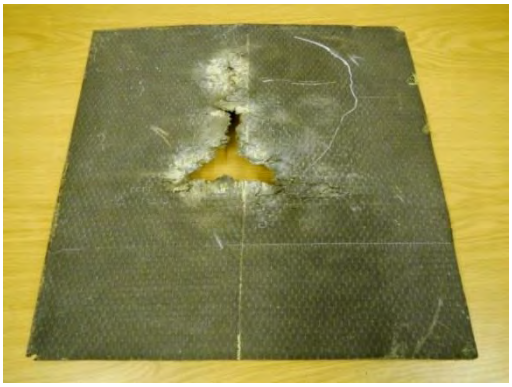

Figure 81: Delaminated carbon / aramid panel

The balance of the preliminary tests focused on panel manufactured from two outer sheets of titanium with uni-directional carbon epoxy cores. These panels were co-cured with a toughed epoxy system to bond the titanium to the composites. Variations were carried out on the consolidation pressure and the curing temperature, with the latter being guided by numerical simulations of the residual stresses in the panel after cure. The thermal stresses were calculated using the relationships presented in section 2.2. The lamination angles were also varied. The material cutting and the composite lamination are shown in Figure 82.

(a) Material cutting (b) Composite lamination

Figure 82: Manufacture of the titanium / carbon epoxy panels

The results of these initial investigations were used as input to the design and manufacture of the final panels.

4.7.4 Face Sheet Material Selection

The need for light weight led to the investigation of titanium for the armour protection. The Ti 6Al-4V form of the alloy was chosen on the practical grounds of the wide-scale availability of suitable thickness sheets and the relatively low price when compared to other titanium alloys.

The ballistic behaviour of titanium is driven by the dynamic deformation characteristics, the formation of adiabatic shear bands and phase transformations [128]. The ballistic performance of the selected alloy is largely characterised by the formation of adiabatic shear bands which are composed of dynamically recrystallized grains [129]. The alloy has the potential to have the ballistic performance enhanced further through modification of the microstructure in order to reduce the sensitivity to the formation of the adiabatic shear bands

[130], [131]. The aim of the modification was to achieve an equiaxed microstructure which consisted of a globular alpha phase in a matrix of a beta or transformed beta phase.

The refinement of the alpha grains to micron or sub-micron sizes may be achieved through thermo-mechanical processes, which would include heat treatment and hot compression. These processes are difficult to implement successfully towards the achievement of such fine grain structures due to the rapid grain growth in the material at high temperatures and the complex allotropic phase transformation. The Advanced Casting Technologies Group of the CSIR was approached to carry out the thermo-mechanical processing and subsequent scanning electron microscope analysis due their prior experience in the field with titanium. Figure 83 shows the original microstructure of the alloy with an equiaxed alpha phase.

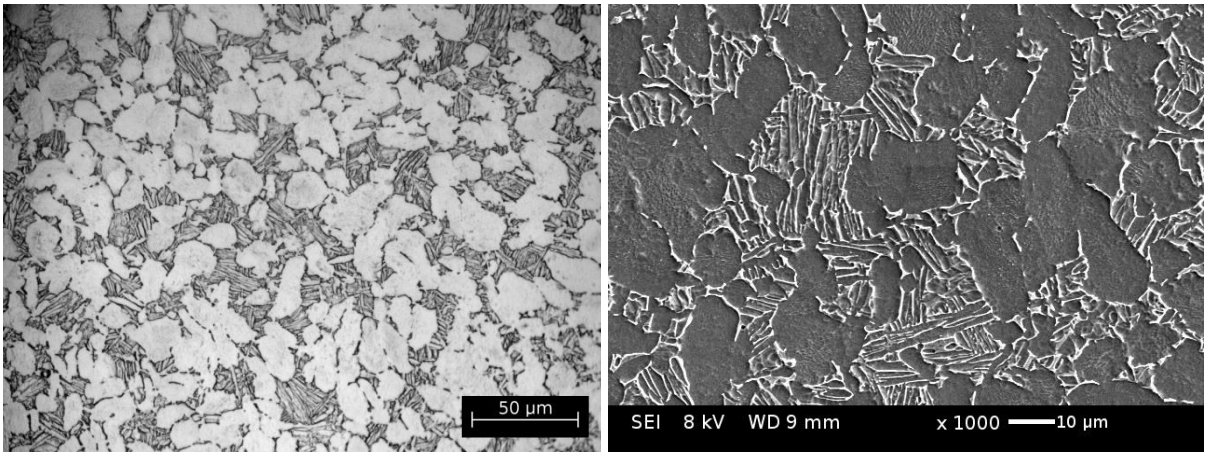

(a) Optical (b) SEM

Figure 83: Original alloy microstructure

The following refinement processes were carried out, with the corresponding micrographs shown in Figure 84, listed as:

- Heat treatment process for fully lamellar structure, Figure 84 (a)
- Heat treatment process for fully martensitic structure, Figure 84 (b)
- Hot compression for a fine-grained alpha structure, Figure 84 (c)
- Heat treatment process for equiaxed structure, Figure 84 (d)

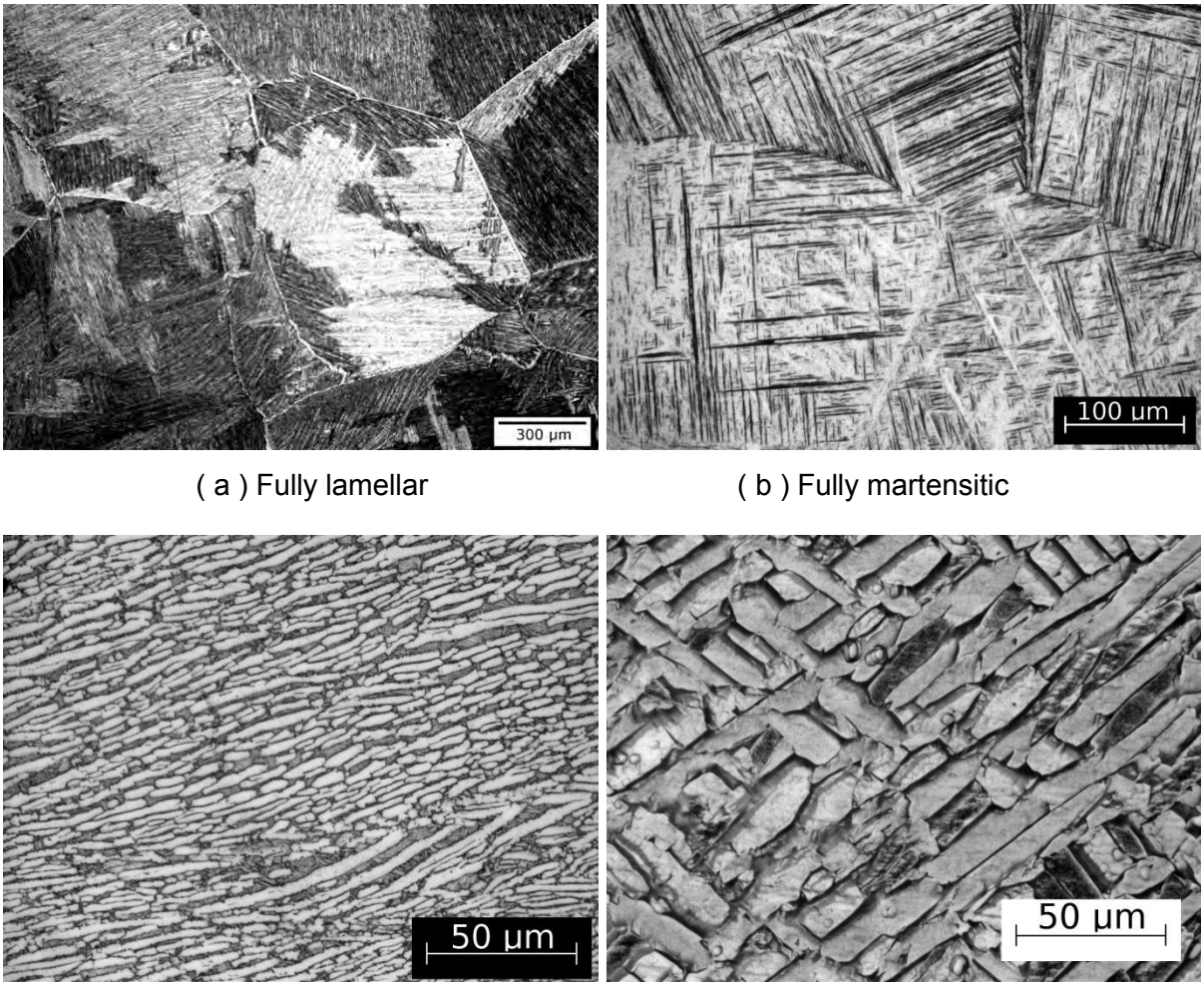

(a) Fully lamellar (b) Fully martensitic

(c) Fine-grained alpha (d) Equiaxed

Figure 84: Micrographs of Ti 6Al-4V subsequent to thermo-mechanical processing

The thermo-mechanical processing had not been sufficiently matured by the time of the final test campaign, and therefore standard wrought alloy was used. The processing may be applied to future work.

4.8 FML Armour Panel Ballistic Testing

The methodology and results of the fourth test campaign are presented below.

4.8.1 Test Layout

The ballistic tests were carried out at the CSIR Paardefontein test range, which is situated north of Pretoria in South Africa. This facility is specifically equipped for detononics,

explosives and ballistics testing, including the data acquisitions equipment for these events. The main bunker, as in Figure 85, was used as the site for the tests.

Figure 85: Paardefontein test range bunker

A schematic view of the test layout is presented in Figure 86. The EFP is placed at a distance from the armour panel, while a steel plate acts as a residual target behind the armour panel.

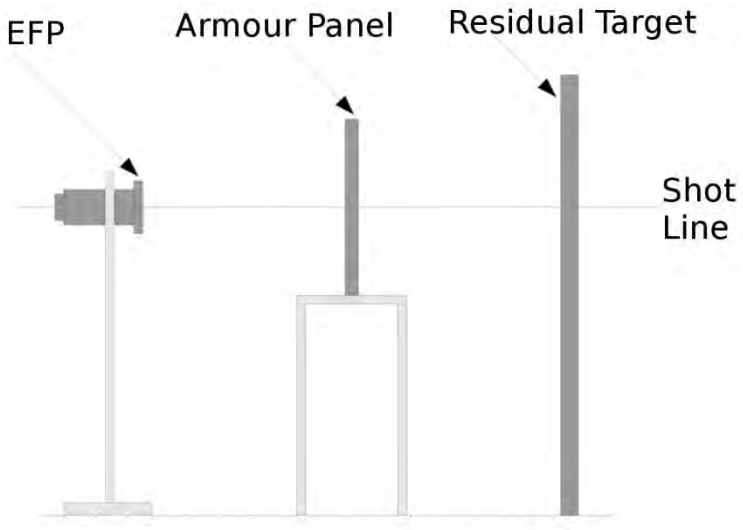

Figure 86: Test layout schematic

The EFPs, Figure 87, and the armour panels, Figure 88, that were used for the tests were placed on sacrificial wooden stands.

Figure 87: EFP as readied for testing

Figure 88: Armour panel on wooden stand prior to test

The residual target, Figure 89, is constructed of 50 millimetre thick steel plate. Examination of this target before and after each test provides insight into the residual debris exiting the back of the armour panel and subsequently impacting the target.

Figure 89: Residual target

The test layout viewed in the direction of the shot line can be seen in Figure 90.

Figure 90: Test layout

Measurement equipment was utilised to capture results during the tests. The bunker is equipped with Flash X-Ray (FXR) facilities that allow for the debris field exiting the panel to be captured at two discrete points in time. The degree of advance of the debris field between the two capture events allows for the determination of the residual velocity. A high-speed video camera, Figure 91, was used to capture the panel response and the exiting debris field during the tests.

Figure 91: High-speed video camera

4.8.2 Test Results and Discussion

The three panels for the parametric tests were subjected to impacts from EFPs, where the test data for subsequent analysis is drawn from the following sources:

- High speed video of the impact.
- Flash X-Ray (FXR) imaging of the impact.
- Post-impact macroscopic analysis.
- Post-impact micrographic analysis.

The high-speed video provides a qualitative assessment of the test. Figure 92 shows a succession of individual frames from the video, with the rear of the panel visible at an oblique angle in the centre of the frame. The time step between each frame is 1/100 000s,

with the shutter speed being 1/1 000 000s. The direction of approach of the penetrator is at an oblique angle, originating from the left in the images while approaching the viewer. The penetrator strikes the front face of the panel which is obscured due to the view, while the rear face is visible. The sequence of the frames starts at the top left and progress from left to right, with the progression being repeated on each subsequent row. The first frame shows the initial signs of penetration, which is only barely visible in the centre of the panel. Each subsequent frame shows the development of the debris plume from the rear of the panel. The bright background to the panel is due to combustion products that are attributable to the blast effect from the EFP, while the dark areas to the left and right are parts of the facility structures. The lighter coloured structure visible under the panel is the wooden stand that it has been placed upon.

Figure 92: Individual frames from high-speed video of the impact

The matter of primary interest in the video is the delamination of the panel during the progression of the penetrator through the panel. The images show that there was no macro level delamination during this time. The video also serves to confirm that the panel remains stationary during penetration and therefore all momentum loss in the penetrator is due to the failure mechanisms within the panel.

The Flash X-Ray (FXR) images of the penetration are presented in Figure 93 through Figure 95. The FXR images in each test are localised in the region of the panel, and show the penetration at two different times. The two different FXR exposures are superimposed on each image, and therefore a dividing line has been added to the middle of each image to assist with differentiating between the exposures. Note that panel 1 included a Weldox plate bonded to the back of the FML plate.

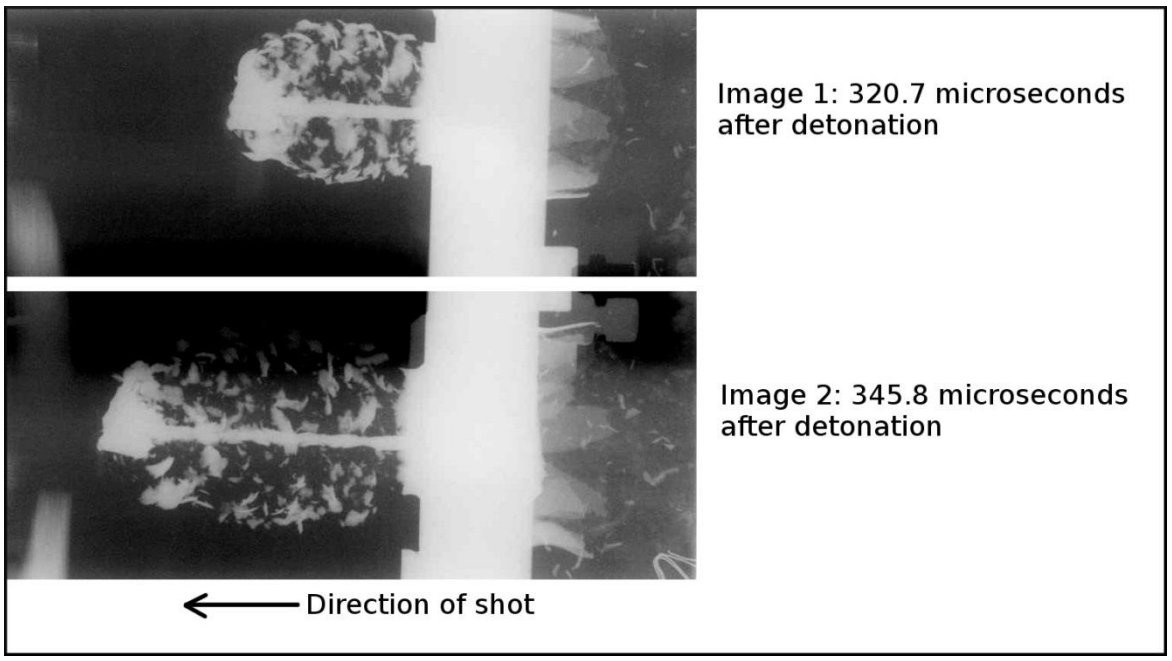

Figure 93: FXR of penetration through panel 1

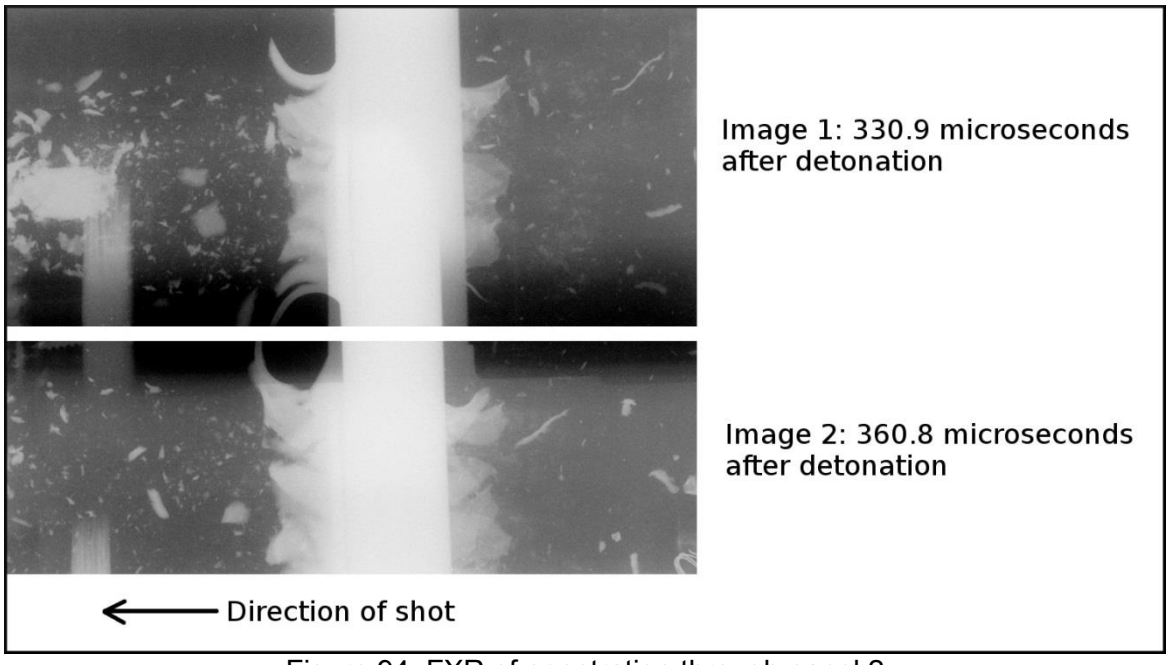

Figure 94: FXR of penetration through panel 2

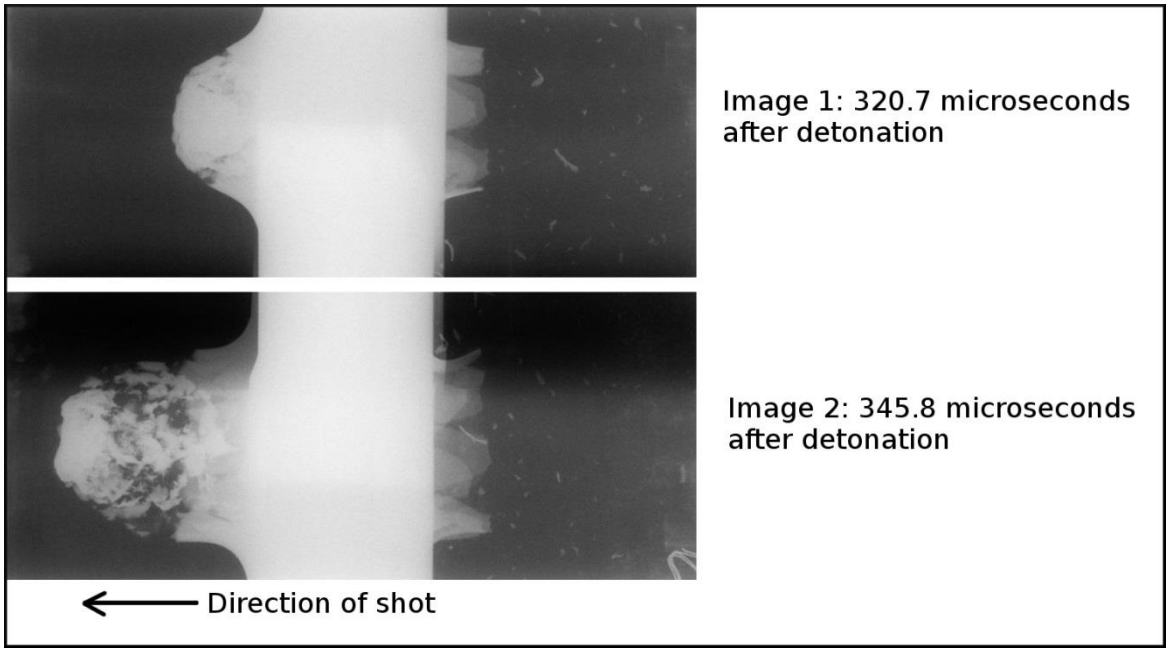

Figure 95: FXR of penetration through panel 3

The petalling behaviour of the titanium sheets may be observed in the FXR images, while the failure modes are well controlled. The staff at the Paardefontein test range carried out an analysis on the FXR images to determine the residual velocities of the debris exiting the rear of the panels. The residual velocities, as stated in Table 30, include an error band to account for variations in velocity in the debris cloud. The mean velocities presented are the velocities of the penetrators after passing through the panels as determined from analysis of the FXR images. The upper and lower bounding velocities that constitute the error range were obtained by determining the range of velocities in the overall debris leaving the panels.

Table 30: Residual velocities as determined from the FXR images

Panel No.	FX1 Time (microseconds)	FX2 Time (microseconds)	Residual Velocity (m/s)
1 Including Weldox	320.7	345.8	1397 ± 50
2	330.9	360.8	1979 ± 150
3	320.7	345.8	1270 ± 50

The masses of panel 1 and panel 3 are very similar when the addition of the Weldox plate attached to panel 1 is taken into account. The dynamics of the penetration do however show differences between these two panels. The penetrator passing through panel 1 has been severely constricted, indicating a small cavity size in the panel. The lack of delamination between the Weldox plate and the titanium sheet on the rear of this panel is also notable. The projectile passing through panel 3 shows significant delamination, indicating that the

increase in thickness of the FML panel is increasing the amount of work done against the penetrator.

The effect of the Weldox plate attached to Panel 1 must be discounted before this panel can be compared directly to the other panels. The modified form of the Lambert and Jones model given in Equation 56 is used to determine the initial velocity of the penetrator when entering the Weldox plate. This will correspond to the exit velocity from the FML panel. The value of p for this calculation is taken as being 2, while the value of a is extracted from Table 6 of [132] for the appropriate material, resulting in a=0.7. The resulting initial velocities derived from measured residual velocities for the Weldox plate are summarised in Table 31. In Table 30 the measured residual velocities are expressed as a range, which are then explicitly described as upper and lower bound and mean velocities in Table 31.

Table 31: Initial and residual velocities for Weldox plate of panel 1

Velocity Range	V_r (m/s)	V_i (m/s)
Lower bound	1347	1938
Mean	1397	2009
Upper bound	1447	2080

The corrected values of Panel 1, together with the values for the other panels, are summarised in Table 32 and are indicated in Figure 97. From here on Panel 1 without the Weldox will be referred to as Panel 1 for brevity.

Table 32: Summary of panel test velocities

Panel No.	Areal Mass (kg/m^2)	V_r Lower Bound (m/s)	V_r Mean (m/s)	V_r Upper Bound (m/s)
1	33.9	1938	2009	2080
2	60.2	1829	1979	2129
3	101.9	1220	1270	1320

The work W for each panel can now be calculated using Equation 62, and the work per areal mass W_a by Equation 63. The results of these calculations are given in Table 33, where the work terms are given for each panel at each of the three velocity points in the residual velocity range for that panel.

Table 33: Work done per panel

	V_r Lower Bound		V_r Mean		V_r Upper Bound	
Panel	W (J)	W_a ($J\ m^2/kg$)	W (J)	W_a ($J\ m^2/kg$)	W (J)	W_a ($J\ m^2/kg$)
1	71939	2120	57367	1690	42270	1246
2	93290	1550	63588	1056	31546	524
3	189846	1864	183372	1800	176638	1734

The results of the W_a calculations are also given graphically in Figure 96.

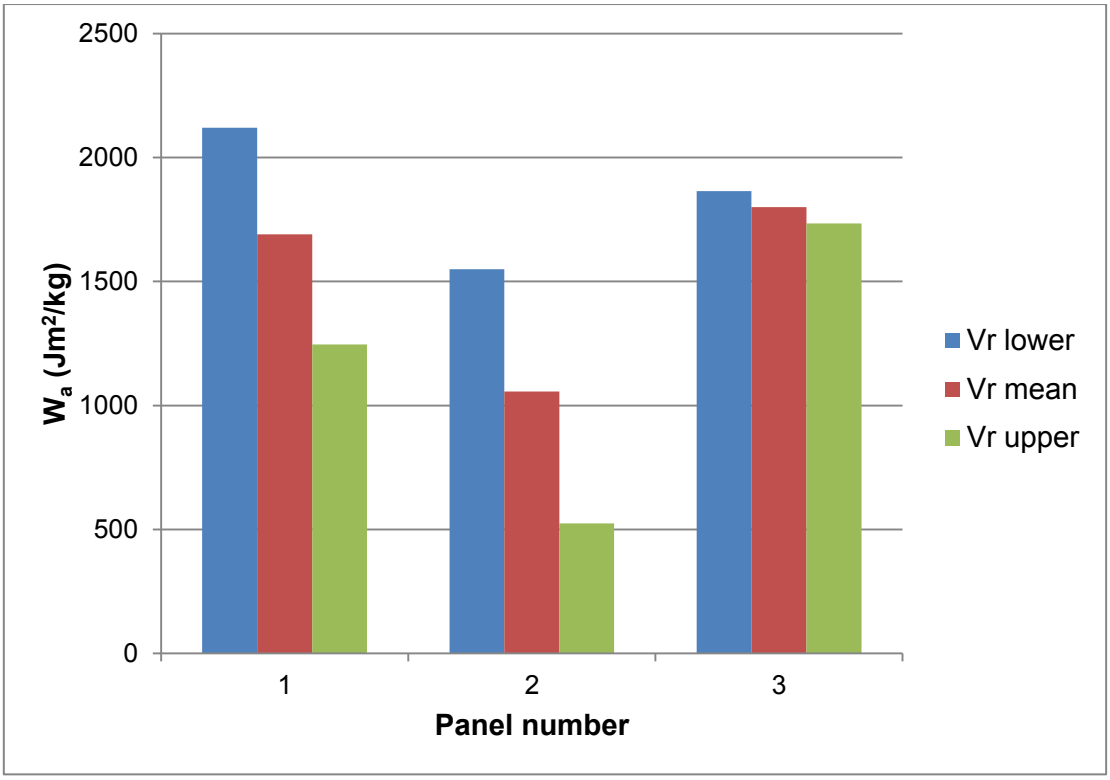

Figure 96: Work done per areal mass for the test panels

The average W_a can be calculated from the figures in Table 33 for each of the velocity regimes, namely the upper and lower bounding velocities, and the mean velocity. These average W_a values are then used for the determination of areal mass at the ballistic limit using Equation 65.

Table 34: Areal masses at the ballistic limit

	Velocity Regime		
	V_r Lower Bound	**V_r Mean**	**V_r Upper Bound**
Average W_a (J m^2/kg)	1845	1516	1168
Areal Mass at Ballistic Limit (kg/m^2)	145	176	229

The average W_a values may also be substituted into Equation 61 to determine the predicted curve of V_r versus A_m. Figure 97 gives a comparison between the velocities predicted by the energy balance model and measured velocities, where the intersection of the curves with the areal mass axis give the areal mass at the ballistic limit.

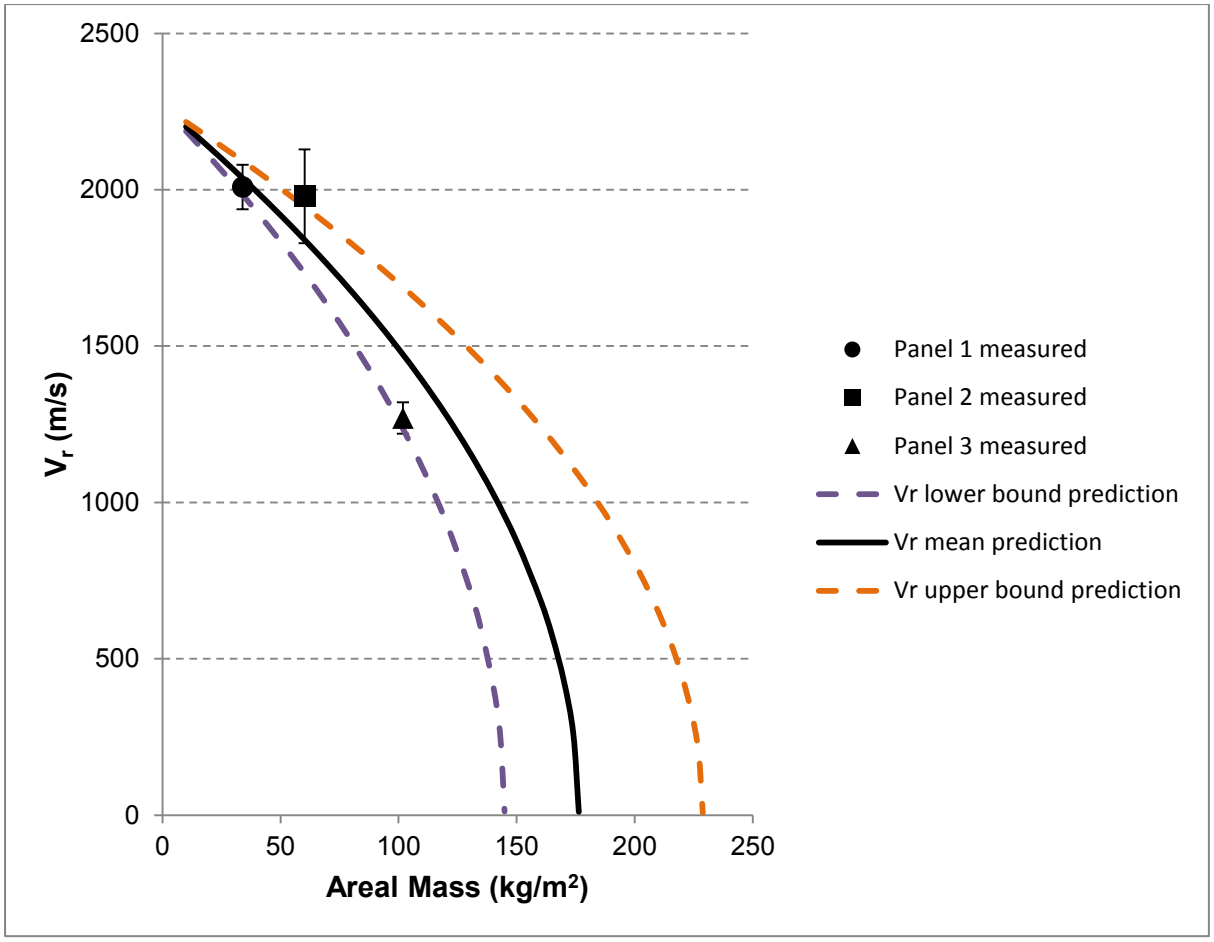

Figure 97: Comparison between the measured residual velocities and the velocities predicted by the energy balance model

The largest difference between the measured and predicted mean residual velocities in Figure 97 is for panel 3. This panel also exhibits the lowest velocity, thereby having the least impact on the energy calculations. A determination of the sensitivity of the predictions to the effect of the velocity associated with panel 3 was done. The mean residual velocity for panel 3 was adjusted to be the same as the value given by the energy balance prediction. The calculation of the areal mass at the ballistic limit was done with this new velocity, resulting in a 6.9% increase in the predicted mass. This result showed that the conclusions drawn from the test are not highly sensitive to some variation in this data point.

A comparison is drawn in Figure 98 between the areal masses at the ballistic limit from the test results and from theoretical predictions. The values from the test data match the theoretical predictions very closely for the middle V_r velocity regime. This is the test regime that is of primary interest due to the velocity representing the bulk of the kinetic energy of the debris. The difference in areal masses from the test and that predicted by the modified

Whipple method is 4.4 percent, while the difference to the prediction by the Schmidt – Holsapple method is 2.6 percent.

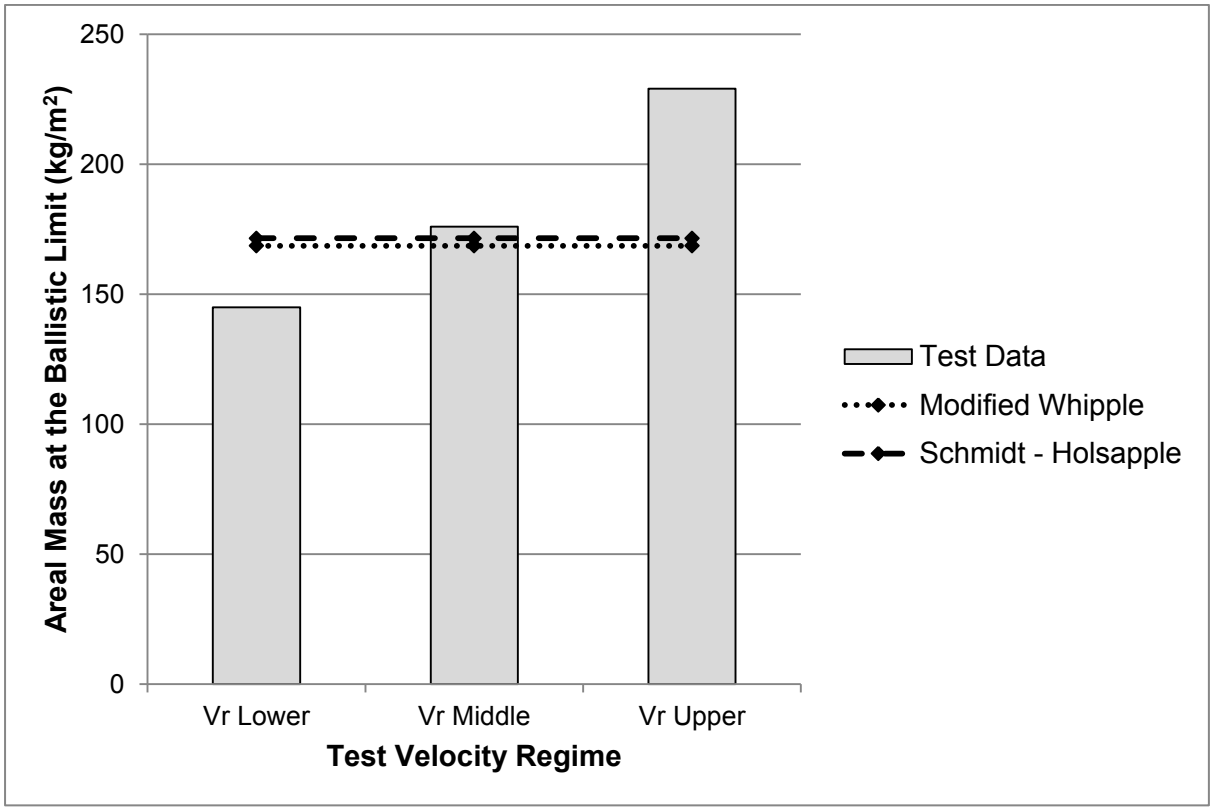

Figure 98: Comparison of areal masses at the ballistic limit from test and theoretical prediction

A macro-photographic survey of the panels was done after the conclusion of the tests in order to identify the overall failure modes. The previous FXR footage indicated a petal formation in the rear titanium sheet attributable to the passage of the penetrator. The overall fracture surface of one of these petal structures may be observed in Figure 99. This fracture surface is typical of what could be expected of a shear failure in the material, with steps in the surface parallel to the panel where the fracture direction followed the crystalline structure of the titanium alloy.

Figure 99: Failure surface of the titanium on the rear of the panel

Views of the composite material failure at the edge of the exit hole are shown in Figure 100 through Figure 102. The view in Figure 100 shows the fibres having rotated relative to each other in a scissoring fashion indicating shear failure within the matrix, while the fibres have also undergone tensile failure. The relative rotation of the fibres is also noticeable in a different view presented in Figure 101.

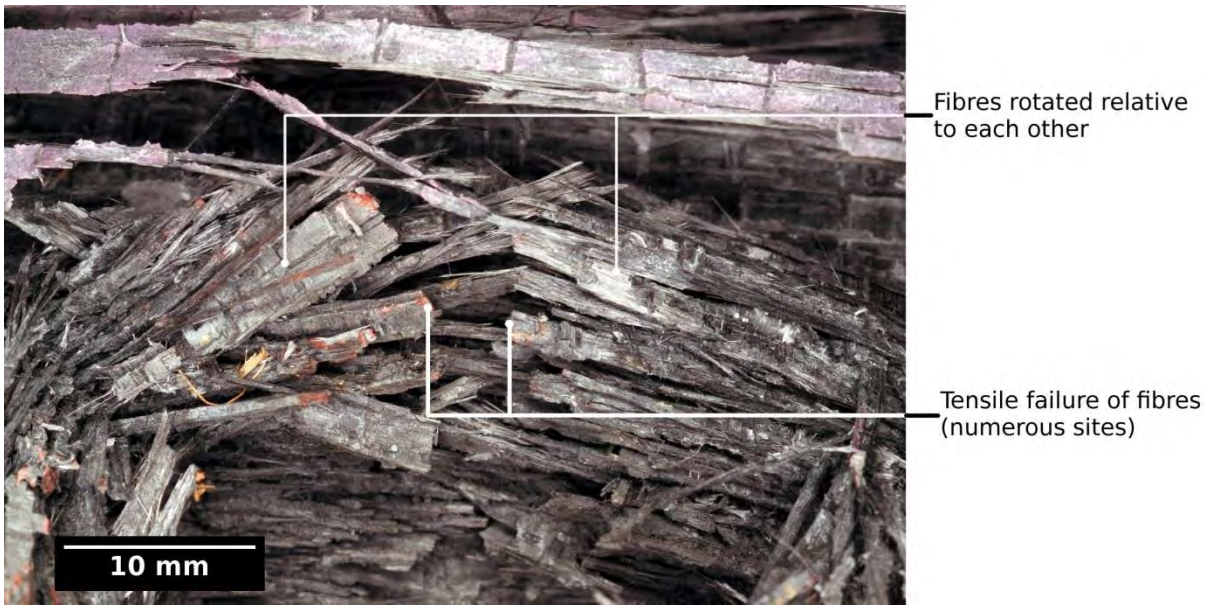

Figure 100: Composite material failure at the edge of the exit hole - view 1

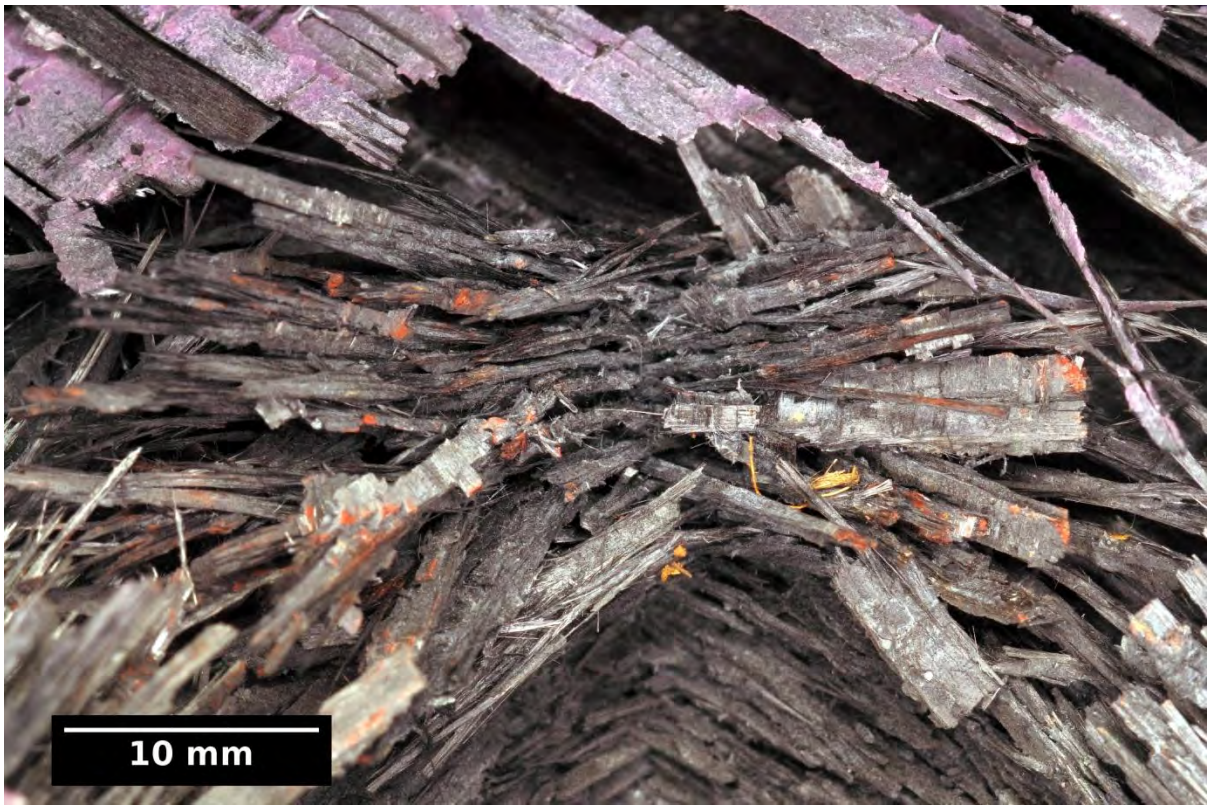

Figure 101: Composite material failure at the edge of the exit hole – view 2

During the design of the panel the composite material failure was anticipated to occur at a 45° angle to the primary fibre directions. The observed failure corresponds with this type of failure.

A view inside of the hole in the panel is given in Figure 102, where there has been bulk material removal due to the passage of the penetrator.

Figure 102: View inside the hole in the panel

The micrographic analysis of the panels provides further information on the failure modes. Figure 103 is a focused stack image of the carbon fibre in the area immediately adjacent to the exit of the penetrator. The image is a composite stack of 42 separate images that were generated at varying levels of focus through the subject, and then stacked using the ImageJ software to obtain an image with an extended depth of field. The tensile failure of the composite fibres is evident, as is the scissoring effect on the fibres due to shear loading.

Figure 103: Focused image stack of carbon fibre failure

A more detailed image of the failure of the carbon fibre, at 31 times magnification, can be seen in Figure 104. Previous tests where plugging type failure had occurred resulted in the fibre bundles being sheared off along a common surface. The fibre bundle that is shown does not exhibit a singular planar fracture surface, indicating tensile failure in the fibres rather than shear failure due to plugging. The implication is that the material behaved in the desired fashion, absorbing the energy in through the highest strength failure mode.

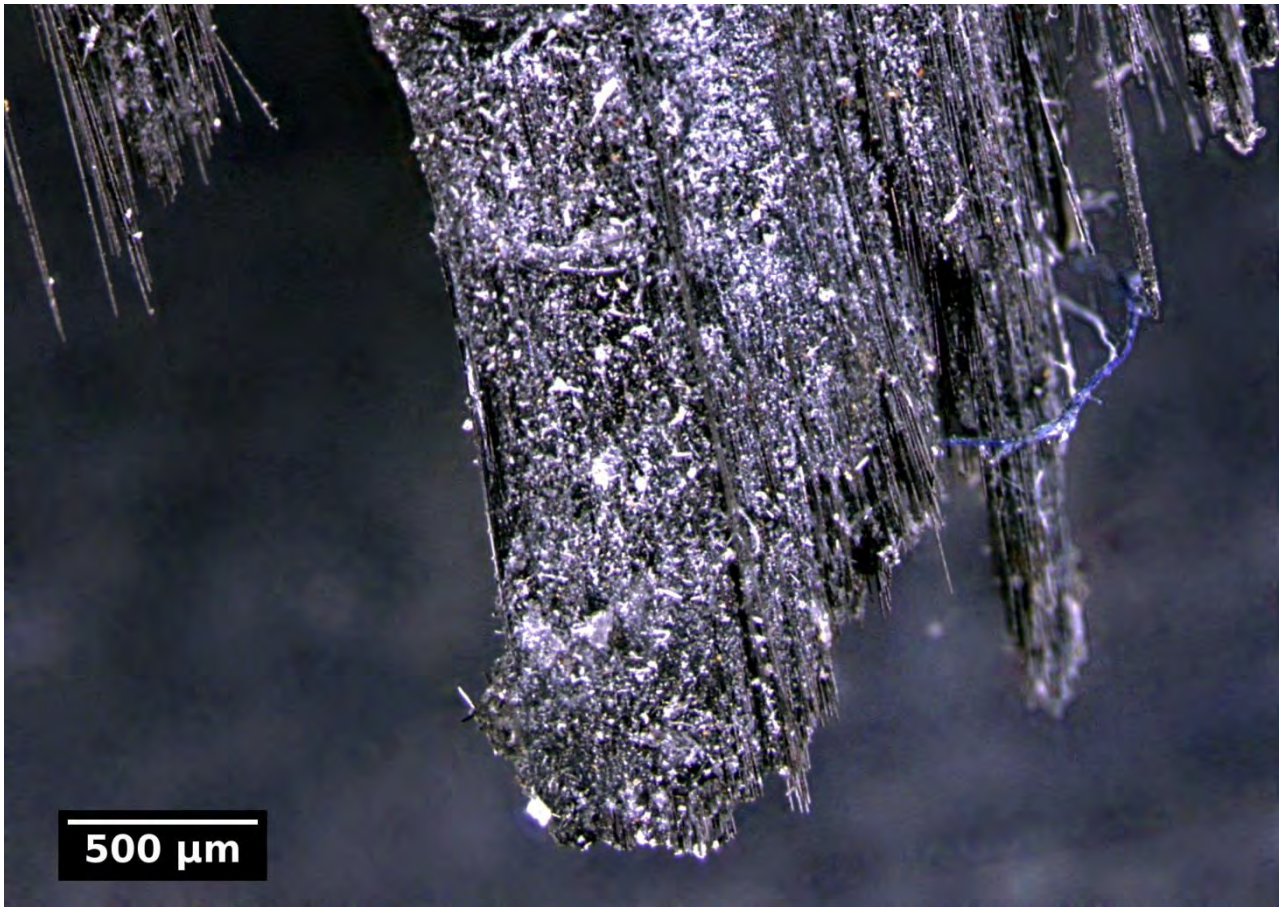

Figure 104: Detail of the carbon fibre failure, focused stack

An infrared thermographic inspection was carried out of the entire face of the composite laminate where the penetrator exited. The intent was to determine if there where further large scale failure modes in addition to those already identified by means of the macroscopic and micrographic examination. The test setup can be seen in Figure 105 (a), while the output image is given in Figure 105 (b).

The output clearly shows the damage around the hole formed by the penetrator which has already been noted. Delaminations extending inwards from the edge of the laminate are also evident, which is a common characteristic with thick composite laminates under load. These edge delaminations show no sign of having interacted with the failure mechanisms around the hole.

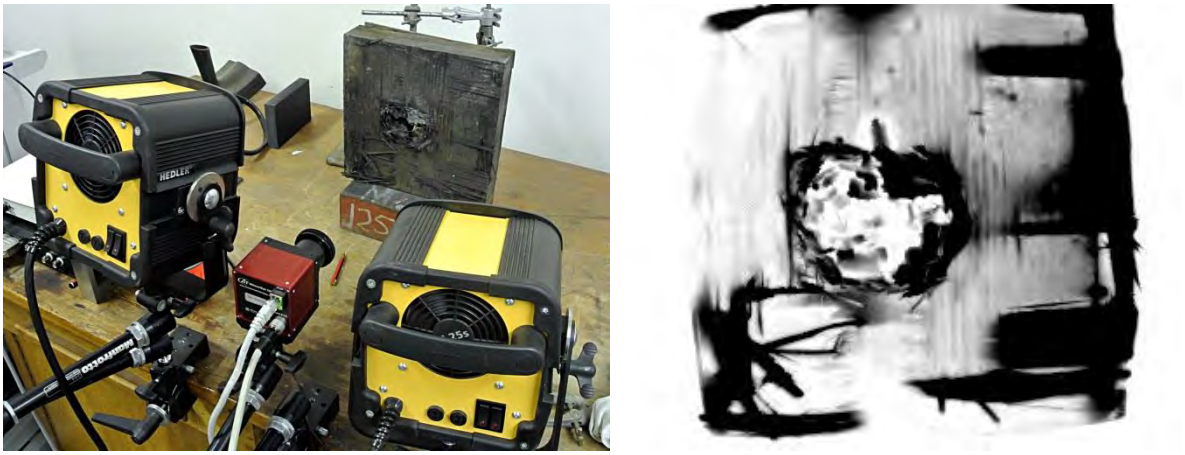

(a) Test setup (b) Test output

Figure 105: Thermographic inspection of the armour panel

A detailed post-test analysis of the titanium was carried out by means of Scanning Electron Microscopy (SEM). The images were generated by the Advanced Casting Technologies Group of the CSIR in Pretoria and are shown in Figure 106 through Figure 108.

The fracture within the titanium is typically driven by the formation of adiabatic shear bands. The bands are a highly localised deformation in an alloy that typically occur under high strain rate conditions [128]. These bands are the product of thermo-mechanical processes where plastic work is converted into heat. The bands are narrow, with a width of 5μm to 100 μm [133]. The formation of the bands becomes more pronounced at strain rates in excess of 10^3 s^{-1}, with typical causative conditions including the penetration of armour [134]. The process is not truly adiabatic due to the heat conducting away from the affected area, but rather the rate of heat loss is small in comparison to the rate of heat generation under high strain conditions. This high rate of heat generation results in thermal softening which exceeds the effect of strain hardening within the area of the band, with recrystallization occurring upon thermal recovery [128]. A decrease in grain size is evident within the adiabatic shear band as a result of the recrystallization, reducing to nanometre sized grains being present at the core of the band [133].

Examples of adiabatic shear bands observed in the failed titanium sheet may be seen in Figure 106, where the characteristics are similar to similar bands presented in [135], [136] and [137].

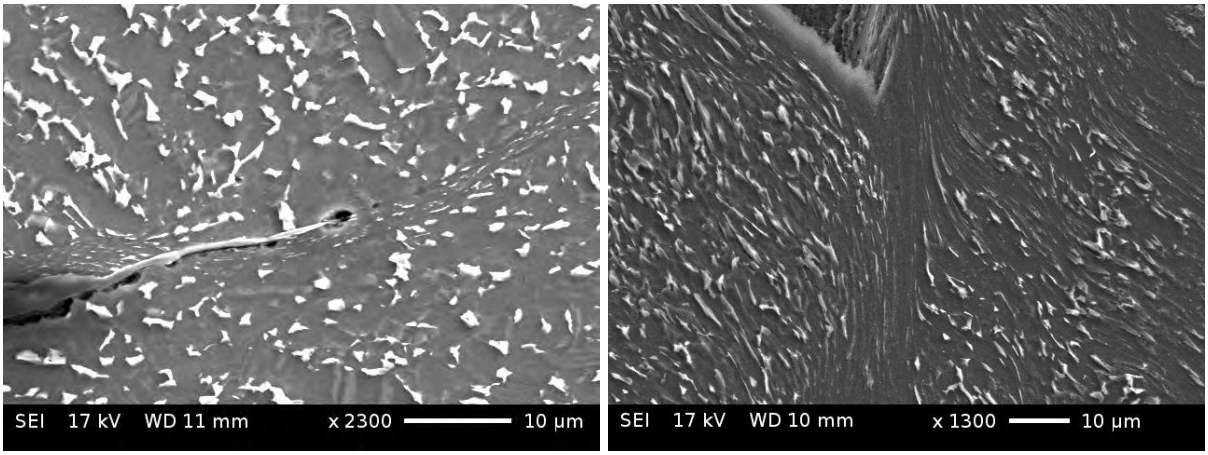

Figure 106: Adiabatic shear bands within the failed titanium sheet

The shear bands are the precursors for fracture due to the associated void nucleation, growth and subsequent coalescence that occurs within these regions [137]. Evidence of this void evolution is given in Figure 107.

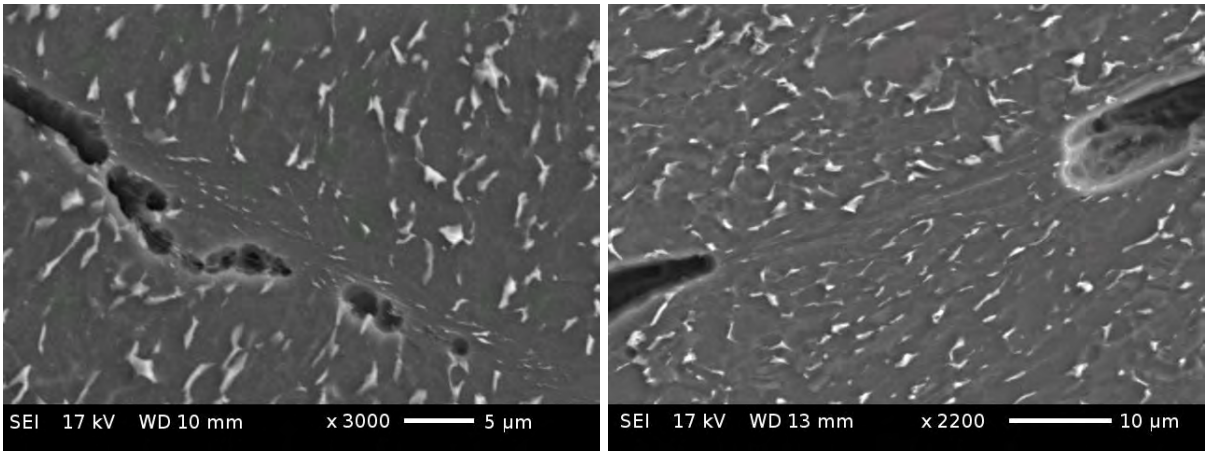

Figure 107: Void evolution within adiabatic shear bands

The formation of elongated dimples within the fracture surface of titanium under high strain rate conditions has been noted by various researchers [128], [134], [136]. Similar dimples were noted during the SEM examination of the armour panels under test, as in Figure 108. These fracture surfaces are ductile, which indicates that ductility was not lost during the failure event [128]. Chiou et al [134] studied the formation of these dimples at various temperatures. The dimples observed in the armour panel exhibit similar morphology to those formed in the 300°C to 500°C range that were described by Chiou.

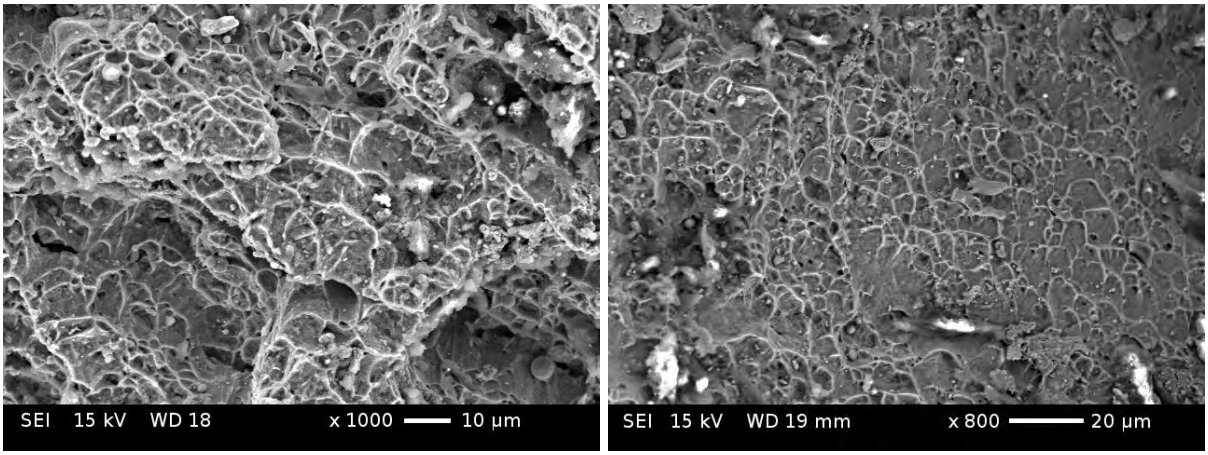

Figure 108: Ductile dimples within the titanium fracture surface

The conclusion is that the formation of adiabatic shear bands, which is the precursor to the failure, by ballistic impact is favoured by the equiaxed microstructure of the Ti 6Al-4V plate. The adiabatic shear banding should be prevented as much as possible in order to improve the ballistic performance of armour plates, where the use of a bimodal microstructure may offer some advantages.

The literature surveyed as part of the material selection for the face sheets in section 4.7.4 indicated that the ballistic performance of the alloy is driven largely by the formation of adiabatic shear bands. The SEM analysis of the test panels verifies that this behaviour did occur.

4.9 Conclusions on the Ballistic Theory and Testing

A need has been identified in this work for the development of a method to predict the static failure modes of titanium / carbon based FMLs. This need was driven by the requirement for higher performance materials in the aerospace field and also by the requirements for lighter weight vehicle armour. In response to this need, this thesis has developed a failure model for titanium / carbon FMLs order to provide insight into the progressive failures in the material up to the point of final failure.

The development of the failure model highlighted the additional work which would be required as part of this thesis in order to both prove the failure model and also to apply the model in a practical design environment. The laboratory scale testing of the model has required the introduction of additional measurement and observational techniques in order to quantify the initial failure modes for comparison with the predictions. The design of armour

panels has required the development of predictive ballistic models to span the gap between the predictions of the static failure model and the execution of viable designs. The development and testing of the armour panels has necessitated investigations into the manufacturing methods and also the analysis of the test data.

The laboratory level tests have proven the viability of the static failure model, while the agreement between the ballistic tests and the predictions validates the chain of the static failure, ballistic predictions, manufacturing methods and finally the analysis of ballistic test results. These outputs indicate that a baseline for further research into FML armour has been established.

The determination of the static failure modes as an input to the ballistic theory highlighted the need for further work in the biaxial testing of laboratory specimens as additional proof of the failure model. The manufacture of the armour panels indicated that further work on the prediction of residual stresses due to thermal effects would be beneficial.

Chapter 5. Concluding Remarks

5.1 Overview of the Study

Fibre Metal Laminates (FMLs) incorporating titanium and carbon fibre epoxy constituents are promising materials for the application to structures when neither metals nor composite materials are suitable. The lack of suitability may be due to constraints related to mass, fatigue or the effect of localised damage. These properties make the material well suited to meeting the needs arising from applications in the aerospace sector. An additional need is for the protection of armoured military vehicles in the case where the mass of conventional armour would be impractical.

There is a lack of verified numerical models that can be used in the engineering design process for predicting the static failure strength of titanium / carbon FMLs. This study incorporated the development and subsequent verification of such a model. Verified failure models were initially identified for each of the carbon / epoxy and titanium material constituents. These models were then incorporated into a global model for the prediction of the progressive failure in an FML. The predictions from this model included all failure modes up to the final collapse of the material. The static failure modelling of FMLs was extended further to allow for the prediction of ballistic penetration. The ballistic modelling aspect was addressed through the adaptation of work done by the space industry on the effect of high velocity impact on spacecraft structures. The static failure and ballistic models were both implemented in software that was developed specifically for the purpose. The output from the software was compared to separate calculations to confirm the software functionality.

The experimental substantiation of the FML failure model was carried out in two phases. The first phase was a laboratory level validation by means of the mechanical testing of specimens. The second phase consisted of ballistic field tests which provided a functional validation under realistic conditions of the ballistic models, and thereby also the static failure model incorporated into these ballistic models.

The laboratory level mechanical testing determined the progressive failure modes of the material from initial through to final failure. These specimens included a variety of lamination angles for the carbon fibre epoxy constituent in order to induce different failure modes. The monitoring techniques used included both audible and micrographic means, in addition to

micro-focus X-Ray examination. The results of the mechanical tests gave confidence in the predictive capabilities of the FML failure model.

The ballistic tests determined the panel mass required to stop a pre-defined penetrator. The proposed ballistic failure model agreed closely with the test results. This outcome gave confidence in the both the predictive ballistic model and also the FML static failure model that was incorporated in the ballistic model. The subsequent examination of the test panels showed failure modes in line with the predictions.

5.2 Contributions to the field

The contributions to the field fell within three categories, as given below;

A method to predict of the progressive degradation of FML panels under load: The modelling the progressive failure of titanium / carbon based FMLs under static loads has received relatively little attention in the literature. This work contributes to the field through the development of a progressive failure model which predicts the progressive degradation of the laminate as the applied load increases up to the point of final failure. This model includes composite failure models which are selected on the basis of their ability to model the failure mechanisms in FMLs.

A method to determine the ballistic resistance of FML panels: No methods have been reported on in the literature for the failure modelling of FMLs under high-velocity ballistic impact where the methods include the static failure characteristics of a panel as an input to the predictions. Two ballistic failure models were therefore developed which incorporate the previously developed progressive static failure model for FMLs as an input to ballistic predictions.

Contributions to static and ballistic test methods: Further contributions were made to the generation and analysis of data for both the static and ballistic tests on FMLs. The static tests included the use of three different sample monitoring techniques that were combined into a single procedure. The analysis of the combined data from these techniques allowed for the determination of the damage progression in the specimens. A method did not exist for analysing the data from ballistic tests where the masses of the panels are varied between tests while the velocity of the penetrator is kept constant. A contribution was made through

the development of a method to determine the ballistic resistance of the panels based on the test results from panels of varying mass with a constant velocity penetrator.

5.3 Recommendations for Further Work

The mechanical tests which were carried out to verify the failure progression model were uni-axial in nature. Further validation could be provided by carrying out the tests under multi-axial loads.

The analysis of the effect of thermal stresses on the FML indicated that these could be of significance in practice, notably the stresses in the adhesive layer between the composite and the metal. Additional work could include mechanical testing at elevated temperatures, with the possible inclusion of moisture absorption which would weaken the panel further.

The Cuntze material model that was implemented was of a simplified form intended for engineering analysis. The reason that Cuntze presented the simplified version was due to the difficulty and cost associated with characterising all of the material properties required for the implementation of the full version of the model. Additional work could include an investigation of alternative methods of implementing some of the features of the full model without the need for additional material characterisation. The same investigation could also apply to the full version of the Puck model, which was not included in this study due to the requirements for the material characterisation activities.

The performance of the armour panels may potentially be enhanced through the thermo-mechanical processing of the titanium alloy to refine the alpha grain size. An initial investigation was carried out, but the process was not fully matured to be point of being practical to implement. Further development of this thermo-mechanical process may be beneficial.

The establishment of the research baseline for FML armour has allowed for the ongoing exploration of alternative material systems and armour configurations. This further work will add additional refinement the analytical, testing and manufacturing techniques.

Bibliography

[1] A. Vlot and W. Gunnink, *Fibre Metal Laminates an Introduction*. Kluwer Academic Publishers, 2001.

[2] R. R. Boyer and R. D. Briggs, “Titanium cost reduction strategies for Boeing Aircraft,” in *Materials Forum*, 2005, vol. 29.

[3] P. Cortes and W. J. Cantwell, “The prediction of tensile failure in titanium-based thermoplastic fibre–metal laminates,” *Compos. Sci. Technol.*, vol. 66, no. 13, pp. 2306–2316, 2006.

[4] D. A. Burianek and S. M. Spearing, “Fatigue damage in titanium-graphite hybrid laminates,” *Compos. Sci. Technol.*, vol. 62, no. 5, pp. 607–617, 2002.

[5] D. A. Burianek and S. M. Spearing, “Modeling of facesheet crack growth in titanium–graphite hybrid laminates. Part II: Experimental results,” *Eng. Fract. Mech.*, vol. 70, no. 6, pp. 799–812, 2003.

[6] D. A. Burianek, A. E. Giannakopoulos, and S. M. Spearing, “Modeling of facesheet crack growth in titanium–graphite hybrid laminates, Part I,” *Eng. Fract. Mech.*, vol. 70, no. 6, pp. 775–798, 2003.

[7] J. Hinkley, N. Johnston, A. Hulcher, J. Marchello, and B. Messier, “Utilization of Induction Bonding for Automated Fabrication of TiGr,” National Aeronautics and Space Administration, Langley Research Center, Hampton, Virginia, NASA/TM-1999-209123, Apr. 1999.

[8] M. J. Shuart, N. J. Johnston, H. B. Dexter, J. M. Marchello, and R. W. Grenoble, “Automated fabrication technologies for high performance polymer composites,” *Compos. Fabr.*, vol. 14, no. 8, pp. 24–30, 1998.

[9] L. B. Vogelesang and A. Vlot, “Development of fibre metal laminates for advanced aerospace structures,” *J. Mater. Process. Tech*, vol. 103, no. 1, pp. 1–5, 2000.

[10] A. Vlot, L. B. Vogelesang, and T. J. De Vries, “Towards application of fibre metal laminates in large aircraft,” *Aircr. Eng. Aerosp. Technol.*, vol. 71, no. 6, pp. 558–570, 1999.

[11] R. C. Alderliesten, “Damage tolerance of bonded aircraft structures,” *Int. J. Fatigue*, vol. 31, no. 6, pp. 1024–1030, 2009.

[12] R. C. Alderliesten, J. Schijve, and S. Zwaag, “Application of the energy release rate approach for delamination growth in Glare,” *Eng. Fract. Mech.*, vol. 73, no. 6, pp. 697–709, 2006.

[13] D. A. Burianek and S. M. Spearing, “Delamination growth from face sheet seams in cross-ply titanium/graphite hybrid laminates,” *Compos. Sci. Technol.*, vol. 61, no. 2, pp. 261–269, 2001.

[14] A. Kling, “Structural Mechanics Aspects of CFRP Fuselage Structures,” in *Advances in Design and Analysis of Composite Struct ures*, German Aerospace Center, Institute of Composite Structures and Adaptive Systems, Braunschweig, 2007.

[15] H. Flower and C. Soutis, “Materials for Airframes,” *Aeronaut. J.*, vol. 107, no. 1072, pp. 331–341, Jun. 2003.

[16] C. Carey and O. Inderwildi, “Aviation Materials,” *Smith Sch. Enterp. Environ. Univ. Oxf.*, 2009.

[17] A. Asundi and A. Choi, “Fibre Metal Laminate: An Advanced Material for Future Aircraft,” *J. Mater. Process. Tech*, vol. 63, pp. 384–394, 1997.

[18] R. Alderliesten, “Fatigue Crack Propagation and Delamination Growth in Glare,” PhD Thesis, Technische Universiteit Delft, 2005.

[19] R. C. Alderliesten, “Analytical prediction model for fatigue crack propagation and delamination growth in Glare,” *Int. J. Fatigue*, vol. 29, no. 4, pp. 628–646, 2007.

[20] R. C. Alderliesten, “On the available relevant approaches for fatigue crack propagation prediction in Glare,” *Int. J. Fatigue*, vol. 29, no. 2, pp. 289–304, 2007.

[21] D. A. Burianek, D. J. Shim, and S. M. Spearing, “Durability of Hybrid Fiber Metal Composite Laminates,” in *Proceedings of the International Conference on Fracture*, Turin, Italy, 2005.
[22] P. Cortes and W. J. Cantwell, “The tensile and fatigue properties of carbon fiber-reinforced PEEK-titanium fiber-metal laminates,” *J. Reinf. Plast. Compos.*, vol. 23, no. 15, p. 1615, 2004.
[23] P. Cortes and W. J. Cantwell, “The Impact Properties of High-temperature Fiber-Metal Laminates,” *J. Compos. Mater.*, vol. 41, no. 5, p. 613, 2007.
[24] A. Fink and B. Kolesnikov, “Hybrid Titanium Composite Material Improving Composite Structure Coupling,” *Dtsch. Zent. Für Luft- Raumfahrt DLR*, no. Internal Publication, 2005.
[25] W. S. Johnson and M. W. Hammond, “Crack growth behavior of internal titanium plies of a fiber metal laminate,” *Compos. Part A*, vol. 39, no. 11, pp. 1705–1715, 2008.
[26] S. S. Kessler, J. R. Gregory, S. M. Spearing, and D. A. Burianek, “Assessment of Durability Models for Composite Materials,” *Tech. Pap. - Soc. Manuf. Eng.*, Jul. 2003.
[27] B. Kolesnikov, L. Herbeck, and A. Fink, “CFRP/titanium hybrid material for improving composite bolted joints,” *Compos. Struct.*, vol. 83, no. 4, pp. 368–380, Jun. 2008.
[28] M. Lamontia, R. Cope, M. Gruber, B. Waibel, and J. Pratte, “Stringer, Honeycomb Core, and TiGr Stiffened Skins, and Ring-Stiffened Cylinders Fabricated From Automated Thermoplastic Fiber Placement and Filament Winding,” presented at the 23rd SAMPE Europe Conference, Paris, France, 2002.
[29] E. Li, W. S. Johnson, S. E. Lowthere, and T. L. St. Clair, “An Evaluation of Two Fabrication Methods for Hybrid Titanium Composite Laminates,” in *Composites Materials Testing and Design*, vol. 13, ASTM, 1996.
[30] C. D. M. Liljedahl, M. E. Fitzpatrick, and L. Edwards, “Residual stresses in structures reinforced with adhesively bonded straps designed to retard fatigue crack growth,” *Compos. Struct.*, vol. 86, no. 4, pp. 344–355, 2008.
[31] M. Ramulu, P. B. Stickler, N. S. McDevitt, I. P. Datar, D. Kim, and M. G. Jenkins, “Influence of processing methods on the tensile and flexure properties of high temperature composites,” *Compos. Sci. Technol.*, vol. 64, no. 12, pp. 1763–1772, 2004.
[32] D. W. Rhymer, “Fatigue Damage Mechanisms of Advanced Hybrid Titanium Composite Laminates,” *Ga. Inst. Technol.*, no. MSc Dissertation, 1999.
[33] D. W. Rhymer and W. S. Johnson, “Fatigue damage mechanisms in advanced hybrid titanium composite laminates,” *Int. J. Fatigue*, vol. 24, no. 9, pp. 995–1001, 2002.
[34] T. Yamaguchi, T. Okabe, and S. Yashiro, “Fatigue simulation for titanium/CFRP hybrid laminates using cohesive elements,” *Compos. Sci. Technol.*, vol. 69, pp. 1968–1973, 2009.
[35] P. P. Camanho, A. Fink, A. Obst, and S. Pimenta, “Hybrid titanium–CFRP laminates for high-performance bolted joints,” *Compos. Part Appl. Sci. Manuf.*, vol. 40, no. 12, pp. 1826–1837, Dec. 2009.
[36] K. Schulze, J. Hausmann, and B. Wielage, “The Stability of Different Titanium-PEEK Interfaces against Water,” *Procedia Mater. Sci.*, vol. 2, pp. 92–102, 2013.
[37] A. Fink, P. P. Camanho, J. M. Andrés, E. Pfeiffer, and A. Obst, “Hybrid CFRP/titanium bolted joints: Performance assessment and application to a spacecraft payload adaptor,” *Compos. Sci. Technol.*, vol. 70, no. 2, pp. 305–317, Feb. 2010.
[38] B. Denkena, D. Boehnke, and J. H. Dege, “Helical milling of CFRP–titanium layer compounds,” *CIRP J. Manuf. Sci. Technol.*, vol. 1, no. 2, pp. 64–69, Jan. 2008.
[39] J. Hausmann, P. Naghipour, and K. Schulze, “Analytical and Numerical Residual Stress Models for Fiber Metal Laminates – Comparison and Application,” *Procedia Mater. Sci.*, vol. 2, pp. 68–73, 2013.
[40] Y. B. Hu *et al.*, “Preparation and properties of Fibre–Metal Laminates based on carbon fibre reinforced PMR polyimide,” *Compos. Part B Eng.*, vol. 69, pp. 587–591, Feb. 2015.

[41] B. Kolesnikov, L. Herbeck, and A. Fink, “CFRP/titanium hybrid material for improving composite bolted joints,” *Compos. Struct.*, vol. 83, no. 4, pp. 368–380, 2008.
[42] C. D. Rans, R. C. Alderliesten, and R. Benedictus, “Predicting the influence of temperature on fatigue crack propagation in Fibre Metal Laminates,” *Eng. Fract. Mech.*, vol. 78, no. 10, pp. 2193–2201, Jul. 2011.
[43] S. Bernhardt, M. Ramulu, and A. S. Kobayashi, “Low-Velocity Impact Response Characterization of a Hybrid Titanium Composite Laminate,” *J. Eng. Mater. Technol.*, vol. 129, no. 2, p. 220, 2007.
[44] A. Ali, L. Pan, L. Duan, Z. Zheng, and B. Sapkota, “Characterization of seawater hygrothermal conditioning effects on the properties of titanium-based fiber-metal laminates for marine applications,” *Compos. Struct.*, vol. 158, pp. 199–207, Dec. 2016.
[45] D. A. Burianek, “Mechanics of fatigue damage in titanium-graphite hybrid laminates,” PhD Thesis, Massachusetts Institute of Technology, 2001.
[46] D. Du, Y. Hu, H. Li, C. Liu, and J. Tao, “Open-hole tensile progressive damage and failure prediction of carbon fiber-reinforced PEEK–titanium laminates,” *Compos. Part B Eng.*, vol. 91, pp. 65–74, Apr. 2016.
[47] Y. Hu *et al.*, “Effects of exposure time and intensity on the shot peen forming characteristics of Ti/CFRP laminates,” *Compos. Part Appl. Sci. Manuf.*, vol. 91, pp. 96–104, Dec. 2016.
[48] X. Li, X. Zhang, H. Zhang, J. Yang, A. B. Nia, and G. B. Chai, “Mechanical behaviors of Ti/CFRP/Ti laminates with different surface treatments of titanium sheets,” *Compos. Struct.*, vol. 163, pp. 21–31, Mar. 2017.
[49] ESDU, *74039: Stress Analysis of Laminated Flat Plates*. Engineering Sciences Data Unit, Regent Street, London, 1986.
[50] P. C. T. Goncalves and J. R. S. Tavares, “A GUI for a Software that Analyses a Composite Bolted Joint,” *E-Minds Int. Jouranl Hum.-Comput. Interact.*, 2008.
[51] C. G. Davila and P. P. Camanho, “Failure Criteria for FRP Laminates in Plane Stress,” *Natl. Aeronaut. Space Adm. Langley Res. Cent.*, vol. NASA/TM-2003-212663, Nov. 2003.
[52] ASM International Handbook Committee., *ASM Handbook Volume 21 - Composites*. ASM International, 2001.
[53] J. N. Reddy, *Mechanics of Laminated Composite Plates and Shells*, 2nd ed. CRC Press, 1997.
[54] L. P. Kollar and G. S. Springer, *Mechanics of Composite Structures*. Cambridge University Press, 2003.
[55] S. W. Tsai, *Composites Design - 1986*. Think Composites, 1986.
[56] D. Gay, *Composite Materials: Design and Applications, Third Edition*. CRC Press, 2014.
[57] C. T. Sun, B. J. Quinn, and D. W. Oplinger, “Comparative Evaluation of Failure Analysis Methods for Composite Laminates.” U.S. Department of Transportation, Federal Aviation Administration, May-1996.
[58] P. P. Camanho, “Failure Criteria for Fibre-Reinforced Polymer Composites,” *Fac. Eng. Universidade Porto*, 2002.
[59] M. Hinton, P. Soden, and A. Kaddour, *Failure Criteria in Fibre-Reinforced-Polymer Composites*. Elsevier, 2004.
[60] G. B. Chai and P. Manikandan, “Low velocity impact response of fibre-metal laminates – A review,” *Compos. Struct.*, vol. 107, pp. 363–381, Jan. 2014.
[61] J. Chen, E. V. Morozov, and K. Shankar, “Progressive failure analysis of perforated aluminium/CFRP fibre metal laminates using a combined elastoplastic damage model and including delamination effects,” *Compos. Struct.*, vol. 114, pp. 64–79, Aug. 2014.
[62] E. Sitnikova, Z. W. Guan, G. K. Schleyer, and W. J. Cantwell, “Modelling of perforation failure in fibre metal laminates subjected to high impulsive blast loading,” *Int. J. Solids Struct.*, vol. 51, no. 18, pp. 3135–3146, Sep. 2014.

[63] G. Yu, L. Wu, L. Ma, and J. Xiong, “Low velocity impact of carbon fiber aluminum laminates,” *Compos. Struct.*, vol. 119, pp. 757–766, Jan. 2015.
[64] H. Nakatani, T. Kosaka, K. Osaka, and Y. Sawada, “Damage characterization of titanium/GFRP hybrid laminates subjected to low-velocity impact,” *Compos. Part Appl. Sci. Manuf.*, vol. 42, no. 7, pp. 772–781, Jul. 2011.
[65] A. Puck and A. Schurmann, “Failure Analysis of FRP Laminates By Means of Physically Based Phenomenological Models,” *Compos. Sci. Technol.*, vol. 58, pp. 1045–1067, 1998.
[66] Engineering Sciences Data Unit, “ESDU 83014: Failure criteria for an individual layer of a fibre reinforced composite laminate under in-plane loading.” 1983.
[67] S. W. Tsai, “Strength Characteristics of Composite Materials,” *NASA CR-224*, 1965.
[68] S. W. Tsai and E. M. Wu, “A general theory of strength for anisotropic materials,” *J. Compos. Mater.*, vol. 5, pp. 58–80, 1971.
[69] A. H. Puppo and H. A. Evensen, “Strength of Anisotropic Materials under Combined Stresses,” *AIAA J.*, vol. 10, no. 4, pp. 468–474, 1972.
[70] Z. Hashin, “Failure criteria for unidirectional fiber composites,” *J. Appl. Mech.*, vol. 47, no. 2, pp. 329–334, 1980.
[71] E. J. Barbero, *Finite Element Analysis of Composite Materials using Abaqus*. CRC Press, 2013.
[72] R. C. Burk, “Standard Failure Criteria Needed for Advanced Composites,” *Astronaut. Aeronaut.*, pp. 58–62, Jun. 1983.
[73] M. J. Hinton and P. D. Soden, “Predicting failure in composite laminates: the background to the exercise,” *Compos. Sci. Technol.*, vol. 58, no. 7, pp. 1001–1010, 1998.
[74] M. J. Hinton, A. S. Kaddour, and P. D. Soden, “A comparison of the predictive capabilities of current failure theories for composite laminates, judged against experimental evidence,” *Compos. Sci. Technol.*, vol. 62, no. 12, pp. 1725–1797, 2002.
[75] P. D. Soden, A. S. Kaddour, and M. J. Hinton, “Recommendations for designers and researchers resulting from the world-wide failure exercise,” *Compos. Sci. Technol.*, vol. 64, no. 3, pp. 589–604, 2004.
[76] G. Corderley and A. Cardoso, “Case Studies in Composite Material Structural Design, Manufacture and Testing,” in *ICAS Proceedings 1992*, Beijing, People’s Republic of China, 1992, vol. 2.
[77] “<http://www.ecss.nl/>.” Oct-2014.
[78] European Cooperation for Space Standardisation, “ECSS-E-HB-32-20 Part 2A, Space engineering - Structural materials handbook - Part 2: Design calculation methods and general design aspects.” ECSS Secretariat, ESA-ESTEC, Requirements & Standards Division, Noordwijk, The Netherlands, 20-Mar-2011.
[79] R. G. Cuntze, “Efficient 3D and 2D failure conditions for UD laminae and their application within the verification of the laminate design,” *Compos. Sci. Technol.*, vol. 66, no. 7–8, pp. 1081–1096, Jun. 2006.
[80] R. G. Cuntze and A. Freund, “The predictive capability of failure mode concept-based strength criteria for multidirectional laminates,” *Compos. Sci. Technol.*, vol. 64, no. 3–4, pp. 343–377, Mar. 2004.
[81] R. G. Cuntze, “The predictive capability of failure mode concept-based strength criteria for multi-directional laminates—part B,” *Compos. Sci. Technol.*, vol. 64, no. 3–4, pp. 487–516, Mar. 2004.
[82] L. J. Hart-Smith, “Predictions of a Generalized Maximum-Shearstress Failure Criterion for Certain Fibrous Composite Laminates,” *Compos. Sci. Technol.*, vol. 58, pp. 1179–1208, 1998.
[83] W. T. Becker and R. J. Shipley, *ASM Handbook Volume 11 - Failure Analysis and Prevention*, Fourth Printing. ASM International, 2007.
[84] N. Dowling, *Mechanical Behavior of Materials*, Second. Prentice Hall, 1999.
[85] T. Wierzbicki, Y. Bao, Y.-W. Lee, and Y. Bai, “Calibration and evaluation of seven fracture models,” *Int. J. Mech. Sci.*, vol. 47, no. 4–5, pp. 719–743, Apr. 2005.

[86] T. B. Stoughton and J. W. Yoon, “A new approach for failure criterion for sheet metals,” *Int. J. Plast.*, vol. 27, no. 3, pp. 440–459, Mar. 2011.
[87] Y. Tachibana and T. Iyoku, “Structural design of high temperature metallic components,” *Nucl. Eng. Des.*, vol. 233, no. 1–3, pp. 261–272, Oct. 2004.
[88] X. Wang, “A method for calculating damage evolution in adiabatic shear band of titanium alloy,” *Trans. Nonferrous Met. Soc. China*, vol. 19, no. 5, pp. 1280–1285, Oct. 2009.
[89] K. Osakada, “History of plasticity and metal forming analysis,” *J. Mater. Process. Technol.*, vol. 210, no. 11, pp. 1436–1454, Aug. 2010.
[90] I. Sen, S. Tamirisakandala, D. Miracle, and U. Ramamurty, “Microstructural effects on the mechanical behavior of B-modified Ti–6Al–4V alloys,” *Acta Mater.*, vol. 55, no. 15, pp. 4983–4993, Sep. 2007.
[91] I. Sen, K. Gopinath, R. Datta, and U. Ramamurty, “Fatigue in Ti–6Al–4V–B alloys,” *Acta Mater.*, vol. 58, no. 20, pp. 6799–6809, Dec. 2010.
[92] M. Zhang, J. Zhang, and D. L. McDowell, “Microstructure-based crystal plasticity modeling of cyclic deformation of Ti–6Al–4V,” *Int. J. Plast.*, vol. 23, no. 8, pp. 1328–1348, Aug. 2007.
[93] ESDU, *84018: Failure Analysis of Fibre Reinforced Composite Laminates*. Engineering Sciences Data Unit, Regent Street, London, 1984.
[94] ASTM International Handbook Committee., “E 8M – 04: Standard Test Methods for Tension Testing of Metallic Materials [Metric].” 100 Barr Harbor Drive, PO Box C700, West Conshohocken, PA 19428-2959, United States, 2004.
[95] ASTM International, “D 3039/D 3039 M: Standard Test Method for Tensile Properties of Polymer Matrix Composite Materials1.” 100 Barr Harbor Drive, PO Box C700, West Conshohocken, PA 19428-2959, United States, 2000.
[96] E. C. Botelho, R. S. Almeida, L. C. Pardini, and M. C. Rezende, “Elastic properties of hygrothermally conditioned glare laminate,” *Int. J. Eng. Sci.*, vol. 45, pp. 163–172, 2007.
[97] J. Carrillo and W. Cantwell, “Scaling effects in the tensile behavior of fiber-metal laminates,” *Compos. Sci. Technol.*, vol. 67, no. 7–8, pp. 1684–1693, Jun. 2007.
[98] P. Iaccarino, A. Langella, and G. Caprino, “A simplified model to predict the tensile and shear stress–strain behaviour of fibreglass/aluminium laminates,” *Compos. Sci. Technol.*, vol. 67, no. 9, pp. 1784–1793, Jul. 2007.
[99] M. Kawai and Y. Arai, “Off-axis notched strength of fiber–metal laminates and a formula for predicting anisotropic size effect,” *Compos. Part Appl. Sci. Manuf.*, vol. 40, no. 12, pp. 1900–1910, Dec. 2009.
[100] S. M. R. Khalili, R. K. Mittal, and S. G. Kalibar, “A study of the mechanical properties of steel/aluminium/GRP laminates,” *Mater. Sci. Eng. A*, vol. 412, no. 1–2, pp. 137–140, 2005.
[101] B.-E. Lee, E.-T. Park, J. Kim, B.-S. Kang, and W.-J. Song, “Analytical evaluation on uniaxial tensile deformation behavior of fiber metal laminate based on SRPP and its experimental confirmation,” *Compos. Part B Eng.*, vol. 67, pp. 154–159, Dec. 2014.
[102] S. E. Moussavi-Torshizi, S. Dariushi, M. Sadighi, and P. Safarpour, “A study on tensile properties of a novel fiber/metal laminates,” *Mater. Sci. Eng. A*, vol. 527, no. 18–19, pp. 4920–4925, Jul. 2010.
[103] M. Vasumathi and V. Murali, “Effect of Alternate Metals for use in Natural Fibre Reinforced Fibre Metal Laminates under Bending, Impact and Axial Loadings,” *Procedia Eng.*, vol. 64, pp. 562–570, 2013.
[104] J. Xue, W.-X. Wang, Y. Takao, and T. Matsubara, “Reduction of thermal residual stress in carbon fiber aluminum laminates using a thermal expansion clamp,” *Compos. Part Appl. Sci. Manuf.*, vol. 42, no. 8, pp. 986–992, Aug. 2011.
[105] P. Murthy and C. Chamis, “Free-edge delamination: laminate width and loading condition effects,” *NASATM-100238*, 1987.

[106] M. M. D. Coetzer, “AMTS Material Test Report - Preliminary B-Basis Design Allowables for Sigratex Kdu 1092 / Axson Epolam 2022 Unidirectional Carbon Fibre Epoxy Composite,” CSIR, AMTS-MTR-0002-A-2010, Jun. 2010.
[107] ASTM International, “D 3171 – 99: Standard Test Methods for Constituent Content of Composite Materials.” 100 Barr Harbor Drive, PO Box C700, West Conshohocken, PA 19428-2959, United States, 2004.
[108] ASTM International, “D 792-08, Standard Test Methods for Density and Specific Gravity (Relative Density) of Plastics by Displacement.” 100 Barr Harbor Drive, PO Box C700, West Conshohocken, PA 19428-2959, United States, 2008.
[109] K. Vanden, S. Ellison, and B. Case, “AFRL-MN-EG-TP-2006-7404: Hypersonic and Unsteady Flow Science Issues for Explosively Formed Penetrator Warheads,” presented at the AFOSR Hypersonics and Boundary Layers Program Annual Review, Atlanta, Georgia, USA, 2006.
[110] David Axe, “Next Step for MRAP,” *Defense Technology International*, Washington, Nov-2007.
[111] B. Cour-Palais, “A career in applied physics: Apollo through space station,” *Int. J. Impact Eng.*, vol. 23, no. 1, pp. 137–168, 1999.
[112] E. L. Christiansen and J. H. Kerr, “Ballistic Limit Equations for Spacecraft Shielding,” *Int. J. Impact Eng.*, vol. 26, pp. 93–104, 2001.
[113] S. Ryan and E. L. Christiansen, “A ballistic limit analysis programme for shielding against micrometeoroids and orbital debris,” *Acta Astronaut.*, vol. 69, no. 5–6, pp. 245–257, Sep. 2011.
[114] S. Ryan and E. L. Christiansen, “Micrometeoroid and Orbital Debris (MMOD) Shield Ballistic Limit Analysis Program, NASA TM-2009-214789.” 2010.
[115] K. B. Hayashida and J. H. Robinson, “Single wall penetration equations,” 1991.
[116] F. K. Schaefer, M. Herrwerth, S. Hiermaier, and E. E. Schneider, “Shape Effects in Hypervelocity Impact on Semi-Infinite Metallic Targets,” *Int. J. Impact Eng.*, vol. 26, pp. 699–711, 2001.
[117] C. L. Frost and P. I. Rodrguez, “AXAF Hypervelocity Impact Test Results,” presented at the Proceedings of the Second European Conference on Space Debris, ESOC, Darmstadt, Germany, 1997.
[118] W. P. Schonberg, “Protecting Earth-orbiting spacecraft against micro-meteoroid/orbital debris impact damage using composite structural systems and materials: An overview,” *Adv. Space Res.*, vol. 45, no. 6, pp. 709–720, Mar. 2010.
[119] S. Ryan, F. Schaefer, R. Destefanis, and M. Lambert, “A ballistic limit equation for hypervelocity impacts on composite honeycomb sandwich panel satellite structures,” *Adv. Space Res.*, vol. 41, no. 7, pp. 1152–1166, Jan. 2008.
[120] E. L. Christiansen, *Meteoroid/debris shielding*. National Aeronautics and Space Administration, Lyndon B. Johnson Space Center, 2003.
[121] T. Børvik, O. S. Hopperstad, M. Langseth, and K. A. Malo, “Effect of target thickness in blunt projectile penetration of Weldox 460 E steel plates,” *Int. J. Impact Eng.*, vol. 28, no. 4, pp. 413–464, 2003.
[122] Department of Defense Handbook, *MIL-STD-662F, Department Of Defense Test Method Standard - V50 Ballistic Test for Armor*. 1997.
[123] G. Ben-Dor, A. Dubinsky, and T. Elperin, *High-Speed Penetration Dynamics: Engineering Models and Methods*. World Scientific, 2013.
[124] J. P. Lambert and G. H. Jonas, “Towards Standardization in Terminal Ballistics Testing: Velocity Representation,” Ballistic Research Laboratories, Aberdeen Proving Ground, Maryland, BRL Report No. 1852, Jan. 1976.
[125] G. Ben-Dor, A. Dubinsky, and T. Elperin, “On the Lambert–Jonas approximation for ballistic impact,” *Mech. Res. Commun.*, no. 29, pp. 137–139, 2002.
[126] S. Abrate, “Ballistic impact on composites,” in *16th Int. Conf. on Composite Materials*, 2007.
[127] ASTM International, “D 1002-01, Standard Test Method for Apparent Shear Strength of Single-Lap-Joint Adhesively Bonded Metal Specimens by Tension Loading (Metal-

to-Metal).” 100 Barr Harbor Drive, PO Box C700, West Conshohocken, PA 19428-2959, United States, 2001.
[128] S. Liao and J. Duffy, “Adiabatic shear bands in a Ti-6Al-4V titanium alloy,” *J. Mech. Phys. Solids*, vol. 46, no. 11, pp. 2201–2231, 1998.
[129] F. Martinez, L. E. Murr, A. Ramirez, M. I. Lopez, and S. M. Gaytan, “Dynamic deformation and adiabatic shear microstructures associated with ballistic plug formation and fracture in Ti–6Al–4V targets,” *Mater. Sci. Eng. A*, 2007.
[130] C. Zheng *et al.*, “Capturing of the propagating processes of adiabatic shear band in Ti–6Al–4V alloys under dynamic compression,” *Mater. Sci. Eng. A*, no. 658, p. 2016.
[131] D.-G. Lee, Y. G. Kim, D.-H. Nam, S.-M. Hur, and S. Lee, “Dynamic deformation behavior and ballistic performance of Ti–6Al–4V alloy containing fine α2 (Ti3Al) precipitates,” *Mater. Sci. Eng. A*, vol. 391, no. 1, pp. 221–234, 2005.
[132] S. Dey, T. Børvik, O. S. Hopperstad, J. R. Leinum, and M. Langseth, “The effect of target strength on the perforation of steel plates using three different projectile nose shapes,” *Int. J. Impact Eng.*, vol. 30, no. 8–9, pp. 1005–1038, Sep. 2004.
[133] J. Peirs *et al.*, “Microstructure of adiabatic shear bands in Ti6Al4V,” *Mater. Charact.*, vol. 75, pp. 79–92, Jan. 2013.
[134] S.-T. Chiou, H.-L. Tsai, and W.-S. Lee, “Effects of strain rate and temperature on the deformation and fracture behaviour of titanium alloy,” *Mater. Trans.*, vol. 48, no. 9, pp. 2525–2533, 2007.
[135] A. Molinari, C. Musquar, and G. Sutter, “Adiabatic shear banding in high speed machining of Ti–6Al–4V: experiments and modeling,” *Int. J. Plast.*, vol. 18, no. 4, pp. 443–459, 2002.
[136] X. Liu, C. Tan, J. Zhang, F. Wang, and H. Cai, “Correlation of adiabatic shearing behavior with fracture in Ti-6Al-4V alloys with different microstructures,” *Int. J. Impact Eng.*, vol. 36, no. 9, pp. 1143–1149, Sep. 2009.
[137] Q. Xue, M. A. Meyers, and V. F. Nesterenko, “Self-organization of shear bands in titanium and Ti–6Al–4V alloy,” *Acta Mater.*, vol. 50, no. 3, pp. 575–596, 2002.